



FRIEDRICH-SCHILLER-UNIVERSITÄT  
JENA

PHYSIKALISCH-ASTRONOMISCHE FAKULTÄT

ASTROPHYSIKALISCHES INSTITUT UND  
UNIVERSITÄTS-STERNWARTE



# The Edgeworth-Kuiper Belt as a Debris Disk

—DISSERTATION—

zur Erlangung des Akademischen Grades  
Doctor Rerum Naturalium (Dr. rer. nat.)

vorgelegt dem Rat der Physikalisch-Astronomischen Fakultät  
der Friedrich-Schiller-Universität Jena

von Dipl.-Phys. CHRISTIAN VITENSE  
geboren am 26. Juni 1984 in Templin

1. Gutachter: Prof. Dr. Alexander V. Krivov  
Friedrich-Schiller-Universität Jena
2. Gutachter: Prof. Dr. Sebastian Wolf  
Christian-Albrechts-Universität zu Kiel
3. Gutachter: Prof. Dr. Marc Kuchner  
NASA Goddard Space Flight Center

Tag der Disputation: 01. 11. 2012

# Contents

<b>Kurzfassung</b>	<b>v</b>
<b>Abstract</b>	<b>vi</b>
<b>1. Introduction</b>	<b>1</b>
1.1. The (Outer) Solar System . . . . .	1
1.2. Planet Formation and the Nice Model . . . . .	2
1.3. Debris Disks and the EKB in Context . . . . .	5
1.4. Aims . . . . .	7
<b>2. Theoretical Background</b>	<b>9</b>
2.1. Keplerian Orbits . . . . .	9
2.2. Effects and Forces on Dust Grains . . . . .	11
2.2.1. Gravity . . . . .	11
2.2.2. Interaction of Grains with Radiation . . . . .	12
2.2.3. Radiation Pressure and Poynting-Robertson Drag . . . . .	13
2.2.4. Stellar Wind Drag . . . . .	16
2.3. Collisions . . . . .	16
2.4. Kinetic Theory . . . . .	20
2.4.1. Number Density and Phase Space Variables . . . . .	20
2.4.2. The Master Equation . . . . .	21
2.4.3. Orbital Elements of Fragments . . . . .	22
2.4.4. Evolution of Debris Disks . . . . .	24
2.5. Thermal Emission of Debris Disks . . . . .	25
<b>3. Planetesimals in the Kuiper belt</b>	<b>27</b>
3.1. Observations and Their Biases . . . . .	27
3.2. Classification of TNOs . . . . .	30
3.3. Debiasing Procedure . . . . .	31
3.4. Orbital Element Distributions of the EKB Objects . . . . .	37
3.5. Albedos and Sizes of the Kuiper Belt Objects . . . . .	39
3.6. Mass of the Kuiper Belt . . . . .	41
3.7. Size Distribution of the Kuiper Belt Objects . . . . .	44

<b>4. Model of the EKB Debris Disk in Collisional Equilibrium</b>	<b>47</b>
4.1. Setup of the Collisional Simulations . . . . .	48
4.2. Results of the Collisional Simulations . . . . .	49
4.3. Thermal Emission . . . . .	57
4.3.1. Spectral Energy Distribution . . . . .	57
4.3.2. Surface Brightness Synthetic Images . . . . .	61
4.3.3. Detectability of “Kuiper Belts” . . . . .	62
<b>5. An Improved Model of the Edgeworth-Kuiper Debris Disk</b>	<b>64</b>
5.1. Setup of the Collisional Simulations . . . . .	64
5.2. Results of the Collisional Simulations . . . . .	66
5.3. Influence of Planets . . . . .	72
5.3.1. Resonant Trapping . . . . .	72
5.3.2. Gravitational Scattering . . . . .	76
5.4. Influence of Sublimation . . . . .	77
5.5. Comparison with Spacecraft Measurements . . . . .	80
5.6. Consistency Check with the Nice Model . . . . .	81
5.7. Thermal Emission Constraints . . . . .	83
5.7.1. Spectral Energy Distribution . . . . .	83
5.7.2. Surface Brightness Synthetic Images . . . . .	85
5.7.3. Detectability of the Kuiper Belt . . . . .	86
<b>6. Summary and Outlook</b>	<b>88</b>
6.1. Kuiper Belt Objects . . . . .	88
6.2. Model of the Kuiper Belt in Collisional Equilibrium . . . . .	89
6.3. An Improved Model of the Edgeworth-Kuiper Debris Disk . . . . .	92
6.4. Future Work . . . . .	95
<b>Bibliography</b>	<b>98</b>
<b>Danksagung</b>	<b>115</b>
<b>Ehrenwörtliche Erklärung</b>	<b>116</b>

# Kurzfassung

Allgegenwärtige Begleiter von Hauptreihensternen sind die sogenannten Trümmerscheiben. Sie sind Überreste der Planetenentstehung und bestehen aus Planetesimalen, welche in gegenseitigen Kollisionen kleinen Staub produzieren. Und es ist dieser Staub, welcher entweder im Streulicht des Sterns oder durch thermische Emission beobachtet werden kann. Durch Modellierung können dann Rückschlüsse vom Staub auf den staubproduzierenden Planetesimalgürtel gezogen werden und es besteht durchaus sogar die Möglichkeit, Zwangsbedingungen an die Existenz von Planeten in solchen Systemen zu knüpfen. Der dominierende Teil der Trümmerscheibe des Sonnensystems ist der Kuipergürtel (EKB), in dem die Situation umgekehrt ist. Hier kennen wir die Mutterkörper des Staubes, die transneptunischen Objekte (TNOs), und die Planeten. Jedoch ist das Wissen über den Staub begrenzt, da eine Detektion auf Grund der starken Emission des Zodiakallichtes unmöglich ist. Unter Anwendung derselben Kollisionsmodelle für extrasolare Trümmerscheiben auf das Sonnensystem, jedoch von Planetesimalen zu Staub, ist es möglich, die Verbindung zwischen Planetesimalen und Staub besser zu verstehen. Dieses Modell kann dann als Referenzmodell für alle Trümmerscheiben verwendet werden.

Zu diesem Zwecke wird die Datenbank der TNOs neu analysiert und ein Algorithmus zur Beseitigung des Entfernungs- und Inklinationsfehlers entwickelt. Aus der bekannten Population der TNOs wird so die „wahre“. Dessen Masse beträgt  $M_{\text{EKB}} = 0,12M_{\oplus}$  und ist damit zirka 15 mal so schwer wie die Masse der bisher bekannten Objekte.

Mit diesem Ergebnis wird der Staub mittels unseres Kollisionscodes erzeugt. Der Einfluss von gravitativer Streuung und des Resonanzeinfangs von Planeten wurde in die resultierenden Staubverteilungen genauso eingearbeitet, wie der Vorgang der Sublimation.

Den größten Einfluss auf die Menge und die Verteilung des Staubes haben die subkilometergroßen Objekte. Diese sind jedoch nicht beobachtbar und auch Kollisionsmodellierung ist nicht möglich, da sich Objekte, die größer als 10 . . . 60 m sind, nicht im Kollisionsgleichgewicht befinden. Um weitere Einschränkungen zu finden, werden Messungen der New Horizons Sonde verwendet. Wir zeigen, dass ein Knick in der Größenverteilung bei  $s \lesssim 70$  km dringend notwendig ist, um konsistent mit den Messungen zu bleiben. Sollte dieser Knick ebenso bei anderen Trümmerscheiben vorhanden sein, wäre die Gesamtmasse der Planetesimale in vorangegangenen Untersuchungen unterschätzt worden. Trotz der Einschränkungen existieren weiterhin verschiedene Modelle, den nahezu konstanten Staubfluss in der Nähe der Gasriesen zu rekonstruieren, welche auch die Zwangsbedingungen des COBE-Teleskops nicht verletzen. Die resultierende Kuipergürtelstaubscheibe ist entweder transportdominiert oder an der Grenze zwischen transport- und kollisionsdominiert. Die parallele optische Dicke beträgt  $\tau_{\parallel}(r > 10 \text{ AU}) \sim 10^{-6}$  und die partielle Leuchtkraft  $f_d \sim 10^{-7}$ . Es zeigt sich, dass Planeten und Sublimation nur einen kleinen Einfluss auf den Staub- und thermischen Fluss haben. Die spektrale Energieverteilung des Kuipergürtels, gesehen von einer Entfernung von 10 pc hätte ihr Maximum bei 40 . . . 50  $\mu\text{m}$  mit  $F \approx 0,5 \text{ mJy}$ , was weniger als 1% des Photosphärenflusses bei diesen Wellenlängen entspricht. Daraus schließen wir, dass EKBs mit ähnlichen Eigenschaften selbst mit dem aktuellen Herschel/PACS Instrument nicht entdeckbar sind.

# Abstract

Debris disks are commonly found around main-sequence stars. As remnants of planet formation, they consist of left-over planetesimals that produce small debris in mutual collisions. It is these dust-sized fragments that can be observed in scattered stellar light or through thermal radiation. Modelers then can draw conclusions from the dust on the dust-producing planetesimal ring and it may even be possible to infer the existence of planets in such systems. The dominant part of the Solar System’s debris disk is the Edgeworth-Kuiper belt and the situation is reverse. Here, we know the parent bodies of dust, the transneptunian objects, and the planets, but there is only sparse knowledge of the dust, because it eludes detection due to the strong foreground emission of the zodiacal cloud. Modelling the debris disk of the Solar System with the same collisional models as used for other debris disks, but from planetesimals to dust, will help to understand the link between planetesimals and dust. This model can serve as a natural reference model for all debris disks.

Therefore, we re-analyze the current database of known TNOs and employ a new algorithm to eliminate the inclination and the distance selection effects in the known TNO populations to derive expected parameters of the “true” EKB. Its estimated mass is  $M_{\text{EKB}} = 0.12M_{\oplus}$ , which is larger by a factor of  $\sim 15$  than the mass of the TNOs detected so far.

Treating the debiased population of TNOs as parent bodies, we generate the dust with our collisional code. The resulting dust distributions are modified to take into account the influence of gravitational scattering and resonance trapping by planets on migrating dust grains as well as the effect of sublimation.

The amount and distribution of dust are largely determined by sub-kilometer-sized bodies. These are directly unobservable and their properties cannot be determined through collisional modeling because objects larger than  $10 \dots 60$  m in the present-day EKB are not in a collisional equilibrium. To place additional constraints, we use in-situ measurements of the New Horizons spacecraft within 20 AU. We show that, to sustain a dust disk consistent with these measurements, the TNO population *has* to have a break in the size distribution at  $s \lesssim 70$  km. If such a break is present in other debris disks as well, than the total mass of planetesimals in these disks has been underestimated in previous studies. However, even this still leaves us with several models that all correctly reproduce the nearly constant dust impact rates in the region of giant planet orbits and do not violate the constraints from the non-detection of the EKB dust thermal emission by the COBE spacecraft. The modeled EKB dust disks, which conform to the observational constraints, can either be transport-dominated or intermediate between the transport-dominated and collision-dominated regime. The in-plane optical depth of such disks is  $\tau_{\parallel}(r > 10 \text{ AU}) \sim 10^{-6}$  and their fractional luminosity is  $f_d \sim 10^{-7}$ . Planets and sublimation are found to have little effect on dust impact fluxes and dust thermal emission. The spectral energy distribution of an EKB analog as seen from 10 pc distance peaks at wavelengths of  $40 \dots 50 \mu\text{m}$  at  $F \approx 0.5 \text{ mJy}$ , which is less than 1% of the photospheric flux at those wavelengths. Therefore, EKB analogs cannot be detected with present-day instruments such as Herschel/PACS.

# 1. Introduction

“Astronomy taught us our insignificance in Nature.”

---

Ralph Waldo Emerson (1803-1882)

## 1.1. The (Outer) Solar System

When one asks people what they know about the Solar System, most of them surely know about the Sun and a few planets. Fewer will remember that some of these planets have moons and they saw comets and meteoroids in form of shooting stars. And very few people have heard about the existence of an asteroid and Kuiper belt<sup>1</sup>. However, that is only the big picture, the details are enormous.

Approximately 580 000 known objects are orbiting the Sun in the main belt<sup>2</sup>. Another  $\approx 700$  Atens,  $\approx 4300$  Apollos,  $\approx 3600$  Armors,  $\approx 5200$  Trojans,  $\approx 170$  Centaurs,  $\approx 1300$  Edgeworth-Kuiper belt objects (EKBOs)<sup>3</sup>, and  $\approx 3200$  comets<sup>4</sup> are known in the Solar System. For all of these objects, e.g., size, albedo, color, surface features, and chemical composition can be studied individually. The effort to acquire this knowledge reaches from Earth-based surveys over space telescopes and space missions to spacecraft that fly to an object, land on it, take samples, and bring them back to Earth like the Stardust or the Hayabusa mission (see, e.g., Brownlee et al., 2006; Nakamura et al., 2011).

Why do we do this? Knowing the composition of different classified objects can help to understand the history of each class and therefore the formation history of the Solar System as a whole. But at first, we have to build the basic components of a planetary system: the planet(esimal)s.

---

<sup>1</sup>The Kuiper belt is also known as Edgeworth-Kuiper belt (EKB). Both names and the abbreviation are used synonymously in this thesis.

<sup>2</sup>Named, e.g., Asterix, Obelix, Idefix, Hansa, Mecklenburg, Jena, Thuringia, and Gerhardmuller. Find all of them at [http://ssd.jpl.nasa.gov/?sb\\_elem](http://ssd.jpl.nasa.gov/?sb_elem) (last accessed on 29 June 2012).

<sup>3</sup>Find Apollos, Armors, Trojans, Centaurs and EKBOs at <http://www.minorplanetcenter.net/iau/lists/MPLists.html>, last accessed on 29 June 2012. Note that the scattered disk objects are listed with the Centaurs, but they are counted as EKBOs here.

<sup>4</sup>Some of these comets are Sun-grazers and do not exist anymore ([http://ssd.jpl.nasa.gov/?sb\\_elem](http://ssd.jpl.nasa.gov/?sb_elem), last accessed on 29 June 2012).

## 1.2. Planet Formation and the Nice Model

The formation mechanism of planetesimals and planets is still a matter of debate in modern astronomy. Here I try to summarize the state-of-the-art theories. When a protostellar cloud collapses because of its self-gravity and the protostar forms, the sphere-like envelope composed of dust and gas (the ratio between dust and gas is usually assumed to be 100:1, Hildebrand 1983) eventually will collapse into a disk. At a few AU it takes only  $10^3$ – $10^4$  yr for tiny dust grains to settle to the disk mid-plane. There, the dust grains collide with each other with low relative velocities and electrostatic and intermolecular forces lead to sticking and therefore to the formation of larger particles with millimeter- and centimeter-sized grains (e.g., Safronov, 1969; Dominik & Tielens, 1997; Wurm & Blum, 1998; Blum et al., 2000)<sup>5</sup>.

Increased relative velocities between larger grains then hamper further growth because the efficiency of sticking decreases (Blum & Wurm, 2008), but the net result is still growth. A critical size is reached for meter-sized boulders<sup>6</sup>. At 1 m migration toward the star due to gas drag is most efficient and impact onto the star occurs within 100 . . . 1000 yr from 1 AU at a density of 1 Minimum Mass Solar Nebula (MMSN Weidenschilling, 1977, 1980; Hayashi, 1981). Since the gas drag is size-dependent the relative velocity of different sized grains can increase to several meters per second and agglomeration becomes inefficient. Due to gas turbulence in the protoplanetary disk even equal-sized particles have non-zero relative velocities. The highest relative velocities for equal-sized objects are between meter-sized objects (e.g., Cuzzi & Weidenschilling, 2006; Dominik et al., 2007, and references therein) at which destruction is more likely to appear than sticking (Wurm et al., 2005). Therefore, the so-called *meter-barrier* is twofold.

Although the formation of supra-meter objects is still an unsolved problem, nature somehow overcomes the meter-barrier, obviously. Once this happened, collisional coagulation among planetesimals will lead to further growth, resulting in increased gravity of the objects which in turn results in an increased collisional cross section (Safronov, 1969; Greenzweig & Lissauer, 1992). At first, a protoplanetary disk is dynamically cold, i.e. the eccentricities and inclinations of objects are very low. Thus, the relative velocities between objects are small and for planetesimals even smaller than their escape velocities which results in a rapid accretion of material. The so-called *runaway growth* (Green-

---

<sup>5</sup>During this process not all encounters lead to sticking. Some collisions have to be fragmenting, otherwise tiny dust grains would be underabundant or even nonexistent, which is in contradiction to observations around T Tauri stars (Dullemond & Dominik, 2005).

<sup>6</sup>Note that this critical size is dependent on the distance to the star and the density.



berg et al., 1978; Wetherill & Stewart, 1989) begins. This phase is most effective for the largest bodies, they grow the fastest. With increasing size and therefore gravity the disk is dynamically heated by the largest bodies. This stirring leads to increased eccentricities and relative velocities become higher. A changeover from the runaway growth to the *oligarchic growth* (Ida & Makino, 1993) occurs when eccentricities become high enough that relative velocities between two objects are in the same order of magnitude as the escape velocities. The rapid growth for the largest objects is slowed down, but not stopped. During this phase the influence of (outer) planetary perturbers have to be considered (Th ebault & Brahic, 1998; Th ebault et al., 2002; Raymond et al., 2006). After both phases planetary embryos have formed.

However, the formation of planets is not finished at this point. To build gas giants two conditions have to be fulfilled. First, to start rapid gas accretion a critical core mass of  $10M_{\oplus}$  (Mizuno, 1980) is needed. Second, gas in the protoplanetary disk vanishes within 3 . . . 6 Myr (Haisch et al., 2001; Hern andez et al., 2009), i.e. gas giants have to have formed by this time. Here the so-called *timescale*-problem arises for the Solar System. The density of the MMSN at the location of Neptune and Uranus is too low to form a  $10M_{\oplus}$  core in 10 Myr (e.g., Safronov, 1969; Lissauer, 1987; Kenyon & Bromley, 2008)<sup>7</sup>. The model of the MMSN can be applied to extrasolar multi-planetary systems. Kuchner (2004) constructed Minimum Mass *Extrasolar* Nebulas analog to the MMSN and showed they are consistent with each other.

By assuming an initial mass of 10 MMSN and planetesimals of 100 km in radius Kobayashi et al. (2011) showed that the critical core mass can be reached at least in the Jupiter-Saturn region by taking into account tenuous atmospheres of Mars-sized planetary embryos. As an alternative, Boss (1997) suggested that gas giants can form directly through gravitational instability, but with a moderate solid core.

At this point, there are two unsolved problems. How to overcome the meter-barrier and how to build Neptune and Uranus at their current location? For the first problem an alternative scenario which bypasses slow growth by accretion and therefore the meter-barrier is proposed: the gravitational instability. Even before the knowledge of the existence of this critical barrier Toomre (1964); Safronov (1969); Goldreich & Ward (1973) showed that local overdensities of dust can cause a (gravitational) collapse and lead to rapid formation of kilometer-sized planetesimals within 10 AU. To create these overdensities turbulence is suggested (Rice et al., 2004; Johansen et al., 2007; Cuzzi et al., 2008). In this turbulence (e.g., caused by magneto-rotational instability, Balbus & Hawley 1992)

---

<sup>7</sup>This is also true for the largest transneptunian objects, they could not have formed there.

the gas drag pushes solid particles to the maximum of the gas density. Although the gas density changes fast in turbulences, the maxima live long enough to concentrate a huge amount of submeter-sized objects, which eventually leads to growth of objects with even a few times the mass of Ceres ( $\sim 1000$  km, Johansen et al. 2006; Johansen et al. 2007). Furthermore, Cuzzi et al. (2008) showed that in some cases it is possible that chondrule concentrations can become dense enough to form clumps. Although the internal gas pressure counteracts further compression, the clumps can gradually concentrate, leading to formation of planetesimals of  $10 \dots 1000$  km in radius. Morbidelli et al. (2009) pointed out that if these scenarios are true, then kilometer-sized planetesimals are strongly underabundant and “asteroids were born big”. In their simulations they could reconstruct the size frequency distribution of the asteroid belt only by assuming planetesimals with sizes of initially  $\sim 100$  km to several  $100$  km. In addition, there is some observational evidence for a break in the size distribution in the Kuiper belt at several tens of kilometers which is the same argument for born big planetesimals (Bernstein et al., 2004; Fraser, 2009).

Still, the second problem of building Neptune and Uranus at their current location is not yet solved completely. The Nice<sup>8</sup> model shows promising results in solving it<sup>9</sup> (see, e.g., Morbidelli, 2010, for a recent review), being able to explain many of the observed properties of the Solar System. In the Nice model, the four giant planets (and the largest EKBOs) have formed closer in where the material density was higher. Gomes et al. (2005) suggested a compact initial configuration of the giant planets and the Kuiper belt. Jupiter, Saturn, Neptune, and Uranus are located at 5.45 AU, 8.18 AU, 11.5 AU, and 14.2 AU, respectively<sup>10</sup> and a  $35M_{\oplus}$  mass EKB is placed between 15.5 AU and 34 AU. Due to interactions with planetesimals, Jupiter and Saturn migrate outwards, finally crossing their mutual 2:1 orbital resonance which causes a short-lasting period of dynamical instability, mirroring the geologically recorded event of the so-called *Late Heavy Bombardment* (LHB) and placing the giant planets and the EKB to their current positions. This event not only re-arranged the planets and the EKB but also reduced the mass of the latter to  $\approx 0.1M_{\oplus}$  (see Chapter 3). Furthermore, Morbidelli et al. (2005) showed that the Nice model is capable of explaining the population of the Jovian Trojans to a good extent. Another success is the reproduction of the amount and size distribution of the irregular satellites of the giant planets (Nesvorný et al., 2007; Bottke et al., 2010). Finally, Levison

---

<sup>8</sup>Named after the city in France in the Provence-Alpes-Côte d’Azur ( $43^{\circ}42' N$ ,  $7^{\circ}16' E$ ), where the institute that developed the model is based.

<sup>9</sup>See Goldreich et al. (2004) for an alternative solution not involving the Nice model.

<sup>10</sup>Note that this is only one example of possible initial conditions that are able to reconstruct the current structure in the Solar System. In this model Neptune and Uranus switched positions during the instability phase.

et al. (2008) showed that an initially empty EKB can be filled during the high-eccentricity phase of Neptune after the LHB. The MMSN and the Nice model are capable of explaining numerous observations of the Solar System, therefore a goal is to join these models self-consistently (e.g., Desch, 2007; Crida, 2009).

### 1.3. Debris Disks and the EKB in Context

In the region of the Kuiper belt our Solar System contains planetesimals that have survived planetary formation (and the LHB). Similar belts of small bodies around other stars are expected, too. These are the natural aftermath of the evolution of dense protoplanetary disks that may or may not result in formation of planets (see, e.g., Wyatt, 2008; Krivov, 2010, for recent reviews) and are called *debris disks*. Indeed, they are known to be ubiquitous around main-sequence stars and are composed of left-over planetesimals and smaller debris produced in mutual collisions, and it is the tiniest, dust-sized fragments that are evident in observations through thermal radiation and scattered stellar light.

Our Solar System's debris disk contains two dust parent belts. The main asteroid belt between two groups of planets, terrestrial and giant ones, where the strong perturbations by the nearby Jupiter prevented the formation of a planet (e.g., Safronov, 1969; Wetherill, 1980), and the EKB, where the density of the outer Solar nebula was too low for planet formation (see Sec. 1.2). Both the asteroid belt and the Kuiper belt have dense internal structure due to the gravitational influence of giant planet(s) on the dynamics of the bodies, predominantly by Jupiter and Neptune, respectively. They include non-resonant and resonant families, as well as various objects in transient orbits ranging from detached and scattered Kuiper belt objects through Centaurs to Sun-grazers. Short-period comets, another tangible population of small bodies in the inner Solar System, must be physically related to the Kuiper belt that acts as their reservoir (Quinn et al., 1990). Asteroids and short-period comets together are sources of interplanetary dust, observed in the planetary region, although their relative contribution to the dust production remain uncertain (Grün et al., 2001). This complex system structure was likely quite different in the past. As described above it is argued that the giant planets and the Kuiper belt have originally formed in a more compact configuration (Gomes et al., 2005), and that it went through a short-lasting period of dynamical instability.

As the amount of material and spatial dimensions of the EKB surpass by far those of the asteroid belt and the population of short-period comets, it is the EKB and its presumed collisional debris that should be referred to as the debris disk of the Solar System (see also

discussion in Sec. 6.3). Ironically, the observational status of the Solar System's debris disk is the opposite of that of the debris disks around other stars. In the former case, we can observe the planetesimals, but there is no certain detection of their dust at least in thermal emission so far (Gurnett et al., 1997; Landgraf et al., 2002). In the latter case, as mentioned above, it is dust that can be observed.

An obvious difference between the debris disks detected so far around other stars and our Solar System's debris disk is the total mass (and thus, also the amount of dust). Müller et al. (2010) for example infer several Earth masses as the total mass of the Vega debris disk, whereas the Kuiper belt mass is reported to be below one-tenth of the Earth mass (Bernstein et al., 2004; Fuentes & Holman, 2008). As a result, were the Solar System observed from afar, its debris dust would be far below the detection limits (see Chapter 5). However, a number of debris disks around Sun-like stars that are coeval with or even older than the Sun have been detected. Booth et al. (2009) analyze “dusty consequences” of a major depletion of the planetesimal populations in the Solar System at the LHB phase. They point out that the pre-LHB debris disk of the Sun would be among the brightest debris disks around solar-type stars currently observed. Future, more sensitive observations (for instance, with the Herschel Space Observatory; Pilbratt et al., 2010) should detect lower-mass disks, reducing (but not yet bridging) the gap between dusty debris disks around other stars and tenuous debris disks as in the present-day Solar System.

The observational evidence for the EKB dust is limited to scarce in-situ detections of dust in the outer Solar System by a few spacecraft (Voyager 1 and 2, Pioneer 10 and 11, and New Horizons), partly with uncalibrated “chance detectors” (Gurnett et al., 1997; Landgraf et al., 2002; Poppe et al., 2010). In addition, there are rough upper limits on the amount of dust from the non-detection of thermal emission of the EKB dust on a bright zodiacal light foreground (Backman et al., 1995). Dikarev et al. (2009) explored the question whether the flux of the EKB dust can contribute to the anomalies found by the WMAP (Wilkinson Microwave Anisotropy Probe) mission in the cosmic microwave background radiation maps. They estimated that about one third of the magnitude of the anomalous flux can indeed stem from the EKB dust. The results of a similar analysis of the WMAP data made by Ichikawa & Fukugita (2011) show that small bodies in the Solar System can contribute to the multipole coefficients of the cosmic microwave background anisotropy, however, no positive detection of this contribution was found. Therefore, it was possible to put constraints on the total mass of the EKB to  $M_{\text{EKB}} < 0.2M_{\oplus}$  (with a bulk density of  $\rho = 2.5 \text{ g cm}^{-3}$ ). Furthermore, Teplitz et al. (1999) used different assumptions for albedo, particle size and distances to investigate the mass limits of the total EKB mass

and the dust mass, including the spectrum shape produced by the dust. They found ranges of the values for the total mass of a factor of 30 and for the dust mass even a factor of 70. Their results include estimates of the depletion of dust due to a passage of the sun through a giant molecular cloud. Greaves & Wyatt (2010) give constraints on the non-detection of the EKB dust flux for COBE at  $70\ \mu\text{m}$ .

## 1.4. Aims

Given the lack of observational data, the only way to access the properties of the EKB dust is by modeling. This modeling takes the known EKB populations to be parent bodies for dust and uses collisional models to generate dust distributions (Stern, 1995, 1996; Kuchner & Stark, 2010).

The main goal of this work is to develop a more realistic model of the EKB dust disk than was done before (e.g., Stern, 1995, 1996).

*Instead of modeling from dust to planetesimals, as done for extrasolar debris disks, we model from planetesimals to dust, using the same kind of collisional models. Hence, the modeling of the Solar System's debris disk can help to understand the link between planetesimals and dust (and vice versa) and so serve as a natural reference model for all debris disks. Furthermore, the role of the parent bodies can be investigated in more detail which may provide useful information for planet formation theories.*

The first step to accomplish this task is to analyze the currently known objects in the EKB and work out an algorithm to correct their distributions for observational selection effects and try to reconstruct the properties of the expected “true” EKB. Advantage is taken of the fact that — unlike with other debris disks and unlike at the time when the first collisional models of the EKB dust were devised — more than a thousand EKB objects, acting as dust parent bodies of the Solar System's debris disk, are now known. This is done in Chapter 3.

Second, the objects of the “true” EKB are treated as dust parent bodies. In Chapter 4 we use the common modeling attempt where all objects in the EKB are in collisional equilibrium and simulate the dust production and evolution with a statistical code. A detailed analysis of the influence of the mass of the parent bodies and the Poynting-Robertson effect is made and the results are presented. We show that this modeling attempt violates the upper non-detection limit by the COBE spacecraft. As a consequence, an EKB in full collisional equilibrium can be rejected.

Therefore, in Chapter 5 a different extrapolation ansatz for objects smaller than  $\sim 10$  km is made. In addition, the influence of planets (resonant trapping and gravitational scattering) is estimated and implemented into the outcome of the numerical simulations as well as the possible effect of ice sublimation. Finally, a detailed comparison of the model with the spacecraft in-situ measurements is done, including the first results of New Horizons (Poppe et al., 2010; Han et al., 2011). The thermal emission constraints by COBE (Greaves & Wyatt, 2010, and references therein) are not violated. Conclusions, a discussion and a scientific outlook are presented in Chapter 6.

## 2. Theoretical Background

“It is the theory that decides what can be observed.”

---

Albert Einstein (1879-1955)

The orbital elements and conversions introduced in Section 2.1 are used to develop the debiasing algorithm described in Chapter 3. Subsequent effects and forces explained in Section 2.2 are important to understand the orbital motion of dust grains exposed to stellar radiation. They are implemented in the simulations (Chapters 4 and 5). Since collisions are the main source of dust, Section 2.3 is the key to understand our collisional simulations and therefore is used to obtain the results of Chapters 4 and 5. The technique described in Section 2.5 is used to calculate thermal fluxes from the disk models in Chapters 4 and 5.

### 2.1. Keplerian Orbits

All bound objects in the Solar System revolve around the Sun (or another bound object) in an elliptic orbit. To characterise this ellipse in space and the current position of an object on this ellipse, a set of six orbital elements has to be defined. The set of these elements is not unique, and the set presented here in Fig. 2.1 was chosen and used by the virtue of being the set best suited to address the dynamical problems addressed in this thesis:

- I. The semimajor axis  $a$  is the half of the longest diameter of the ellipse.
- II. The (numerical) eccentricity  $e$  is the ratio of the distance between the center and the focus of an ellipse and the semimajor axis and can be interpreted as the deviation of the ellipse from a circle.
- III. The inclination  $i$  is the angle between the orbital plane and the ecliptic plane in the Solar System.
- IV. The longitude of the ascending node  $\Omega$  is the angle between the direction to a reference point, which is the vernal equinox  $\Upsilon$ , and the ascending node  $\Omega$  measured in the ecliptic.

- V. The argument of pericenter  $\omega$  denotes the angle between the direction to the pericenter (pericentric distance  $q = a(1 - e)$ ) and the ascending node.
- VI. Finally, the true anomaly  $\varphi$  gives the angle between the direction of the pericenter and the current position of the object measured from the Sun. To simplify some calculations, other anomalies like the eccentric or mean anomaly  $E$  or  $M$  are used.

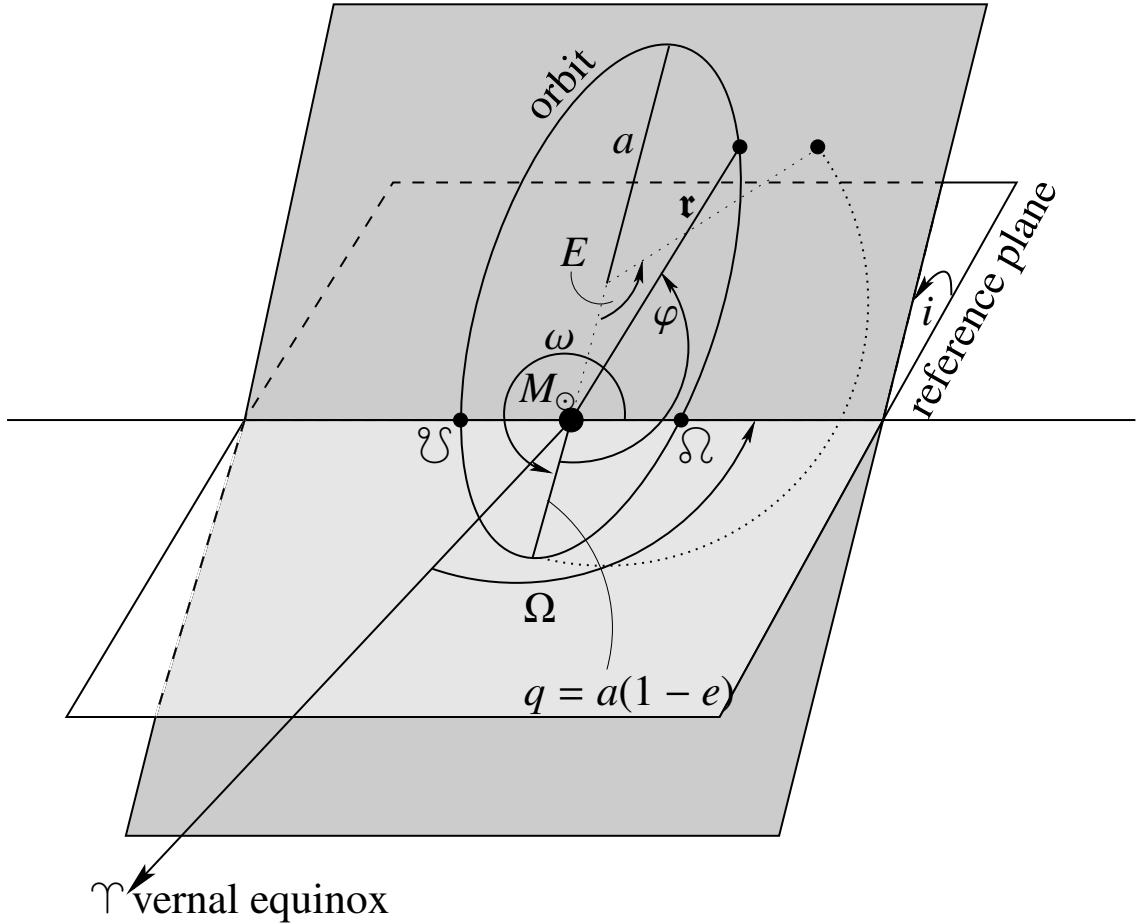


Figure 2.1.: An example of a general orbit in three dimensions with orbital elements  $a$  (semimajor axis),  $e$  (eccentricity),  $i$  (inclination),  $\Omega$  (longitude of the ascending node),  $\omega$  (argument of pericenter), and  $\varphi, E$  (true, eccentric anomaly, respectively)

With this set the Cartesian position vector of an object is found to be

$$\mathbf{r} = \frac{a(1 - e^2)}{1 + e \cos \varphi} \begin{pmatrix} \cos \Omega \cos(\omega + \varphi) - \sin \Omega \sin(\omega + \varphi) \cos i \\ \sin \Omega \cos(\omega + \varphi) + \cos \Omega \sin(\omega + \varphi) \cos i \\ \sin(\omega + \varphi) \sin i \end{pmatrix}. \quad (2.1)$$



The absolute distance from the Sun is given by

$$r = \frac{a(1 - e^2)}{1 + e \cos \varphi} = a(1 - e \cos E), \quad (2.2)$$

with the conversion from true to eccentric anomaly

$$\tan \frac{\varphi}{2} = \sqrt{\frac{1+e}{1-e}} \tan \frac{E}{2}. \quad (2.3)$$

Obviously,  $\varphi = E$  for  $e = 0$ . For bound objects the eccentricity is  $0 \leq e < 1$ , reaching  $e = 1$  for an unbound parabolic orbit and exceeding unity for unbound hyperbolic orbits. Due to interaction with the stellar radiation and wind (see Sec. 2.2) it is possible that the orbit is opened outward from the star and the eccentricity becomes  $e < -1$ .

## 2.2. Effects and Forces on Dust Grains

For big objects like planets, moons, or planetesimals life is quite easy, revolving around the Sun, feeling its heat and gravity and the gravity of the other bodies. Small dust grains, however, are not only heated by the Sun's radiation but affected on their orbital motion. This section gives an overview over the important forces and effects implemented in this thesis. Additional effects like the Lorentz, the Yarkovski force or the YORP-effect (e.g., Gustafson, 1994; Bottke et al., 2000; Lowry et al., 2007, and references therein) affect mostly very small  $s \ll 1 \mu\text{m}$  or big objects  $s > 1 \text{m}$  on very long timescales and were not taken into account.

### 2.2.1. Gravity

The fundamental (but though the weakest) force in the Universe is the gravity. Newton's law (Newton, 1687) describes the force on a particle with mass  $m$  in the gravitational field of a central body with mass  $M_\star$

$$\mathfrak{F}_g = -G \frac{mM_\star}{r^3} \mathbf{r}. \quad (2.4)$$

That leads to bound orbits of planets and planetesimals around a star.  $G$  is the newtonian gravitational constant and  $r$  the distance of the particle to the star.

Planetary (gravitational) effects are scattering, which can result in gaps in the disk, warping or stirring, trapping into mean-motion resonances, e.g., the 3:2 resonance of

Neptune with Pluto, and secular perturbations. These effects can result in observable signatures in the debris (or protoplanetary) disk and conclusion of embedded planets can be drawn (e.g., Liou & Zook, 1999; Ozernoy et al., 2000; Wolf et al., 2002a; Freistetter et al., 2007; Wolf et al., 2007; Wolf, 2008).

### 2.2.2. Interaction of Grains with Radiation

Photons (or radiation) can interact with grains in two different ways: they can be scattered or absorbed. If a photon is scattered, its direction of motion is changed and if it is absorbed, its energy is dissipated into thermal energy, the grain is heated and eventually will re-emit photons with a characteristic spectrum.

To determine the extinction cross section  $C_{\text{ext}}$  for grains, one can simply use the superposition of the scattering cross section  $C_{\text{sca}}$  and the absorption cross section  $C_{\text{abs}}$  to  $C_{\text{ext}} = C_{\text{sca}} + C_{\text{abs}}$ .

Usually, the *efficiencies* for extinction, scattering and absorption are used, which are defined as  $Q_{\text{ext,sca,abs}} = C_{\text{ext,sca,abs}}\sigma^{-1}$  with  $\sigma = \pi s^2$  being the geometrical cross section for spherical particles with radius  $s$ .

The measure of momentum transfer from photon to particle, the radiation pressure efficiency, reads

$$Q_{\text{pr}} = Q_{\text{ext}} - \langle \cos \vartheta \rangle Q_{\text{sca}}. \quad (2.5)$$

The factor  $\langle \cos \vartheta \rangle$ , the asymmetry parameter, distinguishes between forward ( $0 < \langle \cos \vartheta \rangle < 1$ ) and backward scattering ( $-1 < \langle \cos \vartheta \rangle < 0$ ).  $Q_{\text{pr}}$  is a function of the wavelength and the shape (radius) of the particle. Gustav Mie (1868–1957) used the assumption that particles are spherical, homogeneous, and isotropic. With this assumption he found an analytic solution for the interaction between radiation and spherical particles. This solution is known and referred to as Mie theory. Obviously, such perfect grains do not exist in reality. A real object usually is not a perfect sphere, but can be porous, crystalline or amorphous. The absorption and emission properties of such grains depend on the internal energy levels and are too complex for an analytical treatment, so Mie theory fails to reproduce the measured spectra from amorphous and crystalline materials. The wavelength averaged dependency of  $Q_{\text{pr}}$  on the size for different materials is shown in the left panel of Fig. 2.2.

A “typical” material composition for transneptunian objects (TNOs) is difficult to find. For a number of bright EKBOs the surface composition has been measured (see, e.g., Barucci et al., 2008, for a recent review). These objects turned out to have surfaces with very different spectral reflectances (i.e. colors, e.g., Trujillo & Brown, 2002; Doressoundi-

ram et al.,2005; Jewitt et al.,2007; Peixinho et al., 2008; see also Thébault & Doressoundiram, 2003). Some objects show no diagnostic spectral bands, while others have spectra showing signatures of various ices (such as water, methane, methanol, carbon monoxide, and nitrogen). The diversity in the spectra suggests that these objects represent a substantial range of original bulk compositions, including ices, silicates, and organic solids. As a compromise, the material used in this work is the so-called Astronomical Silicate (astrosil), which is a synthetic material (Laor & Draine, 1993), together with ice (Warren, 1984) in a volume ratio of 1:1 (Chapter 5). For optical constants of other materials the reader is referred to the Heidelberg-Jena-St. Petersburg Database of Optical Constants (Henning et al., 1999).

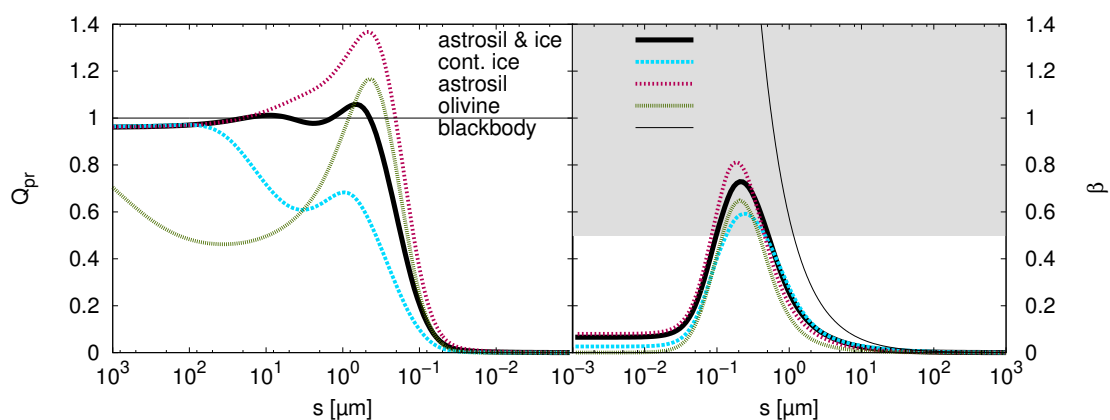


Figure 2.2.: Left: Dependency of  $Q_{pr}$  on the size for different materials averaged over wavelengths. When  $Q_{pr} \sim 1$  the material can be assumed to be a blackbody radiator. The volume ratio of astrosil & ice is 50% astrosil and 50% ice, and for contaminated ice 10% astrosil and 90% ice. Right:  $\beta$ -value for different sizes and the same materials as in the left panel. Grains in the gray shaded area have  $\beta > 0.5$  and are unbound.

### 2.2.3. Radiation Pressure and Poynting-Robertson Drag

The direct radiation pressure force acts radially away from the star and carries momentum (and energy) onto particles, counteracting the star's gravity. The ratio between radiation pressure and gravity is denoted and defined by

$$\beta := \frac{|\mathfrak{F}_{rp}|}{|\mathfrak{F}_g|}. \quad (2.6)$$

The advantage of this definition is that (in an optically-thin disk) the so-called  $\beta$ -ratio is independent of the distance to the star, since both forces are proportional to  $r^{-2}$ . Following Burns et al. (1979),  $\beta$  can be written as

$$\beta = \frac{3L_{\star}\langle Q_{\text{pr}}\rangle}{16\pi GM_{\star}c s \rho}, \quad (2.7)$$

where  $L_{\star}$  is the luminosity of the star,  $\langle Q_{\text{pr}}\rangle$  is the radiation pressure efficiency of a spherical grain averaged over wavelength and size,  $\rho$  the bulk density of the particle, and  $c$  the speed of light.

If  $Q_{\text{pr}} = 1$ , i.e. a particle absorbs *all* incident radiation, it is called *blackbody*. This is a good approximation as long as the particle's size is large compared to the wavelength. Then  $\beta$  can be written as

$$\beta = 0.574 \frac{L_{\star}}{L_{\odot}} \frac{M_{\odot}}{M} \frac{1 \text{ g cm}^{-3}}{\rho} \frac{1 \mu\text{m}}{s}, \quad (2.8)$$

with  $L_{\odot}$  and  $M_{\odot}$  being the luminosity and mass of the Sun, respectively. As stated above, the radiation pressure counteracts gravity and with help of the  $\beta$  ratio the resulting gravitational force reads

$$\mathfrak{F}_{\text{total}} = \mathfrak{F}_{\text{G}} + \mathfrak{F}_{\text{rp}} = -G \frac{mM_{\star}(1 - \beta)}{r^3} \mathbf{r}. \quad (2.9)$$

The particle “sees” the reduced, effective stellar mass  $M_{\text{eff}} = M_{\star}(1 - \beta)$ . For different values of  $\beta$  the grain can move on bound orbits (ellipses), parabolae and hyperbolae. If  $\beta > 1$  the effective mass becomes  $M_{\text{eff}} < 0$ , i.e. the particle moves on a anomalous hyperbola. Fig. 2.3 shows the possible orbits of a  $\beta$ -particle when released from a parent body. The value  $\beta = 0.5$  is often referred to as the blowout limit because the eccentricity of such a particle (when released from a parent body with  $e = 0$ ) becomes 1. Such grains are often called  $\beta$ -meteoroids. Typical  $\beta$ -values for different materials are shown in the right panel of Fig. 2.2.

As stated previously, “the radiation pressure force acts radially from the star”. Since the speed of light is finite, radiation pressure also has a tangential component, dependent on the velocity of the particle. A vivid explanation is that the particle feels a “headwind”, that reduces its energy and forces the particle to spiral inward. This drag force is named after John Henry Poynting (1852–1914) and Howard Percy Robertson (1903–1961), who first introduced and calculated this effect in terms of special relativity<sup>11</sup>. The resulting

<sup>11</sup>Poynting described the effect in terms of the aether theory.

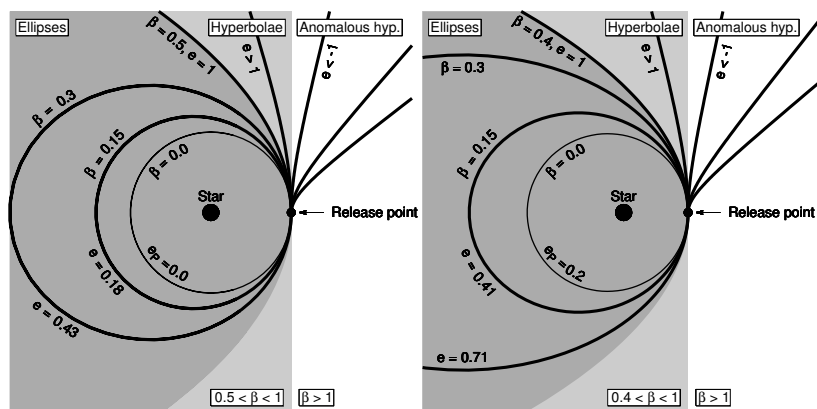


Figure 2.3.: Possible orbits of  $\beta$ -particles, released from the pericenter of a parent body. *Left.* The eccentricity of the parent body is  $e_p = 0$ . *Right.* The parent body's eccentricity is  $e_p = 0.2$ .

Poynting-Robertson drag force (P-R force or P-R effect) is expressed by

$$\mathfrak{F}_{\text{PR}} = -\frac{GmM_\star\beta}{r^2} \left[ \frac{\mathbf{v}\mathbf{r}}{cr} + \frac{\mathbf{v}}{c} \right]. \quad (2.10)$$

In total, the radiative force reads (Burns et al., 1979)

$$\mathfrak{F}_{\text{rad}} = \frac{GmM_\star\beta}{r^2} \left[ \left(1 - \frac{\dot{r}}{c}\right) \frac{\mathbf{r}}{r} - \frac{\mathbf{v}}{c} \right]. \quad (2.11)$$

Most of the debris disks observed to date (Wyatt, 2005) are very massive and the lifetime of particles are determined by collisions rather than transport effects like P-R drag. Therefore, dust transport via drag forces is usually neglected. However, facilities like the Herschel observatory are able to detect debris disks in which transport effects “play a notable role”, e.g., in the debris disk around HD 207129 (Löhne et al., 2012). Collision-dominated debris disks have been extensively modeled both analytically and numerically (Thébault et al., 2003; Krivov et al., 2006; Strubbe & Chiang, 2006; Thébault & Augereau, 2007; Wyatt et al., 2007; Löhne et al., 2008; Müller et al., 2010). As we will see later (Chapter 5) the situation in the Solar System is different. The total mass of the Kuiper belt is small, transport becomes important and *cannot* be neglected anymore. This holds especially for small particles like dust, because the P-R drag is size dependent and more effective for small objects.

### 2.2.4. Stellar Wind Drag

A similar drag effect on particles is the *stellar wind drag*. It is caused by the same reason as the P-R force, but with (charged) particles instead of photons. Therefore, a  $\beta$  ratio analog to Eq. 2.6 can be defined as

$$\beta_{\text{sw}} := \frac{|\mathfrak{F}_{\text{wp}}|}{|\mathfrak{F}_{\text{G}}|} = \frac{3\dot{M}_{\star}v_{\text{sw}}}{16\pi GM_{\star}sq}. \quad (2.12)$$

The velocity of the wind particles in the Solar System is  $v_{\text{sw}} = 300 \dots 800 \text{ km s}^{-1}$  and the stellar mass loss rate is  $\dot{M}_{\odot} = 2 \times 10^{-14} M_{\odot} \text{ yr}^{-1}$  (Allen, 1973). As corpuscular analog to Eq. 2.11 the wind drag force can be written as

$$\mathfrak{F}_{\text{sw}} = \frac{GmM_{\star}\beta_{\text{sw}}}{r^2} \left[ \left( 1 - \frac{\dot{r}}{v_{\text{sw}}} \right) \frac{\mathbf{r}}{r} - \frac{\mathbf{v}}{v_{\text{sw}}} \right]. \quad (2.13)$$

In the Solar System the wind drag is approximately 30% of the P-R drag (Gustafson, 1994). For late type stars or stars with a strong stellar wind the wind drag becomes more effective and overpowers the P-R drag. Reidemeister et al. (2011) showed for  $\varepsilon$  Eridani, a K2V star, that strong transport mechanisms can be important even for its massive disk.

## 2.3. Collisions

In the protoplanetary disk phase of a system gas and dust is canonically assumed to be present in a ratio of 100:1 (Hildebrand, 1983). The gas damps the relative velocities of the dust particles, so collisions are not disruptive and agglomeration can occur, planetesimals or even giant planets can form (cf. Sec. 1.2). This gas, however, is removed from the system approximately 3...6 Myr after stellar birth (e.g., Haisch et al., 2001; Hernández et al., 2009). Within this time planet formation has to be finished and sticking collisions will become cratering or even completely disruptive. Hence, smaller fragments are produced. Such a fragmenting collisional event on an asteroid/comet (P/2010 A2 LINEAR) was reported by Snodgrass et al. (2010), Jewitt et al. (2011), and Hainaut et al. (2012).

There are several different collisional possibilities which can be summarized as follows:

- I. Disruptive collision. The target and the projectile are destroyed.
- II. Cratering collision. The target is cratered and the projectile is destroyed.
- III. Cratering collision. The target and the projectile are cratered.
- IV. Bouncing collision. Both colliders stay intact and are separated again.
- V. Sticking collision. The colliders are bound together.

Now, we want to describe these possibilities in more detail. For a collision, independent of whether it is cratering, disruptive or sticking, at least two colliders are needed. Following the notation of Krivov et al. (2005) and using index “t” for target and “p” for projectile the impact energy of two colliders with masses  $m_t$  and  $m_p$  is given by

$$E_{\text{imp}} = \frac{1}{2} \frac{m_t m_p}{m_t + m_p} v_{\text{imp}}^2 \quad (2.14)$$

where  $v_{\text{imp}}$  is the impact velocity, which can be approximated with the keplerian velocity  $v_K$  roughly to

$$v_{\text{imp}} = e v_K. \quad (2.15)$$

A collision is called *disruptive* (or destructive) when the largest fragment’s mass is smaller than half of the target’s mass. Thus, a critical (dispersal) impact energy can be defined where a collision becomes disruptive:

$$E_{\text{imp}} > E_D. \quad (2.16)$$

To eliminate the mass dependence on the impact energy the specific energy for dispersal

$$Q_D^* = \frac{E_D^*}{m_{t/p}} \quad (2.17)$$

is introduced, which is dependent on the radius  $s$  of the object and the material. This dependency can be expressed as the sum of two power laws (Benz & Asphaug, 1999):

$$Q_D^*(s) = A_s \left( \frac{s}{1 \text{ m}} \right)^{3b_s} + A_g \left( \frac{s}{1 \text{ km}} \right)^{3b_g}. \quad (2.18)$$

These two regimes are denoted as strength (index  $s$ ) and gravity (index  $g$ ) regime. The former is dominated by inter-molecular forces, e.g., covalent-, dipole-, hydrogen bonds, and van-der-Waals forces. The gravity regime, corresponds to larger objects (typically  $s > 300$  m) where self-gravity is the dominating force of material bounding. For basalt  $A_s = 0.6 \dots 1.7 \times 10^7 \text{ erg g}^{-1}$ ,  $A_g = 0.5 \dots 0.9 \times 10^7 \text{ erg g}^{-1}$ ,  $b_s \approx -0.12$ , and  $b_g \approx 0.45$ . For ice  $A_s = 0.3 \dots 0.9 \times 10^7 \text{ erg g}^{-1}$ ,  $A_g = 0.17 \dots 0.22 \times 10^7 \text{ erg g}^{-1}$ ,  $b_s \approx -0.13$ , and  $b_g \approx 0.41$  (Benz & Asphaug, 1999). In this work we use values thought to be typical of low-temperature ice:  $A_s = 10^6 \text{ erg g}^{-1}$ ,  $A_g = 2 \times 10^6 \text{ erg g}^{-1}$ ,  $3b_s = -0.37$  and  $3b_g = 1.38$ . A disadvantage of this assumption is that it does not take into account the velocity

dependence on  $Q_D^*$ . For detailed description for a velocity dependent  $Q_D^*$  the reader is referred to Stewart & Leinhardt (2009).

To describe the outcome of a collision several parameters have to be defined. One is the mass of *the* largest fragment<sup>12</sup>  $m_x$ , for which impact experiments yielded to an empirical function

$$\frac{m_x}{m_p + m_t} = \frac{1}{2} \left( \frac{m_t Q_D^*(m_t) + m_p Q_D^*(m_p)}{E_{\text{imp}}} \right)^c, \quad (2.19)$$

where the slope ranges from  $c \approx 1.24$  for basalt (Fujiwara et al., 1977) to  $c \approx 0.91$  for ice (Arakawa, 1999).

If the impact energy does not exceed the critical energy for disruption then the target stays intact except for a crater with the ejected mass  $m_{\text{eject}}$  which escapes to infinity. The same holds for the projectile, if the impact energy is smaller than its dispersal threshold. Thus, these events are called *cratering* collisions. According to the model of Wyatt & Dent (2002) and Thébault & Augereau (2007) the ejected mass for large craters, comparable with the size of the target reads

$$m_{\text{eject}} = 0.5 \frac{E_{\text{imp}}}{Q_D^*}. \quad (2.20)$$

To obtain a mass distribution after the collisional event the remnant mass  $m_{\text{rem}}$  and the ejected mass  $m_{\text{eject}}$  are defined. Obviously the total mass is conserved

$$m_t + m_p = m_{\text{rem}} + m_{\text{eject}}. \quad (2.21)$$

For a cratering collision the mass of the largest remnant is defined as

$$m_x = m_{\text{eject}} \frac{2 - \eta}{\eta - 1}. \quad (2.22)$$

Dependent on the collisional regime, remnant and excavated mass can be calculated as follows:

$$m_{\text{rem}} = \begin{cases} m_t + m_p & \text{in a sticking collision,} & (2.23) \\ 0 & \text{in a disruptive collision,} & (2.24) \\ m_t - m_{\text{eject},t} & \text{target cratered, projectile destroyed,} & (2.25) \\ m_t + m_p - m_{\text{eject},t} - m_{\text{eject},p} & \text{target and projectile cratered,} & (2.26) \end{cases}$$

<sup>12</sup>Meant literally, i.e. there is only one largest fragment.



and

$$m_{\text{eject}} = \begin{cases} 0 & \text{in a sticking collision,} & (2.27) \\ m_p + m_t & \text{in a disruptive collision,} & (2.28) \\ m_p + m_{\text{eject,t}} & \text{target cratered, projectile destroyed,} & (2.29) \\ m_{\text{eject,t}} + m_{\text{eject,p}} & \text{target and projectile cratered.} & (2.30) \end{cases}$$

Then the fragment distribution  $g(m)$  can be written as

$$g(m) = (2 - \eta)(m_{\text{eject}}) \left( \frac{m_x}{m} \right)^\eta \frac{1}{m_x^2} \Theta(m_x - m) + \delta(m - m_{\text{rem}}) \quad (2.31)$$

with the Heaviside and Dirac functions  $\Theta(x)$  and  $\delta(x)$ <sup>13</sup>, respectively. The normalization of  $g(m)$  is

$$M(< m) = \int_0^m g(m') m' dm' = \begin{cases} m_{\text{eject}} \left( \frac{m_x}{m} \right)^{2-\eta} & \text{for } m < m_x \\ m_{\text{eject}} & \text{for } m_x \leq m < m_{\text{rem}} \\ m_p + m_t & \text{for } m \geq m_{\text{rem}}. \end{cases} \quad (2.32)$$

Krivov et al. (2005) showed that  $\eta < 2$ , while impact experiments of Fujiwara (1986, and references therein) give values for the parameter  $\eta$  between 1.5 . . . 2.0 with  $\eta = 1.83$  being the “classical” value which corresponds to a differential size distribution of  $N(s) ds \propto s^{-3.5} ds$ . This slope is the value of the (differential) size distribution of a debris disk in collisional equilibrium (Dohnanyi, 1969).

There are other collisional outcomes when the impact energy is decreased even further. Bouncing or bounding interactions between two colliders can occur. Both objects are neither destroyed nor cratered, and depending on the impact velocity and energy are separated from each other or stick together. Laboratory experiments by Beitz et al. (2011, and references therein) show that head-on bouncing is only possible for centimeter-sized objects at velocities below  $0.4 \text{ m s}^{-1}$ . Bouncing can also occur in grazing collisions or in a rather unlikely event of head-on bouncing where the momenta are reversed. Both objects would suffer high stress in such an incident.

---

<sup>13</sup>See Eq. 2.42.

## 2.4. Kinetic Theory

Although computational power increased drastically in the last years, physical models of stellar systems cannot be calculated by numerical N-body integrations alone. Some models require statistic approaches like the axisymmetric modeling of debris disks and their spatial and size distribution of objects as done in this work. Of course N-body integrations and statistical models have advantages and disadvantages. N-body simulations allow us to follow individual objects, for example, in stability analysis of planetary systems (e.g., Reidemeister et al., 2009) with, e.g., the Mercury6 code (Chambers, 1999). Wada et al. (2007, 2008, 2009) performed N-body integrations to investigate (head-on) collisions of two individual objects which are each composed of numerous particles. Also, structures in disks caused by planetary perturbations can be investigated (e.g., Wyatt, 2003, 2006; Kuchner & Stark, 2010, and references therein). In contrast to that, a statistical approach has to be used to model a complete debris disk with objects ranging in size from sub-micrometer up to several thousands of kilometer. A summary of the detailed description of the statistical approach used in Krivov et al. (2000, 2005); Löhne (2008) is given in this Section.

All concepts and ideas introduced here are the heart of our collisional code (*ACE*, see description in Section 4.1). Therefore, this Section gives an overview of the equations *ACE* solves numerically to simulate the Edgeworth-Kuiper belt debris disk (Chapters 4 and 5).

### 2.4.1. Number Density and Phase Space Variables

At first, a general quantity “phase space number density” is defined  $n(\mathbf{p}, s, t)$ , which is dependent on the cartesian coordinates and the corresponding velocities  $\mathbf{p} = (x, y, z, \dot{x}, \dot{y}, \dot{z})$ , the radius of an object  $s$ , and the time  $t$ . More descriptively,  $n(\mathbf{p}, s, t) d\mathbf{p} ds$  is the number of particles with arguments  $[\mathbf{p}, \mathbf{p} + d\mathbf{p}]$  and  $[s, s + ds]$ . Another important quantity is the number density denoted with the same letter  $n$  but with different dependencies.  $n(s, t)$  is simply obtained by integrating  $n(\mathbf{p}, s, t)$  over  $\mathbf{p}$ :

$$n(s, t) = \int n(\mathbf{p}, s, t) d\mathbf{p}. \quad (2.33)$$

A straightforward definition is the total number of objects  $N(t)$  with

$$N(t) = \int n(s, t) ds. \quad (2.34)$$

In celestial mechanics it is useful to work with orbital elements (as defined in Sec. 2.1) instead of cartesian coordinates. The translation into other coordinate systems is achieved the usual way by multiplying  $n(\mathbf{p}, s, t)$  with the corresponding Jacobian  $J$

$$n(\mathbf{p}, s, t) = Jn(\mathbf{p}', s, t), \quad (2.35)$$

with  $\mathbf{p}' = (a, e, i, \Omega, \omega, \varphi)$  and without changing relations 2.33 and 2.34. The Jacobian for the conversion from cartesian coordinates to orbital elements (using the mean anomaly  $M$  instead of the true anomaly  $\varphi$ ) is<sup>14</sup>

$$J = \left| \frac{\partial(x, y, z, \dot{x}, \dot{y}, \dot{z})}{\partial(a, e, i, \Omega, \omega, M)} \right| = \frac{1}{2} \sqrt{a(GM_\star)^3} e \sin i, \quad (2.36)$$

with the mass of the star  $M_\star$ .

By using the transformation relation 2.35 it is easy to transform  $n(\mathbf{p}, s, t)$  into the mass density  $n(\mathbf{p}, m, t)$  in the following way

$$n(\mathbf{p}, m, t) = \left| \frac{ds}{dm} \right| n(\mathbf{p}, s, t). \quad (2.37)$$

As phase space variables the grain size  $s$  and the orbital elements vector  $\mathbf{p}$  are used, following Krivov et al. (2005). In order to reduce the set of 8 variables to 4,  $(i, \Omega, \omega, \varphi)$  are averaged over. This assumption leads to the simplification of an azimuthally and vertically symmetric disk. The phase space density then reads

$$n(a, e, s, t) = \iiint_{\varphi \ \omega \ \Omega \ i} n(\mathbf{p}, s, t) \, di \, d\Omega \, d\omega \, d\varphi. \quad (2.38)$$

## 2.4.2. The Master Equation

Having defined the important variables and the number density the focus in this Section is centered on the evolution of the latter quantity. For that purpose the “master equation”<sup>15</sup> has to be solved

$$\frac{dn(\mathbf{p}, s, t)}{dt} + \text{div}(n\dot{\mathbf{p}}) = \left( \frac{dn}{dt} \right)_{\text{gain}} + \left( \frac{dn}{dt} \right)_{\text{loss}}. \quad (2.39)$$

---

<sup>14</sup>Note that this is the formal way to calculate the Jacobian. In praxis it is calculated the way described in the appendix of Krivov et al. (2006). In the code used in this thesis (*ACE*, see introduction in Sec. 4.1) we use the pericenter  $q$  instead of  $a$  to avoid issues at the boundary of the grid.

<sup>15</sup>Without the divergence it is sometimes referred to as the Boltzmann-Smoluchowski equation.

The right hand side reflects the collisional gain and loss of particles, the divergence term is needed to handle transport mechanisms like the Poynting-Robertson drag (see Sec. 2.2). The derivation of the gain and loss term is a long business with a lot of integrals, functions, substitutions, and derivatives and shall not be presented here, instead the results are given. The gain term can be written as

$$\left(\frac{dn(\mathbf{p}, s, t)}{dt}\right)_{\text{gain}} = \iiint_{s_p} \iiint_{\mathbf{p}_p} \iiint_{s_t} \iiint_{\mathbf{p}_t} f(\mathbf{p}, s, \mathbf{p}_t, s_t, \mathbf{p}_p, s_p) v_{\text{imp}}(\mathbf{v}(\mathbf{p}_t), \mathbf{v}(\mathbf{p}_p)) \sigma(s_t, s_p) \times n(\mathbf{p}_t, s_t, t) n(\mathbf{p}_p, s_p, t) \delta(\mathbf{r}(\mathbf{p}_p) - \mathbf{r}(\mathbf{p}_t)) d\mathbf{p}_t ds_t d\mathbf{p}_p ds_p. \quad (2.40)$$

The new introduced function  $f(\mathbf{p}, s, \mathbf{p}_t, s_t, \mathbf{p}_p, s_p)$  is the so-called fragment generating function. The impact velocity  $v_{\text{imp}}$  shows dependencies on the position vectors in space of two colliders.  $\sigma(s_t, s_p)$  represents the cross section of the target and the projectile and can be calculated for spherical particles simply by

$$\sigma(s_t, s_p) = \pi(s_t + s_p)^2 \quad (2.41)$$

(Krivov et al., 2006). For Dirac's  $\delta$ -function the usual definition is used (valid for all functions  $f(\mathbf{x})$ )

$$\int_{\mathbf{x}} f(\mathbf{x}) \delta(\mathbf{x} - \xi) d\mathbf{x} = \begin{cases} f(\xi) & \text{for } \xi \in \{\mathbf{x}\}, \\ 0 & \text{else.} \end{cases} \quad (2.42)$$

In a similar way the loss term can be written as

$$\left(\frac{dn(\mathbf{p}, s, t)}{dt}\right)_{\text{loss}} = \iint_{\mathbf{p}_p, s_p} v_{\text{imp}}(\mathbf{v}(\mathbf{p}), \mathbf{v}(\mathbf{p}_p)) \sigma(s, s_p) \times n(\mathbf{p}, s, t) n(\mathbf{p}_p, s_p, t) \delta(\mathbf{r}(\mathbf{p}_p) - \mathbf{r}(\mathbf{p})) d\mathbf{p}_p ds_p. \quad (2.43)$$

### 2.4.3. Orbital Elements of Fragments

In a disruptive collision the fragments inherit the sum of the momenta of the target and the projectile. Assuming maximum collisional damping, the fragments are moving in roughly one direction with zero relative velocity. The resulting momentum then is described by two conservation laws in the two-dimensional case (radial and angular component, Krivov

et al. 2005; 2006):

$$(m_p + m_t)\dot{r} = m_p\dot{r}_p + m_t\dot{r}_t, \quad (2.44)$$

$$(m_p + m_t)r\dot{\varphi} = m_pr\dot{\varphi}_p + m_tr\dot{\varphi}_t. \quad (2.45)$$

Once these equations are solved one has to take into account that the smallest produced grains ( $\beta$ -particles as introduced in Sec. 2.2.3) interact with stellar radiation, which has to be included into the calculation for the orbital elements of the collisional fragments. To accomplish this task Krivov et al. (2006) made use of the equation of the conic section (Eq. 2.2) and the derivatives

$$r\dot{\varphi} = \frac{L}{mr}, \quad (2.46)$$

$$\dot{r} = \frac{L}{mr} \left( \frac{1}{r} \frac{\partial r}{\partial \varphi} \right) \quad (2.47)$$

with

$$L = m\sqrt{pGM_\star(1-\beta)}, \quad (2.48)$$

$$\frac{1}{r} \frac{\partial r}{\partial \varphi} = \pm \sqrt{\frac{r}{p} \left( 2 - \frac{r}{a} - \frac{p}{r} \right)}, \quad (2.49)$$

$$p = a(1 - e^2). \quad (2.50)$$

$p$  is the so-called ‘‘semilatus rectum’’. Finally, to cut a long algebra short, the result is

$$\begin{aligned} \frac{r}{a} = & 2 - \frac{m_p^2}{(m_p + m_t)^2} \frac{1 - \beta_p}{1 - \beta} \left( 2 - \frac{r}{a_p} \right) - \frac{m_t^2}{(m_p + m_t)^2} \frac{1 - \beta_t}{1 - \beta} \left( 2 - \frac{r}{a_t} \right) \\ & - 2 \frac{m_p m_t}{(m_p + m_t)^2} \frac{\sqrt{(1 - \beta_p)(1 - \beta_t)}}{1 - \beta} \left[ \frac{1}{r} \sqrt{p_p p_t} \right. \\ & \left. \pm \sqrt{\left( 2 - \frac{r}{a_p} - \frac{p_p}{r} \right) \left( 2 - \frac{r}{a_t} - \frac{p_t}{r} \right)} \right], \end{aligned} \quad (2.51)$$

$$\begin{aligned} e = & \pm \left[ 1 - \frac{1}{a} \left( \frac{m_p^2}{(m_p + m_t)^2} \frac{1 - \beta_p}{1 - \beta} p_p + \frac{m_t^2}{(m_p + m_t)^2} \frac{1 - \beta_t}{1 - \beta} p_t \right. \right. \\ & \left. \left. + 2 \frac{m_p m_t}{(m_p + m_t)^2} \frac{\sqrt{(1 - \beta_p)(1 - \beta_t)}}{1 - \beta} \sqrt{p_p p_t} \right) \right]^{\frac{1}{2}}. \end{aligned} \quad (2.52)$$

Note that the sign of  $e$  matches that of  $(1 - \beta)$ , yielding for  $\beta > 1$  to anomalous hyperbolae (see Fig. 2.3). Note that scattering in mutual collisions will increase the inclination of small particles (Thébault, 2009) which is not taken into account here.

#### 2.4.4. Evolution of Debris Disks

By ignoring transport mechanisms for the moment it is possible to calculate the time dependent change of the number of particles with phase space variables  $\mathbf{p}$  and size  $s$  with Eq. 2.39. While the total number of particles changes with respect to  $\mathbf{p}$  and  $s$ , they stay constant relative to each other. If this condition is fulfilled, such a disk is called *quasi-steady state* or disk in collisional equilibrium. For brevity, the adjective “quasi” is often omitted. In an equilibrium the evolution of  $n(\mathbf{p}, s, t)$  can be expressed as

$$n(\mathbf{p}, s, t) = \tilde{n}(\mathbf{p}, s)f(t) \quad (2.53)$$

(Löhne et al., 2008). Hence, the total mass of the disk can be written as

$$M_{\text{disk}}(t) = \iint n(\mathbf{p}, s, t)m(s) d\mathbf{p} ds = f(t) \iint \tilde{n}(\mathbf{p}, s)m(s) d\mathbf{p} ds, \quad (2.54)$$

which leads to the straightforward conclusion that

$$\dot{M}_{\text{disk}} = \iint \dot{n}(\mathbf{p}, s, t)m(s) d\mathbf{p} ds = \dot{f}(t) \iint \tilde{n}(\mathbf{p}, s)m(s) d\mathbf{p} ds = \dot{f}(t)M_0 \quad (2.55)$$

where  $f(0) = 1$ .  $M_0$  denotes the initial mass of the disk and  $m(s)$  is the mass of the particle (for spherical grains it is simply  $m(s) = 4/3\pi\rho s^3$ ). Löhne et al. (2008) found that  $\dot{M}_{\text{disk}} \propto \dot{f}(t)$  and  $\dot{M}_{\text{disk}} \propto f^2(t)$  so that  $\dot{f}(t) \propto f^2(t)$ . Integration yields

$$f(t) = \frac{1}{1 + t/\tau}. \quad (2.56)$$

The integration constant  $\tau$  is the characteristic lifetime of a particle with size  $s$ . It increases with size and distance from the star. Only for

$$t \gg \tau \quad (2.57)$$

the system is in a steady-state. Since  $\tau$  is a function of size and distance large particles need more time to reach a steady-state, the same holds for particles at larger distances. Hence, it is useful to define an equilibrium up to certain sizes  $s_{\text{equi}}$ . In a steady-state disk

lost grains are replaced by collisions of larger ones which have to be replaced by still larger ones. This chain goes up to the largest planetesimals and eventually the total mass of the disk reduces. Numerical simulations of Löhne et al. (2008) showed that

$$\frac{\dot{M}_{\text{disk}}}{M_{\text{disk}}} \propto t^{-2/3 \dots -4/5} \propto r^{-4.3}. \quad (2.58)$$

Note that in tenuous disks where transport mechanisms are important,  $\dot{M}_{\text{disk}}/M_{\text{disk}}$  is proportional to  $t^{-2}$  (Dominik & Decin, 2003). Wyatt et al. (2007); Krivov et al. (2008); Löhne et al. (2008) found useful scaling laws which can be used for collision-dominated disks. For any quantity  $F(M_0, r, t)$ , which is directly proportional to a certain amount of material in any size regime, the following analytical scaling rule applies

$$F(xM_0, r, t) = xF(M_0, r, xt) \quad (x > 0). \quad (2.59)$$

The quantity  $F$  can stand, e.g., for the total disk mass, the mass of dust or the total cross section. Increasing the initial disk mass speeds up the evolution and amplifies  $F$ . In another scaling law one can shift the disk toward other distances from the star instead of changing its mass which leads to

$$F(M_0, xr, t) \approx F(M_0, r, x^{-4.3}t). \quad (2.60)$$

In contrast to Eq. 2.59 this equation is approximate. At larger distances the disk's evolution is slowed down. This can be compensated by increasing the initial mass at the same time. It is also possible to find a relation between the dust mass and the time

$$M_{\text{dust}}(M_0, r, xt) \approx x^{-(0.3 \dots 0.4)} M_{\text{dust}}(M_0, r, t). \quad (2.61)$$

The denotation “dust” is usually used for particles  $s < 1$  mm, but this scaling law is also valid for grains  $s < 100$  m, i.e. material in the strength regime.

## 2.5. Thermal Emission of Debris Disks

For the calculation of the thermal emission of debris disks it is assumed that the embedded grains are in thermal equilibrium with its surroundings. That means that they absorb the same amount of radiation which they emit. An implicit equation to calculate the equilibrium temperature  $T_g$  for spherical particles at a given distance  $r$  from the star is given by

(e.g., Backman & Paresce, 1993; Wolf & Hillenbrand, 2003):

$$r = \frac{R_\star}{2} \sqrt{\frac{\int_0^\infty Q_{\text{abs}}(\lambda, s) F_\star(\lambda, T_\star) d\lambda}{\int_0^\infty Q_{\text{abs}}(\lambda, s) B(\lambda, T_g) d\lambda}}, \quad (2.62)$$

where  $R_\star$  is the radius,  $F_\star(\lambda, T_\star)$  the flux,  $\lambda$  the wavelength, and  $T_\star$  the effective temperature of the star.  $B(\lambda, T_g)$  is the Planck function. Considering a rotationally symmetric disk with distance  $D$  from the observer, the total flux at a given wavelength can be calculated via (see Krivov et al., 2008)

$$F_{\text{total}}(\lambda) = \frac{2\pi}{D^2} \int_{T_g(r_{\text{max}})}^{T_g(r_{\text{min}})} r(T_g) B(\lambda, T_g) \frac{dr(T_g)}{dT_g} dT_g \int_{s_{\text{min}}}^{s_{\text{max}}} N(r, s) Q_{\text{abs}} s^2(\lambda, s) ds. \quad (2.63)$$

Here,  $N(r, s)$  is defined as the surface number density of grains, similar to Sec. 2.4.1. Interestingly, the fluxes are calculated with respect to the wavelength  $F(\lambda)$  whereas the measured fluxes usually are given in terms of frequency  $F(\nu)$  with the conversion relation

$$F(\nu) = \left| \frac{d\lambda}{d\nu} \right| F(\lambda) = \frac{\lambda^2}{c} F(\lambda). \quad (2.64)$$

A common unit for flux is the *Jansky* (Jy) with  $1 \text{ Jy} = 10^{-26} \text{ J s}^{-1} \text{ m}^{-2} \text{ Hz}^{-1}$ . As an example, the fluxes at  $70 \mu\text{m}$  and  $160 \mu\text{m}$  for the first four debris disks, also known as the “fabulous four”, are given in Table 2.1.

Table 2.1.: Typical fluxes for different wavelengths of some selected debris disks.

Star	$70 \mu\text{m}^\dagger$	$160 \mu\text{m}^\dagger$	Reference	Instrument
$\beta$ Pictoris	16.0 Jy	5.1 Jy	Vandenbussche et al. (2010)*	(PACS)
$\varepsilon$ Eridani	1.5 Jy	0.9 Jy	Backman et al. (2009)*	(IRAS, MIPS)
Fomalhaut	10.8 Jy	6.2 Jy	Acke et al. (2012)*	(PACS)
Vega	9.3 Jy	2.4 Jy	Heinrichsen et al. (1998)*	(ISOPHOT)

\*And references therein.  $^\dagger$  The fluxes for Vega are at  $60 \mu\text{m}$  and  $170 \mu\text{m}$ , respectively.



# 3. Planetesimals in the Kuiper belt

“If we knew exactly what to expect throughout the Solar System, we would have no reason to explore it.”

---

Poul William Anderson (1926-2001)

*The following Chapter is based on the paper Vitense et al. (2010). The analyses and results in this Chapter are the contribution of the author of this thesis. Discussions with Alexander Krivov, Torsten Löhne, Martin Reidemeister, and Sebastian Müller were appreciated.*

## 3.1. Observations and Their Biases

The EKB was predicted more than sixty years ago by Edgeworth and Kuiper and it took forty years until the first member, QB 1, was discovered (Jewitt et al., 1992). More than 1300 TNOs orbiting the Sun beyond the orbit of Neptune have been discovered to date. Table 3.1 lists most of the surveys published so far, in which new TNOs have been discovered, and key parameters of these surveys. One parameter is the area  $\Omega$  on the sky searched for TNOs. Another one is the limiting magnitude  $m_{50}$  that corresponds to the detection probability of 50%. As the detection probability drops rapidly from 100% to zero when the apparent magnitude  $m$  “crosses”  $m_{50}$ , we simply assume that an object will be detected with certainty if  $m < m_{50}$  and missed otherwise. Finally, the maximum ecliptic latitude  $\varepsilon$  and ecliptic longitude  $\alpha$  covered by each survey are listed. Where it was not given explicitly in the original papers, we estimated them to be  $\varepsilon = \sqrt{\Omega}/2$  and  $\alpha = \sqrt{\Omega}$ , assuming that the surveyed area was centered on the ecliptic. Table 3.1 shows that all campaigns can be roughly divided into two groups: deeper ones with a small sky area covered (“pencil-beam” surveys) and shallower ones with a larger area, but a smaller limiting magnitude.

The orbits of TNOs are commonly characterized by six orbital elements: semimajor axis  $a$  (or perihelion distance  $q$ ), eccentricity  $e$ , inclination  $i$ , argument of pericenter  $\omega$ , longitude of the ascending node  $\Omega$ , and mean anomaly  $M$  (see Fig. 2.1). In addition, each object itself is characterized by the absolute magnitude  $H$ , which is defined as the apparent magnitude the object would have if it was 1 AU away from the Sun and the Earth,

Table 3.1.: A list of campaigns where TNOs were found. The sky area covered ( $\Omega$ ), the number of the objects discovered ( $N$ ), the limiting magnitude ( $m_{50}$ ), an estimated half-opening angle  $\varepsilon$  (if not explicitly given in the paper), and the ecliptic longitude coverage  $\alpha$  are given. Papers that provide enough data for objects discovered in that survey to identify them in the MPC database are marked with an asterisk.

$\Omega$ [deg <sup>2</sup> ]	N	$m_{50}$	$\varepsilon$ [°]	$\alpha$ [°]	Reference
0.7	2	23.5	0.42	0.84	Irwin et al. (1995)*
1.2	7	24.85	0.55	1.1	Jewitt & Luu (1995)
3.9	12	24.2	0.99	1.97	Jewitt et al. (1996)*
4.4	3	23.2	1.05	2.1	Jewitt et al. (1996)*
0.35	1	24.6	0.30	0.59	Gladman et al. (1998)
0.049	4	25.6	0.11	0.22	Gladman et al. (1998)*
0.075	0	25	0.14	0.27	Gladman et al. (1998)
51.5	13	23.4	3.6	7.2	Jewitt et al. (1998)
0.01	2	27.94	0.05	0.1	Chiang & Brown (1999)
20.2	3	23.6	2.25	4.5	Trujillo et al. (2000)
1.5	24	24.9... 25.9	0.61	1.22	Allen et al. (2001)*
0.012	0	26.7	0.06	0.11	Gladman et al. (2001)*
0.31	17	25.93	0.28	0.56	Gladman et al. (2001)*
73	86	24.0	4.25	8.5	Trujillo et al. (2001a)*
164	3	21.1	6.40	12.8	Trujillo et al. (2001b)*
5108	19	20.7	10	255.4	Trujillo & Brown (2003)*
0.02	3	28.7	0.07	0.14	Bernstein et al. (2004)*
550	183	22.5	5	55	Elliot et al. (2005)*
8000	1 big	20... 21	10	400	Larsen et al. (2007)*
3.0	70	26.4	0.87	1.73	Fraser et al. (2008)
2.8	82	25.7	1.67	1.67	Fuentes & Holman (2008)
0.255	20	26.76	0.25	0.5	Fuentes et al. (2009)
0.33	36	26.8	0.29	0.57	Fraser & Kavelaars (2009)

and depends on the object radius and albedo. We take the orbital elements and the absolute magnitudes of all known objects from the Minor Planet Center (MPC) database<sup>16</sup> rather than from discovery papers listed in Table 3.1, because the MPC data include follow-up observations and thus provide more precise ephemerides.

Planet formation theory implies that the TNO orbits strongly concentrate towards the ecliptic plane, if the formation and evolution was unperturbed by, e.g., a passing star. Ac-

<sup>16</sup><http://www.cfa.harvard.edu/iau/lists/TNOs.html> and <http://www.minorplanetcenter.net/iau/lists/Centaurs.html> – For Fig. 3.1 (and corresponding description) the last access was on 15 June 2012. For the debiasing and the modeling we used the data from 12 October 2009 (plot and description with these data are shown in Fig. 1 of Vitense et al. 2010).

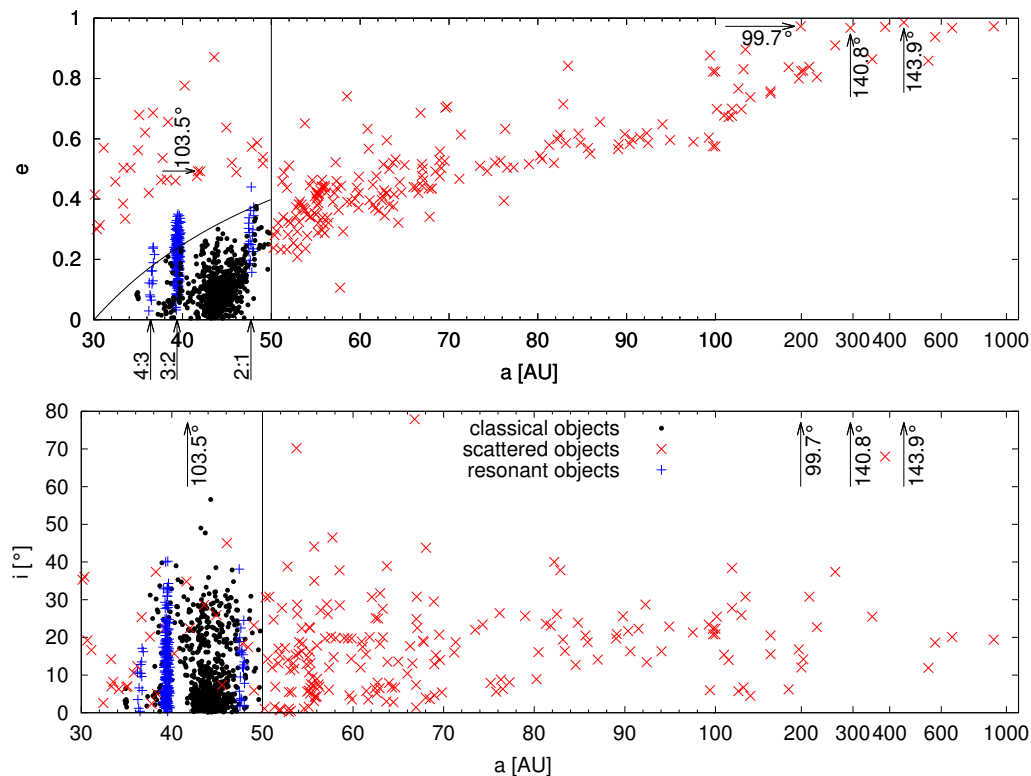


Figure 3.1.: Known TNOs in the  $a$ – $e$  plane (top) and  $a$ – $i$  plane (bottom). Different groups are shown with different symbols: 865 classical objects with dots, 235 resonant TNOs with pluses, and the remaining 160 scattered objects with crosses. Solid lines separate classical and scattered objects in our classification. Four objects with  $i > 90^\circ$  are outside the lowest panel, but are marked with arrows in both panels. Notice that the linear scale turns into a logarithmic scale at 100 AU.

cordingly, in order to increase the detection probability, the majority of the observations were made near the ecliptic, and only a few surveys covered high ecliptic latitudes. Our sample, given in Table 3.1, contains surveys with  $\varepsilon$  up to  $10^\circ$  (e.g., Trujillo et al., 2001a; Trujillo & Brown, 2003; Elliot et al., 2005; Petit et al., 2006; Larsen et al., 2007). However, TNOs with higher orbital inclinations exist as well. Since Brown (2001) it is known that the inclination distribution of TNOs has a second component with higher inclinations ( $i = 17^\circ \pm 3^\circ$ ).

Several objects with very high inclinations, including four retrograde ones with  $i > 90^\circ$ , were detected. Clearly, the fact that observations are done near the ecliptic plane decreases the probability to detect such extreme objects, because it is only possible twice per orbital

period, close to the nodes. Thus there is an obvious selection effect in favor of TNOs in low-inclination orbits that needs to be taken into account. Equally obvious is another selection effect, which is that objects are predominantly discovered at smaller heliocentric distances. This reduces the probability to discover TNOs with large semimajor axes and high eccentricities, because these are too faint all the time except for the short period of time when they are near perihelion.

## 3.2. Classification of TNOs

Many classifications of TNOs into “classical”, “resonant”, “excited”, “scattered”, “detached” etc. groups have been proposed, based on the orbital elements and taking into account dynamical arguments (e.g., Jewitt et al., 1998; Chiang & Brown, 1999; Luu & Jewitt, 2002; Delsanti & Jewitt, 2006; Jewitt et al., 2009, among others). Classifications by different authors are similar, but not identical. In this thesis we use the following working classification:

1. Resonant objects (RES): objects in a mean-motion commensurability with Neptune, where we only consider the three most prominent first-order resonances 4:3, 3:2 and 2:1. To identify the objects as resonant, we use the resonance “widths” from Murray & Dermott (2000). For example, the width of the 3:2-resonance at  $e = 0.1$  is  $\Delta a = 0.012$  AU. The width increases with increasing eccentricity and with decreasing distance to Neptune.
2. Classical Kuiper Belt (CKB) objects: objects with  $a < 50$  AU, which are neither resonant nor Neptune-crossers ( $q > a_{\text{Neptune}}$ ).
3. Scattered disk objects (SDO): objects with  $a > 50$  AU, as well as Neptune-crossers ( $a > a_{\text{Neptune}}$  and  $q < a_{\text{Neptune}}$ ).

Figure 3.1 depicts all known TNOs, using different symbols for each of the three groups. This classification is intentionally made simpler than many others in common use, in order to facilitate the analysis below. For instance, in our classification, the known detached objects (those with perihelia well outside Neptune’s orbit,  $q > 40$  AU) fall into the “scattered” category. By any account, the parameters of the entire EKB and its dust that we will derive will not depend on the way in which the TNOs are classified into various groups. On the other hand, this classification roughly reflects different formation history of different populations in the EKB, as well as different modes of their gravitational interaction with Neptune at present.

### 3.3. Debiasing Procedure

Because of the obvious selection effects of inclined and faint objects, statistical models were developed to estimate a true distribution of orbital elements and numbers of the TNOs. Brown (2001) calculated an inclination distribution. He assumed circular orbits and derived a relation between the inclination and the fraction of an object's orbit that it spends at low ecliptic latitudes. Donnison (2006) calculated the magnitude distribution for the classical, resonant, and scattered objects for absolute magnitudes  $H < 7$ , using maximum likelihood estimations, and showed that the samples were statistically different. Furthermore, Kavelaars et al. (2009) used CFEPS (Canada-France *Ecliptic* Plane Survey), which they describe in a great detail. They made several different statistical approaches to analyze the one-dimensional orbital element distribution  $(a, e, i)$  of different classes in the EKB<sup>17</sup>.

Here we propose another debiasing method<sup>18</sup> to estimate the “true” distribution of the TNOs, based on the observational surveys listed in Table 3.1. We start with calculating the probability to find an object with the given parameters  $\{a, e, i, \omega, \Omega, H\}$  for each given survey. To this end, we estimate the time fraction of the object's orbit that lies within the maximum ecliptic latitude  $\varepsilon$  covered by the survey, as well as the fraction of the orbit which is observable at the given limiting magnitude  $m_{50}$ , and find the intersection of the two orbital arcs. Once the probability to detect the object in each of the surveys has been calculated, we compute the probability that it would be detected at least in one of the surveys made so far. Finally, we augment the number of objects with that same orbital elements as the object considered to a 100% probability, e.g., an object with 20% probability is counted five times.

We now explain this procedure in more detail. The first effect is the *inclination bias*. Observing in the ecliptic plane lowers the detection probability of highly inclined objects, which leads to this bias. In calculating the orbital arc that lies in the observable latitudinal zone, we make the assumption that we observe from the Sun. The observable area on the sky is thus a belt  $|b| \leq \varepsilon$ , where  $b$  is the heliocentric ecliptic latitude. The orbit crosses the boundary of the observed belt,  $|b| = \varepsilon$ , at four points. At these intersection points, the

---

<sup>17</sup>They use a more detailed classification of objects, e.g., they divide the classical belt into the cold and hot subgroups.

<sup>18</sup>Note that there are several other debiasing attempts. Nevertheless, the advantage of the algorithm presented below is that we can debias *all* orbital elements and the size distribution simultaneously. Additionally, the results are optimized for implementation to our collisional code (see Chapters 4 & 5).

true anomaly  $\varphi$  takes the values

$$\varphi_j = \pm \arccos \left( \pm \sqrt{1 - \frac{\sin^2 \varepsilon}{\sin^2 i}} \right) - \omega. \quad (3.1)$$

Due to our approximation that we observe from the Sun, the longitude of the ascending node does not appear in this formula.

The second effect is the *distance bias* (or *eccentricity bias*). The maximum distance at which an object is detectable is given by (Irwin et al., 1995)

$$r_{\max} = 10^{0.1(m_{50}-H)}. \quad (3.2)$$

Then we combine both observability constraints, from inclination (Eq. 3.1) and eccentricity (Eq. 3.2), into one, to find the orbital arc (or arcs) that lie both in the observable latitudinal belt and the observable sphere. Typical geometries are sketched in Fig. 3.2, assuming that the pericenter is inside (I... IX) and outside (X... XVIII) the observing latitudinal belt. The intersection points of the orbit with the visibility sphere  $r = r_{\max}$  are denoted by  $E_k$ , those with the visibility circle  $|b| = \pm \varepsilon$  by  $I_k$  (indices  $k$  increase with increasing true anomaly). The point  $E_1$  can lie before  $I_1$ , between  $I_1$  and  $I_2$ , or between  $I_2$  and  $I_3$ , giving three possibilities. On the other hand, the point  $E_2$  can reside between  $I_2$  and  $I_3$ , between  $I_3$  and  $I_4$ , or after  $I_4$ . Furthermore, the pericenter can lie inside or outside the observing latitudinal belt. This yields  $2 \times 3 \times 3 = 18$  possibilities in total, denoted by I...XVIII. Additionally, there are special cases. One is  $i < \varepsilon$ , where the entire orbit is inside the observable belt, so that the points  $I_1 \dots I_4$  do not exist (exemplified by case XIX, where also the entire orbit is in the observable sphere and  $E_1, E_2$  do not exist). Others are where the entire orbit is inside or outside the observable sphere, so that the points  $E_1$  and  $E_2$  do not exist (exemplified by case XX, where the entire orbit is outside of the observable sphere and  $E_1, E_2$  do not exist, but the orbit is partly outside the observable belt).

As an example, we take ellipse number III. The object starts at the pericenter (where it is visible) and moves toward  $I_1$ . Between  $I_1$  and  $I_2$ , it is outside the observed latitudinal belt and is invisible. Although it has a sufficiently low ecliptic latitude up to  $I_3$ , it is only detectable up to  $E_1$ , because it gets too faint beyond that point. Between  $I_3$  and  $I_4$  the object is too far from the ecliptic, and it stays outside the limiting sphere until it reaches  $E_2$ . Starting from  $E_2$ , the object is visible again.

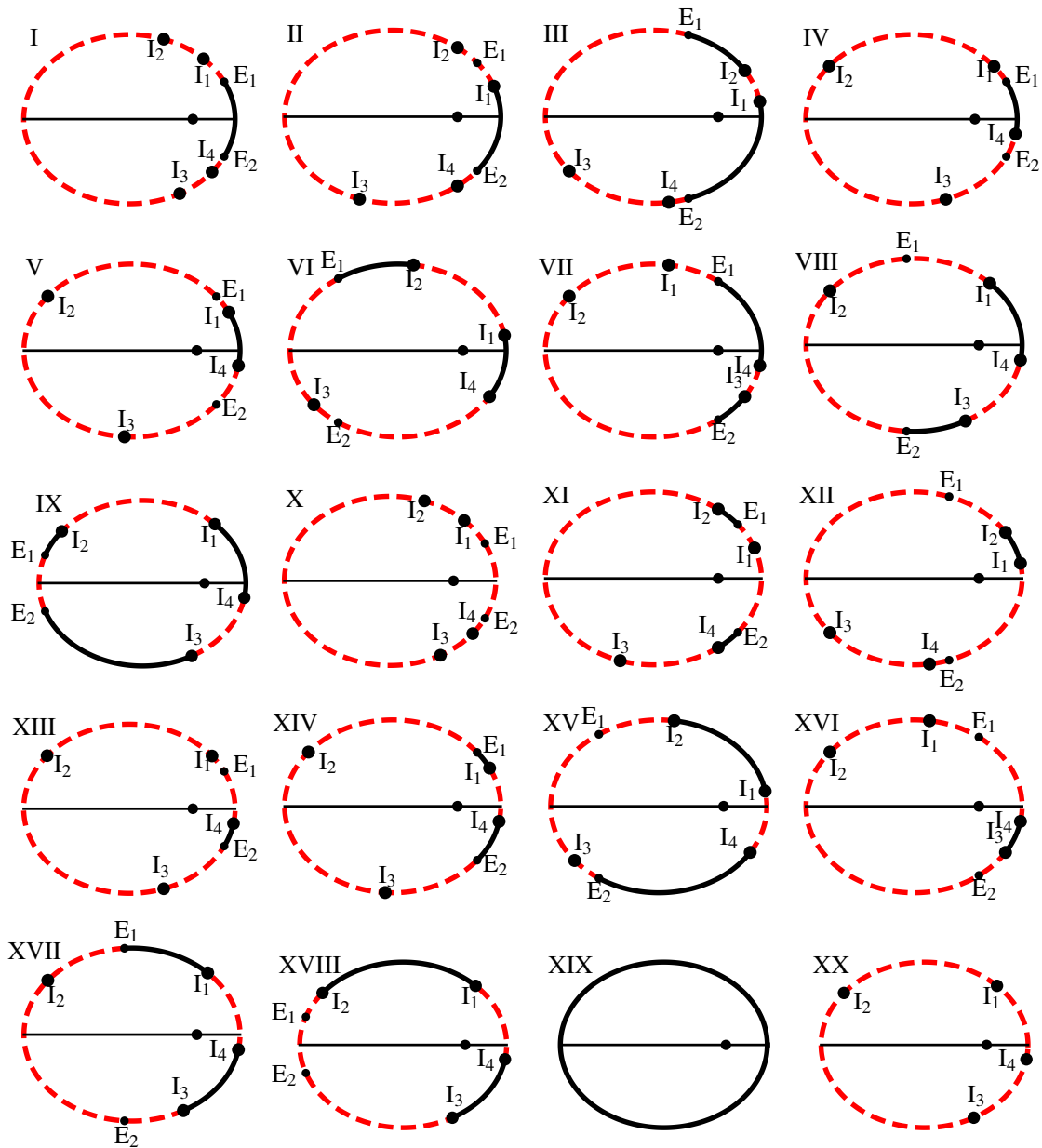


Figure 3.2.: Observable arc(s) of a TNO orbit that satisfy the distance and the inclination restrictions. Smaller points denoted with  $E_1$  and  $E_2$  are intersection points of the orbit with the sphere  $r = r_{\max}$ . Bigger points  $I_1 \dots I_4$  are intersection points of the orbit with the circles  $b = \pm \varepsilon$  on the sky. Solid and dashed arcs represent observable and non-observable parts of the orbit, respectively.

Having found the observable arcs, we compute the fraction  $f$  of the object's orbital period it spends in these arcs for a given survey. If the survey had a full ( $360^\circ$ ) coverage of the ecliptic longitudes, that fraction would directly give us the probability to detect the

object. However, the survey is confined to the longitude range with a certain width  $\alpha$ . This width is often given in the papers, and where it is not, we simply take  $\alpha = \sqrt{\Omega} = 2\varepsilon$ , where  $\Omega$  is the observed sky area. Thus the detection probability is  $f$  multiplied by  $\alpha/360^\circ$ . This estimation assumes that all the observations are done within a period of time that is much shorter than the orbital period of the TNO, so that its proper motion can be neglected. This is the case for all the surveys we consider. However, the same estimation assumes a uniform azimuthal distribution of the TNOs. For plutinos, for instance, this is no longer valid, as they concentrate preferably in two azimuthal zones ahead and behind Neptune’s location. Thus our algorithm may underestimate the detection probability of resonant objects, at least in surveys targeted at parts of the ecliptic where such objects are more numerous.

In this way, for each of the known TNOs, we can calculate the detection probability in any survey. We then calculate the probability  $P_i$  that an object  $i$  would be detected in any of the  $N_{\text{surveys}}$  surveys:

$$P_i = 1 - \prod_{k=1}^{N_{\text{surveys}}} (1 - P_{ik}), \quad (3.3)$$

where  $P_{ik}$  is the probability to detect an object  $i$  in a survey  $k$ . The advantage of equation 3.3 is that  $1 - P_{ik}$  gives the probability not to detect an object, “shallower” surveys make little contribution to the product and thus to the total detection probability of very faint objects. Therefore, it is deep surveys that dominate the result for faint objects.

Given the discovery probability  $P_i$  of a given object, we can augment the observed Kuiper belt to the “true” one by counting that object  $P_i^{-1}$  times. In other words, we debias the observed Kuiper belt by setting the number of TNOs with the same orbital elements as the known object to  $P_i^{-1}$ .

The number of surveys in Table 3.1 is  $N_{\text{surveys}} = 23$ . However, only nearly half of the 1260 TNOs contained in the MPC database were found in these campaigns. Another  $\approx 600$  objects were discovered in other observations, some serendipitously in surveys that did not aim to search for TNOs. The circumstances of those observations have not been published in all cases. What is more, even for the campaigns listed in Table 3.1, it is problematic to identify which particular set of  $\approx 600$  objects out of 1260 in total was found in those surveys. Indeed, the papers that give a specific, identifiable list of newly discovered objects (marked with an asterisk in Table 3.1) only cover  $\approx 400$  TNOs. We do not know under which circumstances the remaining two-thirds of the TNOs were detected. In other words, there is no guarantee that the parameters of those unknown surveys ( $m_{50}$ ,  $\varepsilon$  etc.) are similar to those listed in Table 3.1. Furthermore, some of the



surveys in our list may not have reported their discoveries to the MPC. As a result, it is difficult to judge how complete the MPC database is. We can even suspect that there have been surveys not listed in Table 3.1 that have discovered TNOs not listed in the MPC. Therefore, it does not appear possible to compile a complete version of Table 3.1 that would cover all known TNOs and all discovery observations (together with their  $\Omega$ ,  $m_{50}$ , and  $\varepsilon$ ). Nor is it possible to get a complete list of all known TNOs together with their orbital elements, along with information in which particular survey each of the known TNOs was discovered. To cope with these difficulties, we make two assumptions. First, we assume that the surveys listed in Table 3.1 are representative of all surveys that discovered TNOs. Second, we assume that, conversely, the TNOs listed in the MPC<sup>19</sup> are representative of all the objects discovered in surveys listed in Table 3.1. These two assumptions represent the main shortcoming of our debiasing approach.

To check them at least partly and proceed with the debiasing, we employed two different methods. In the first method, we have randomly chosen 600 TNOs out of the full list of known objects and assumed that it is these objects that were discovered in the campaigns listed in Table 3.1. We tried this several times for different sets of 600 TNOs and found that the results (e.g., the elemental distributions and the total mass of the “debiased EKB”) are in close agreement. In the second method, we have made an assumption that another set of 23 similar surveys with similar detection success rate would have likely led to a discovery of all known TNOs. So we simply counted each survey twice and replaced Eq. (3.3) by

$$P_i = 1 - \prod_{k=1}^{N_{\text{surveys}}} (1 - P_{ik})^2. \quad (3.4)$$

Again, the results turned out to be very close to those found with the first method.

Figure 3.3 illustrates the probabilities  $P_{ik}$  to observe known TNOs in a fiducial survey with  $m_{50} = 25$  mag, a latitudinal coverage of  $\varepsilon = 5^\circ$ , and a longitudinal coverage of  $360^\circ$ . Let us start with an artificial case where all objects are in circular orbits. If they were bright enough to be observed (or equivalently, in the limiting case  $m_{50} \rightarrow \infty$ ), they would all lie on the curve overplotted in Fig. 3.3. In particular, their detection probability would be 100% for  $i < \varepsilon$ , and it would be  $\varepsilon/90^\circ = 5.6\%$  for  $i = 90^\circ$ . If they are too faint for detection, their detection probability will be zero regardless of the inclination. The case of eccentric orbits is more complicated. Then, the vast majority of objects

---

<sup>19</sup>Note that the eccentricity of some objects is assumed to be zero in the MPC due to insufficient data. This applies to classical belt objects only which usually have a small eccentricity anyway. Therefore, this assumption plays a very minor role.

still are on the curve but, as seen in the figure, there are many that lie below. Either these are objects whose pericenter is outside of the latitudinal belt  $|b| < \varepsilon$  or these are objects that cannot be observed over the entire orbits, even when they have sufficiently low ecliptic latitude, because in some low-latitude parts of their orbits they are too faint to be visible. In fact, a mixture of both cases is typical. Finally, a few objects lie above the curve. These are rare cases of objects in highly-eccentric orbits, whose aphelia fall into the observable latitudinal belt, and whose apocentric distances are not too large. Such objects spend much of their orbital period near aphelia and are detectable there, which raises their detection probability.

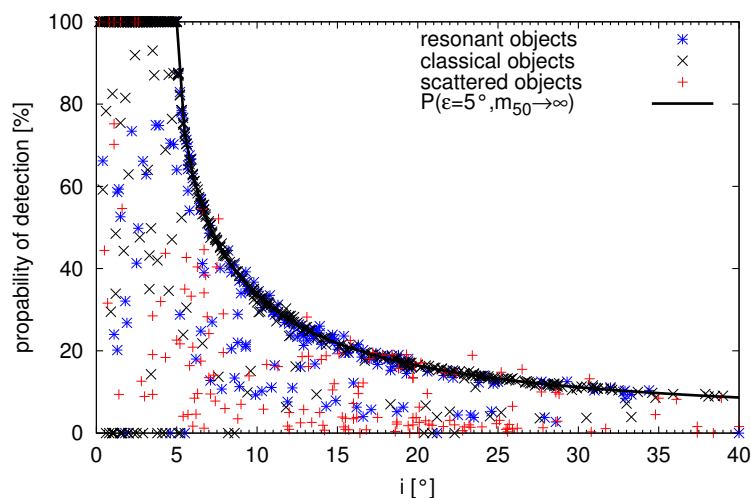


Figure 3.3.: The detection probability of all known TNOs (as function of their orbital inclinations) in a fiducial survey with a full coverage of a belt on the sky within  $\varepsilon = 5^\circ$  ecliptic latitude and the limiting magnitude of  $m_{50} = 25$  mag. The curve is the formal detection probability of objects in circular orbits in the  $m_{50} = \infty$  limit, but it approximates well the detection probability of many known TNOs in eccentric orbits in our fiducial survey. Objects which are below the curve are either those affected by the distance bias or have arguments of pericenters which are outside of our viewing field. Objects above the curve correspond to rare cases where the orbital eccentricity is high, aphelion lies in the observable belt, and the object is not too faint even near the aphelion. These are mostly scattered objects.

Although the average detection probability in Fig. 3.3 is quite high, this only holds for a complete coverage of the  $|b| < \varepsilon$  band on the sky. In reality, only a limited range of the ecliptic longitude is covered. The resulting detection probability  $P_i$  of all known TNOs in

all 23 surveys, calculated with Eq. (3.4) that takes into account actual latitudinal coverage of the observational campaigns, is plotted in Fig. 3.4. Typical values are within  $\sim 20\%$  for near-ecliptic orbits and drop to a few percent for inclinations above  $10^\circ$ .

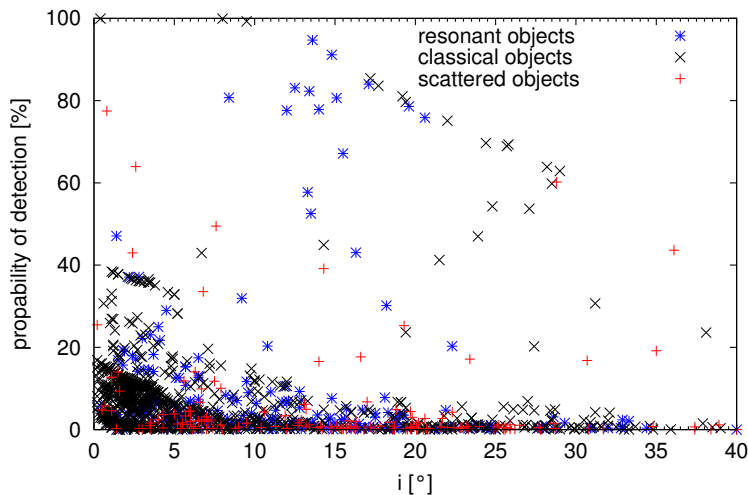


Figure 3.4.: The final detection probability of the known TNOs, calculated with Eq. (3.4). Included are all surveys from Table 3.1.

### 3.4. Orbital Element Distributions of the EKB Objects

Having applied the debiasing procedure, we compared and analyzed the distributions of orbital elements of the known and the “true” EKB — separately for each class.

Figures 3.5 and 3.6 show the distributions in terms of numbers (for  $s > 75$  km) and masses (for  $s < 400$  km) of objects per element’s bin before and after debiasing. The distribution in terms of numbers depicted in Fig. 3.5 emphasizes smaller, more numerous, TNOs. It is directly related to observational counts of TNOs and is also useful to alleviate comparison with similar work by the others. In contrast, the distribution of TNO’s mass in Fig. 3.6 is dominated by larger objects. It demonstrates more clearly where the wealth of the EKB *material* is located, which aids placing the EKB in context of extrasolar debris disks. Objects with  $s < 75$  km were excluded from Fig. 3.5, because detections of the smallest objects are the least complete, which would lead to a highly uncertain, distorted distribution. Conversely, we excluded the biggest objects with  $s > 400$  km from Fig 3.6 to avoid large bin-to-bin variations stemming from a few individual rogues. Failure to

do this would lead, for example, to a pronounced peak in the eccentricity distribution of resonant objects at  $e = 0.15 \dots 0.20$  produced by a single object, Pluto.

As seen in Figs. 3.5 and 3.6 for the classical Kuiper belt, debiasing increases the total number and mass of objects, but the position of the maximum remains at  $a \approx 44$  AU. The same holds for the semimajor axis distribution of resonant objects, whose peaks are preserved at known resonant locations. In contrast, for the scattered objects, here are indications that a substantial unbiased population with larger semimajor axes of  $80 \dots 120$  AU might exist. Some of them may be “detached” ( $q > a_{\text{Neptune}}$ ), while some others may not (since the eccentricities of these TNOs are also large, see middle panels in the bottom rows of Figs. 3.5 and 3.6). These conclusions should be taken with caution, because the statistics of scattered objects are scarce and their debiasing factors are the largest.

The eccentricity distribution in Figs. 3.5 and 3.6 shows moderate values ( $e < 0.2$ ) for the classical belt and reveals a broad maximum at  $e \approx 0.1 \dots 0.3$  for the resonant objects (Kavelaars et al., 2009 found a maximum at  $e = 0.2$ ). The maximum for the scattered objects appears to be located around  $e \approx 0.5 \dots 0.6$ .

As far as the inclination distribution (right panels in Figs. 3.5 and 3.6) is concerned, our analysis confirms the result by Brown (2001) who identified two distinct subpopulations in the classical Kuiper belt, a cold one with low inclinations and a hot one with high inclined orbits. The maxima of  $0^\circ \dots 5^\circ$  and  $20^\circ \dots 25^\circ$  that we found are consistent with his results of  $2.6_{-0.6}^{+0.2^\circ}$  and  $17^\circ \pm 3^\circ$ . Simulations of Kuchner et al. (2002) showed that long-term interaction with the four outer planets results in removing low-inclination objects, raising the mean value of the inclination. However, this does not explain the second maximum in the distribution.

The inclination distribution of the resonant objects reveals a broad maximum around  $\approx 15^\circ$ . For comparison, Brown (2001) found a maximum at  $10.2_{-1.8}^{+2.5^\circ}$ . A second maximum visible at  $i = 30^\circ \dots 35^\circ$  in the number distribution (Fig. 3.5) is due to small objects with a large debiasing factor, which are still big enough not to fall under the  $s < 75$  km criterion. That is why in Fig. 3.6 the same peak is barely seen.

A clear difference between the number and mass distributions can be seen in the bottom right panels of the two figures, too, which show the inclination distribution of the scattered objects. A large number of scattered TNOs can be found at  $25^\circ \dots 30^\circ$  (Fig. 3.5), whereas their mass peaks at  $15^\circ \dots 20^\circ$  (Fig. 3.6). Interestingly, a recent paper by Gulbis et al. (2010) yielded  $19.1_{-3.6}^{+3.9^\circ}$ , which is close to the maxima we find here.

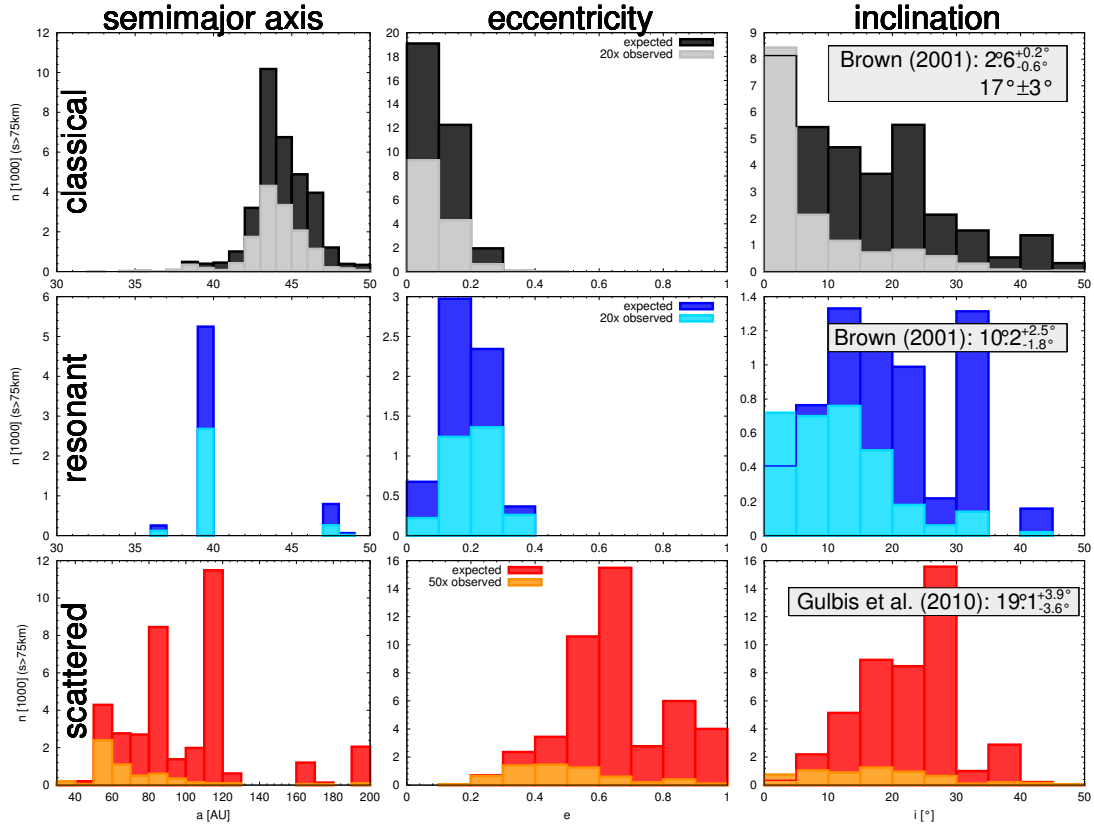


Figure 3.5.: Distribution of classical (top row), resonant (middle row), and scattered objects (bottom row), in terms of numbers of objects. Left column: semimajor axes, middle: eccentricities, right: inclinations. Dark and light bars in each panel represent the expected (debiased) and observed populations, respectively. The numbers of the observed TNOs are magnified by 20 (classical and resonant objects) and 50 (scattered objects) for better visibility. Numbers are given in 1000 for intervals with a width of  $\Delta a = 1$  AU (classical and resonant),  $\Delta a = 10$  AU (scattered objects),  $\Delta e = 0.1$  and  $\Delta i = 5^\circ$  for all populations.

### 3.5. Albedos and Sizes of the Kuiper Belt Objects

To estimate the TNO sizes, we employed the V-band formula from Kavelaars et al. (2009):

$$H = m_\odot + 42.38 - 2.5 \lg(4ps^2), \quad (3.5)$$

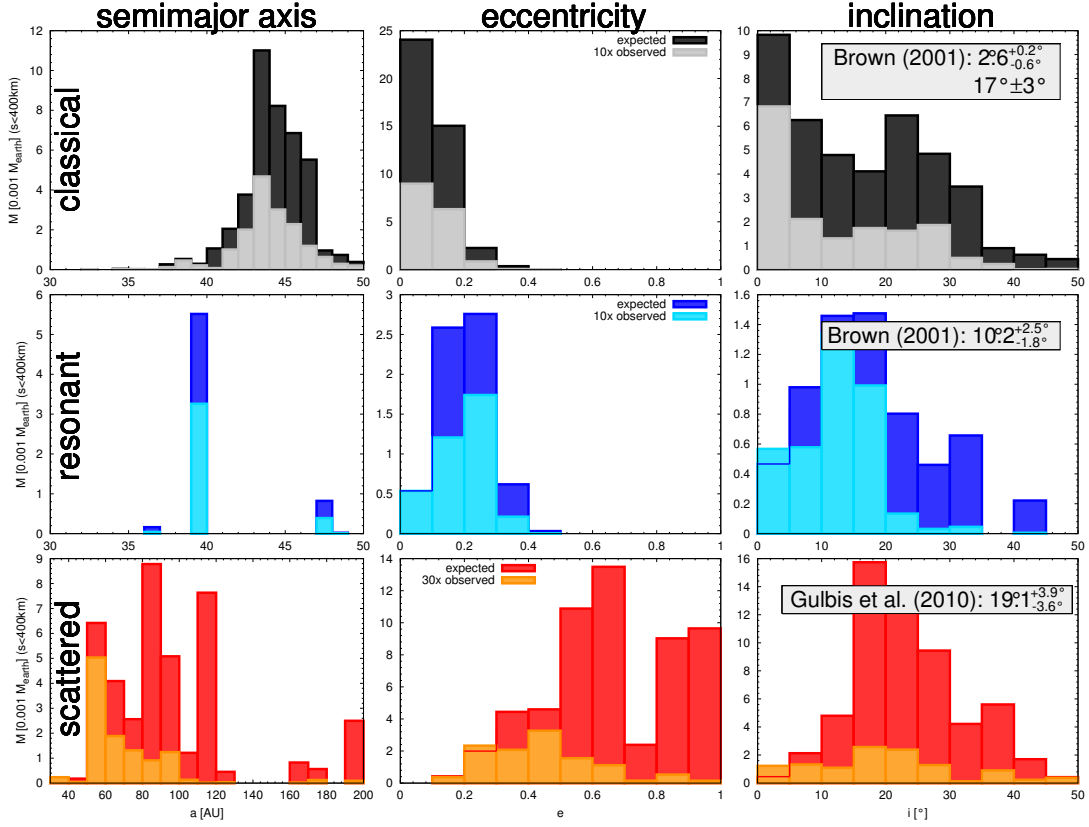


Figure 3.6.: Same as Fig. 3.5, but in terms of mass contained in TNOs.

where  $m_{\odot} = -26.74$  mag is the apparent V-magnitude of the Sun,  $p$  the albedo and  $s$  the radius of an object in kilometers. Solving for radius, we find

$$s = 671.5 \times \frac{10^{-0.2H}}{\sqrt{p}} \text{ km.} \quad (3.6)$$

With this equation and albedo measurements from Noll et al. (2004), Stansberry et al. (2008), Brucker et al. (2009), Santos-Sanz et al. (2012), Mommert et al. (2012), Vilenius et al. (2012), and Pál et al. (2012), we calculated the radius of objects with known albedo (Fig. 3.7).

Albedos inferred for a handful of big objects with  $H \leq 3$  turned out to be high, which is indicative of a strongly reflecting surface material. For instance, the surface of Haumea was found to be covered with  $> 92\%$  pure water ice (Pinilla-Alonso et al., 2009). Dumas et al. (2007) reported for Eris 50% methane ice on its surface along with nitrogen and water ices, and ice tholin. Smaller objects are coated with darker carbonaceous layers, so

their albedo is lower. Note that objects between  $6 < H < 7$  have a very strong scatter, the reason for that being unknown. Albedos of the smallest TNOs with  $7 < H < 9$  are typically close to  $\approx 0.05$ , and there have been no measurements beyond  $H = 9$ . However, since the EKB is known to act as a reservoir of short-period comets, we can use the measurements of cometary nuclei with sizes of  $\sim 1\text{--}10$  km as a proxy for the reflectance properties of the smallest TNOs. (The obvious caveat is that comets may have altered their original surface properties as a result of their long residence in the inner Solar System.) The typical albedo values of the nuclei range from 0.02 to 0.06 (Lamy et al., 2004).

On these grounds, to eliminate the dependence on albedo (which is not known for most of the Kuiper belt objects) from Eq. (3.6), we have fitted the sizes of the TNOs with known albedo by an exponential function at  $H < 6$  and assumed  $p = 0.05$  for all TNOs with  $H \geq 6$ . This yielded a formula where  $s$  is only a function of  $H$ :

$$s = 882 \times 10^{-0.117H} \text{ km} \quad (H < 6) \quad (3.7)$$

and

$$s = 3000 \times 10^{-0.2H} \text{ km} \quad (H \geq 6). \quad (3.8)$$

The smallest object found so far is a scattered object with  $H = 15$  mag which corresponds to a size of only  $s = 3$  km. The smallest resonant object has a radius of  $s = 9.9$  km ( $H = 12.4$  mag) and the smallest classical one has  $s = 12.5$  km ( $H = 11.9$  mag).

### 3.6. Mass of the Kuiper Belt

To translate the TNO sizes into masses requires an assumption regarding their (composition and) bulk density. In this section the commonly used value of  $\varrho = 1 \text{ g cm}^{-3}$  is taken. All masses given here can simply be translated for different bulk densities by

$$M(\varrho) = \frac{\varrho}{1 \text{ g cm}^{-3}} M(\varrho = 1 \text{ g cm}^{-3}). \quad (3.9)$$

The resulting mass and number of objects in resonant, classical, and scattered populations and in the entire Kuiper belt are listed in Table 3.2. Note that the numbers are given there for objects  $s > 75$  km. The deduced “true” masses are several times higher than in Fuentes & Holman (2008) who inferred  $M_{\text{CKB}} = (0.008 \pm 0.001)M_{\oplus}$ ,  $M_{\text{SDO}} = 0.010_{-0.003}^{+0.021}M_{\oplus}$ , with a total of  $M_{\text{tot}} = 0.020_{-0.003}^{+0.004}M_{\oplus}$ . However, they considered the mass within  $\pm 3^\circ$  around

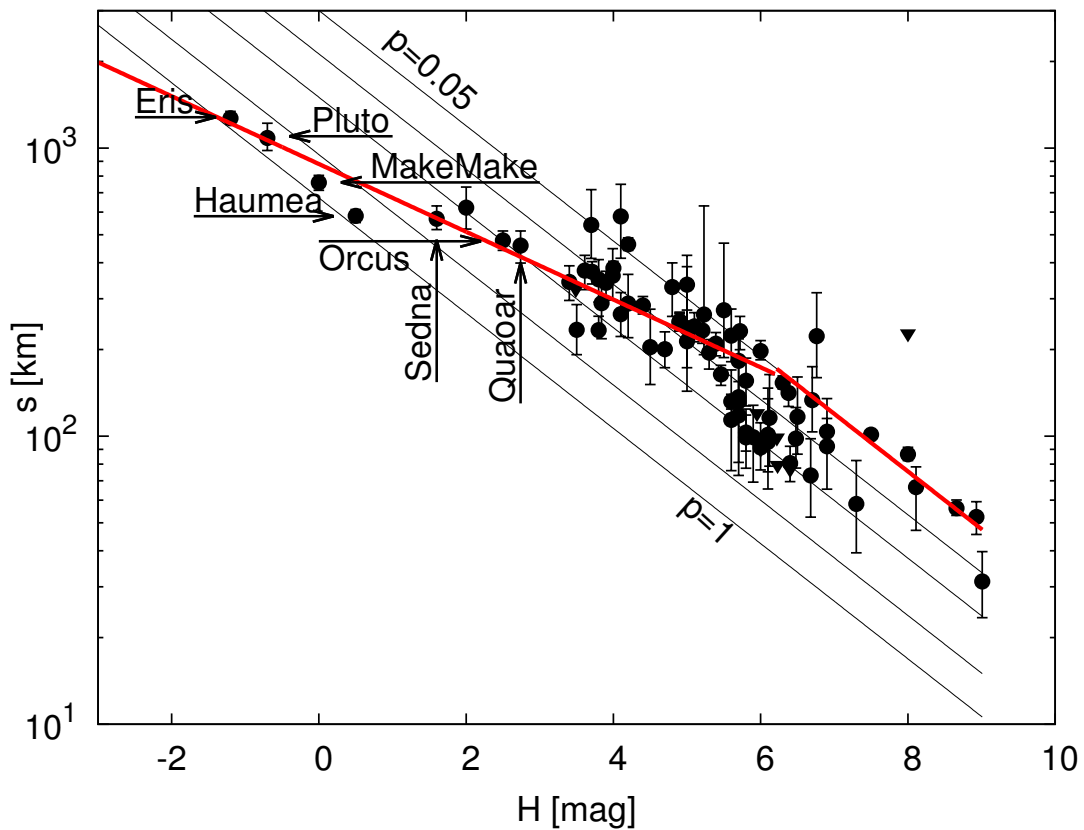


Figure 3.7.: Absolute magnitude – radius relation for objects with known albedo. The biggest objects are labeled with their names. The thick solid line is a fit to this relation, Eqs. (3.7)–(3.8). Thin lines correspond to equal albedos of  $p = 0.05; 0.10; 0.20; 0.50; 1.00$ .

the ecliptic. Since we investigated the full range of ecliptic latitudes, we deem the results consistent with each other.

One issue about the deduced mass of the entire EKB and its populations is the influence of the uncertainties of the orbital elements inferred from the observations. In many cases, the elements are known only roughly. How could a change in the orbital elements of an object affect the debiasing procedure and the final estimates of the parameters of the “true” EKB? Obviously, if a true value of *one* of the three elements of a TNO ( $a$ ,  $i$ , or the absolute magnitude  $H$ ) is larger than the one given in the database, the detection probability will be overestimated and the estimated number of similar objects in the “true” EKB underestimated. The eccentricity plays a special role in this case. Increasing it would



Table 3.2.: Masses and numbers of objects in the Kuiper belt. CKB is the classical Kuiper belt, RES are the resonant objects, and SDO denotes the scattered disk objects.

	before debiasing	after debiasing
$M_{\text{CKB}}$ [ $0.001 M_{\oplus}$ ]	2.7	43
$M_{\text{RES}}$ [ $0.001 M_{\oplus}$ ]	1.2	8
$M_{\text{CKB+RES}}$ [ $0.001 M_{\oplus}$ ]	3.9	51
$M_{\text{SDO}}$ [ $0.001 M_{\oplus}$ ]	1.9	63
$M_{\text{total}}$ [ $0.001 M_{\oplus}$ ]	5.8	114
$N_{\text{CKB}} (s > 75 \text{ km})$	715	33400
$N_{\text{RES}} (s > 75 \text{ km})$	154	6360
$N_{\text{CKB+RES}} (s > 75 \text{ km})$	869	39860
$N_{\text{SDO}} (s > 75 \text{ km})$	122	45200
$N_{\text{total}} (s > 75 \text{ km})$	991	84960

not automatically lead to a lower detection probability, the pericenter distance decreases while the apocenter increases, so that the total detection probability depends also on  $a$ . However, a combined variation of two or more elements may alter the results in either direction. As an example, let us consider a scattered object with  $a = 1057$  AU and  $e = 0.977$ , which has a pericenter distance of  $q = 24.3$  AU. Decreasing, for instance, both  $a$  and  $e$  by 5% would lead to a pericenter at  $q = 72$  AU, which would result in a significantly lower detection probability and therefore in a higher contribution of that object to the estimated total mass. In contrast, we may consider a classical object with  $a = 40$  AU and  $e = 0.2$ , which cannot be observed near the apocenter. Again, decreasing both values by 5% would now reduce the aphelion distance to detectable values, so that the detection probability would increase.

From published observational results, we assume 5–10% as a typical error for the orbital elements. To quantify possible effects, we used the following Monte-Carlo procedure. We assumed that the orbital elements and the absolute magnitude  $\{a, e, i, H\}$  are known with a standard deviation  $\sigma$  (for simplicity, the same for all four elements). Then, we randomly generated  $\{a, e, i, H\}$ -sets for each of the known TNOs assuming that each element of each object is normally distributed around its cataloged value. For this hypothetical EKB, the debiasing procedure was applied and the expected masses of objects in the “true” Kuiper belt were evaluated. This procedure was repeated 10,000 times (for 10,000 realizations of the observed Kuiper belt, that is to say). The results for several  $\sigma$  values between 5% and 15% are listed in Table 3.3. Since this variation of the elements lead to numerous huge outliers, only the mean value and the median of the results is shown and the standard deviations are not reported.

Interestingly, the net effect for the CKB and RES of the increasing  $\sigma$  is that the mean TNO detection probabilities decrease, which leads to somewhat higher estimates for the mass of the EKB populations and the whole Kuiper belt up to a factor of 4, while the median nearly stays constant. For the subpopulation of the SDOs any conclusion about the mass is brave, since an uncertainty of 20% would alter the mean total mass of the SDOs by a factor of 70. This either shows that the given values for the elements are very accurate or if they are not, there is a lot of mass hidden in the population of the scattered objects.

Table 3.3.: Masses of objects in the Kuiper belt, as a function of the assumed standard deviation  $\sigma$ , with which orbital elements of TNOs were deduced from observations. Abbreviations and units are as in Table 3.2.

$\sigma$ [%]	$M_{\text{CKB}}$		$M_{\text{RES}}$		$M_{\text{CKB+RES}}$		$M_{\text{SDO}}$	
	mean	median	mean	median	mean	median	mean	median
5	45.4	43.3	8.4	7.6	54.3	51.2	2250	64.4
10	61.4	43.1	9.7	7.6	73.9	51.3	3120	86.1
15	107.4	42.5	16.9	7.5	121.8	51.7	3589	149.4
20	162.9	42.5	28.5	7.5	203.0	51.2	4235	206.7

### 3.7. Size Distribution of the Kuiper Belt Objects

We now come to the size distribution of EKBOs. The exponents  $q$  of the differential size distribution  $N(s) ds \propto s^{-q} ds$  after debiasing were derived with the size-magnitude relation (3.7)–(3.8). In doing so, we have chosen the size range  $50 \text{ km} < s < 170 \text{ km}$  ( $8.9 > H > 6$ ), and we determined the size distribution index separately for different populations of TNOs and their combinations. For the CKB, the result is  $q = 4.3 \pm 0.2$ . The resonant objects reveal a steeper slope of  $5.1 \pm 0.1$ , with plutinos (in 3:2 resonance with Neptune) having  $5.3 \pm 0.1$  and twotinos (2:1 resonance) having  $4.0 \pm 0.1$ . This results in  $4.4 \pm 0.2$  for classical and all resonant objects together. In contrast, the scattered objects have  $2.8 \pm 0.1$ . Altogether, we find  $3.6 \pm 0.1$  for the entire EKB (classical, resonant, and scattered TNOs).

Our results are largely consistent with previous determinations (Table 3.4). For the CKB, for instance, the range between  $3.6 \pm 0.1$  (Chiang & Brown, 1999) and  $4.8_{-0.6}^{+0.5}$  (Gladman et al., 1998) was reported. In this comparison, one has to take into account that different authors dealt with somewhat different size intervals. Chiang & Brown (1999) considered objects between 50...500 km, Gladman et al. (2001) and Trujillo et al. (2001a)

between 50... 1000 km, and Donnison (2006) between 120... 540 km ( $7 > H > 2$ ). For the SDOs, our results are also consistent within the error bars with Donnison (2006). However, for the resonant objects our result departs from his appreciably.

Table 3.4.: Size distribution index of the Kuiper belt populations.

CKB	RES	SDO	reference
$4.3 \pm 0.2$	$5.1 \pm 0.1$	$2.8 \pm 0.1$	this work
$4.8^{+0.5}_{-0.6}$			Gladman et al. (1998)
$4.0 \pm 0.5$			Jewitt et al. (1998)
$3.7 \pm 0.2$			Luu & Jewitt (1998)
$3.6 \pm 0.1$			Chiang & Brown (1999)
$4.4 \pm 0.3$			Gladman et al. (2001)
$4.0^{+0.6}_{-0.5}$			Trujillo et al. (2001a)
$4.05 \pm 0.2$			Bernstein et al. (2004)
$3.97 \pm 0.15$	$3.30 \pm 0.37$	$3.02 \pm 0.32$	Donnison (2006)

Figure 3.8 shows cumulative numbers of the expected Kuiper belt objects larger than a given size. In agreement with Donnison (2006), the profile flattens for objects  $s \lesssim 60$  km ( $H < 7$ ). Without further investigation (see Chapter 5) the break in the size distribution at radii of several tens of kilometers reported by some authors, e.g., at  $s \approx 30$  km by Bernstein et al. (2004) and Fraser (2009) can neither be clearly identified nor ruled out with our debiasing algorithm at this point.

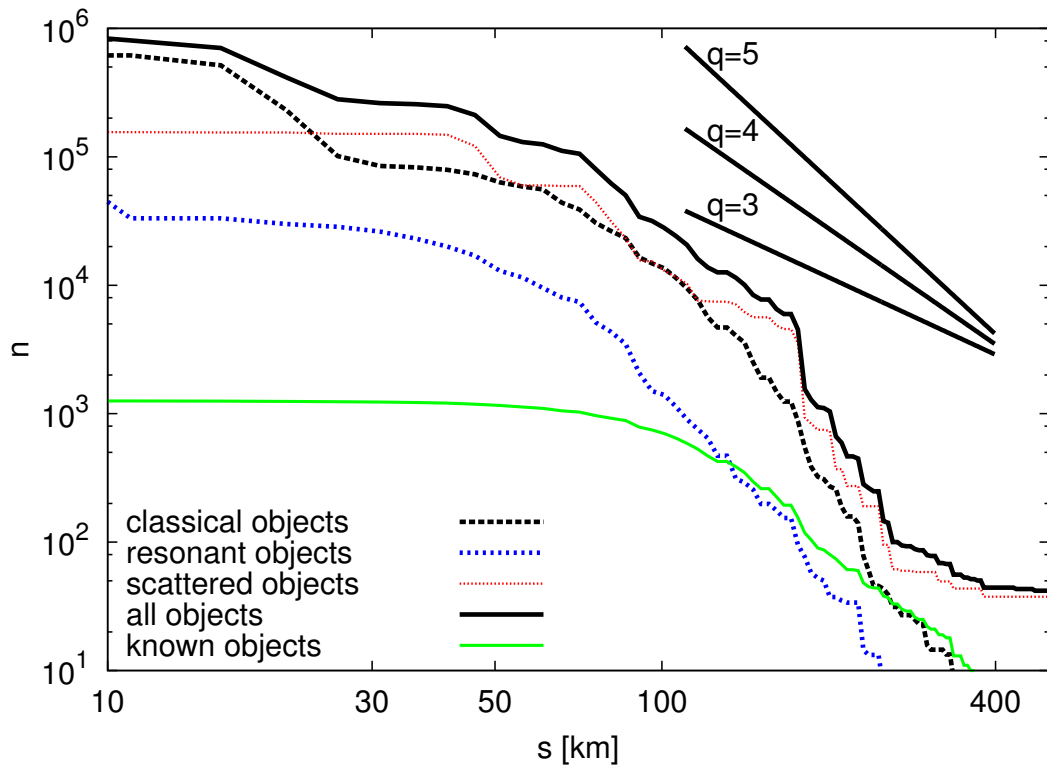


Figure 3.8.: Cumulative numbers of the expected and known Kuiper belt objects with a  $\Delta s = 5$  km resolution. For an easier orientation, straight lines show the slopes that would correspond to the differential size distribution indices of  $q = 3, 4,$  and  $5$ .

# 4. Model of the EKB Debris Disk in Collisional Equilibrium

“I have looked further into space than any human being did before me.”

---

Sir William Herschel (1738-1822)

*This Chapter is based on Vitense et al. (2010). The analyses and results presented here were obtained in conjunction with Alexander Krivov and Torsten Löhne and are used here with their permission.*

In the case of Vega’s debris disk, whose mass is estimated to be  $\sim 10M_{\oplus}$  for objects  $s < 100$  km (Müller et al., 2010) collisions are dominant over all drag forces and therefore the disk is collision-dominated. That means that drag forces do not modify the size and radial distribution significantly. A disk can usually be considered to be collision-dominated if the optical depth  $\tau \gtrsim v_K/c$  (Kuchner & Stark, 2010). Reidemeister et al. (2011) showed for the massive disk of  $\varepsilon$  Eridani, however, that drag forces, in form of the stellar wind drag can make even a massive disk transport-dominated.

This difference is a combination of circumstances. First, the spectral type of the host star is important.  $\varepsilon$  Eridani, for example, is a K2 main sequence star with a high stellar mass loss rate and therefore high efficiency of the stellar wind drag. In addition, the mass of the disk is an important factor. For  $\varepsilon$  Eridani the total disk mass is lower than for Vega which makes the collisional timescales longer and therefore drag more effective.

In this Chapter the influence of our debiasing algorithm and the Poynting-Robertson drag on the radial and size distribution is analysed and explained and a first, simplified model of the EKB debris disk is developed.

At this point we make the following definitions. The *known EKB* consists of all objects found in the MPC (and produced dust with these objects), i.e. before applying our debiasing algorithm. Hence, the *expected EKB* defines the EKB (and its dust) after applying our algorithm.

## 4.1. Setup of the Collisional Simulations

To obtain the dust distributions in the present-day EKB, which is the goal of this thesis, we now move from the observable “macroscopic” objects in the EKB to the expected debris dust in the transneptunian region. Therefore, we used the collisional code *ACE* (Analysis of Collisional Evolution; Krivov et al., 2000, 2005, 2006, 2008; Löhne et al., 2008; Müller et al., 2010). The code was developed by Alexander Krivov, Miodrag Sremčević and Torsten Löhne. The author of this thesis made some minor contribution. It simulates the evolution of orbiting and colliding solids, solving the Boltzmann-Smoluchowski kinetic equation (Eq. 2.39) using a mesh of sizes  $s$ , pericentric distances  $q$ , and eccentricities  $e$  of objects as phase space variables (cf. Sec. 2.4). It includes the effects of stellar gravity, direct radiation pressure, Poynting-Robertson force, stellar wind, and several collisional outcomes (sticking, rebounding, cratering, and disruption), and collisional damping. For the critical specific impact energy Eq. 2.18 is used with the constants given in Sec. 2.3. Gravitational effects of planets in the system are not simulated with *ACE* directly. The code outputs, among other quantities, the size and radial distribution of disk solids over a broad size range from sub-micrometers to hundreds of kilometers at different time steps, and the code is fast enough to evolve the distribution over gigayears.

In the *ACE* simulations for this Chapter, we used the following size–pericentric distance–eccentricity mesh. The minimum grain radius was set to  $0.1 \mu\text{m}$  and the variable mass ratio in the adjacent bins between 4 (for largest TNOs) and 2.1 (for dust sizes). The pericenter distance grid covered 41 logarithmically-spaced values from 4 AU to 200 AU. The eccentricity grid contained 50 linearly-spaced values between  $-5.0$  and  $5.0$  (eccentricities are negative in the case of smallest grains with  $\beta > 1$ , whose orbits are anomalous hyperbolas, open outward from the star, see Sec. 2.2.3). The distance grid used by *ACE* to output distance-dependent quantities such as the size distribution was 100 values between 4 AU and 400 AU. The semi-opening angle was set to  $i \approx 8^\circ$ .

In many previous studies, the initial radial and size distributions of dust parent bodies — planetesimals — were taken in the form of power laws, with normalization factors and indices being parameters of the simulations. Here, we use a different approach. To take advantage of our knowledge of the (largest) parent bodies, TNOs, we directly filled the  $(m, q, e)$ -bins at the beginning of each simulation with the objects of the “true” Kuiper belt. For comparison, we also made a run, where we populated the bins with known TNOs only (without debiasing).

As already described, our “true” distribution hardly contains any objects with radii smaller than  $\sim 10$  km, because no or very few EKBOs of that sizes have been discovered. Given the lack of information on these objects, we chose to extrapolate the size distribution to smaller objects with a power law  $dN \propto s^{-q} ds$  with the unknown exponent  $q$ . The extrapolation was done the following way: For every object that resides in a bin  $\{s_i, q_j, e_k\}$ , the bins  $\{s_l, q_j, e_k\}$  are populated with  $(s_l/s_i)^{1-q}$  ( $l < i$ ) objects (assuming logarithmic size bins). That means that we simply assumed that these objects inherit the pericentric distance and the eccentricity from their parent bodies.

As a first approximation, we extrapolated the contents of the filled bins towards smaller sizes with a slope of  $q = 3.03$  for objects between  $100 \text{ m} < s < 75 \text{ km}$  (in the gravity regime) and  $q = 3.66$  for objects smaller than  $100 \text{ m}$  (in the strength regime), following O’Brien & Greenberg (2003). Note that the adopted slope in the gravity regime is roughly consistent with Fig. 3.8. The break at radii of several tens of kilometers reported by Bernstein et al. (2004) and Fraser (2009) was not included.

In the course of the collisional evolution, this artificial distribution corrects itself until it comes to a collisional quasi-steady state. The latter is assumed to have been reached, when the size distribution no longer changes its shape and just gradually moves down as a whole as a result of collisional depletion of parent bodies (Löhne et al., 2008). We find that after  $\leq 100$  Myr a collisional quasi-steady state sets in for all solids in the strength regime (i.e. smaller than  $\sim 100$  m).

Finally, we have to adopt the material properties, which necessitate assumptions about the chemical composition. The surface composition of a number of bright EKB objects has been measured (Barucci et al., 2008, see also discussion in Sec. 3.5). For the sake of simplicity, for the collisional simulation in this Chapter we choose an ideal material with  $\rho = 1 \text{ g cm}^{-3}$  and geometric optics, leading to the radiation pressure efficiency  $Q_{\text{pr}} = 1$ .

## 4.2. Results of the Collisional Simulations

**Size Distribution of Dust.** Figure 4.1 depicts the simulated size distribution of the EKB dust with all objects being in collisional equilibrium. We present three cases: for the debiased EKB without (top panel) and with P-R included (middle), as well as for the known EKB objects with P-R effect, for comparison (bottom). To explain the gross features of the size distributions shown in Fig. 4.1, the reader shall be reminded to the ratio of radiation pressure to gravity,  $\beta$  (see Sec. 2.2.3). If a small dust grain is released after a collision from a nearly circular orbit, its eccentricity is  $e \approx \beta(1 - \beta)^{-1} \propto s^{-1}$ . This implies

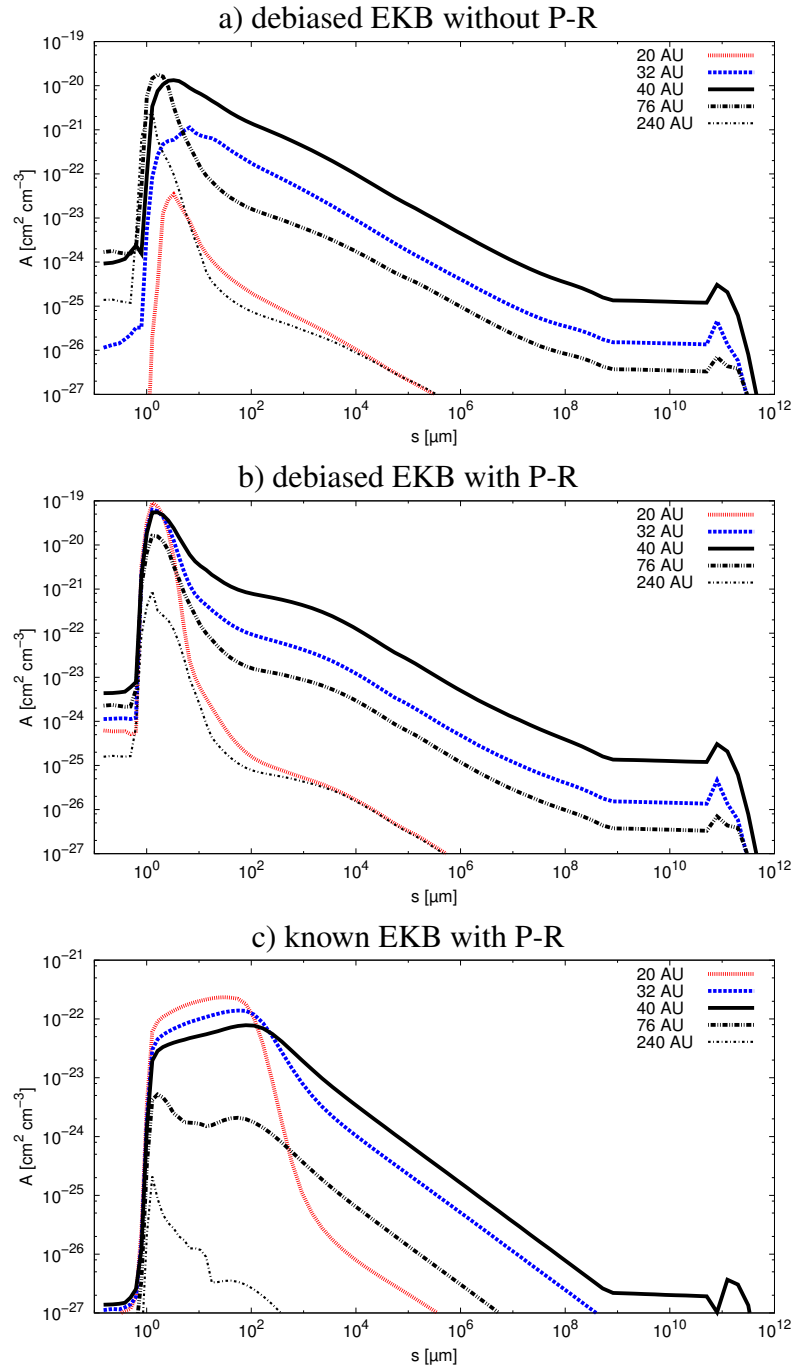


Figure 4.1.: Size distribution of the Kuiper belt dust at different distances. The vertical axis gives the cross-section density per size decade.

higher eccentricities for smaller grain sizes. The orbits of sufficiently small grains with  $\beta$  exceeding  $\sim 0.5$  are unbound. Accordingly, the grain radius that corresponds to  $\beta = 0.5$  is commonly referred to as blowout limit (see introduction of the  $\beta$ -ratio in Sec. 2.2.3). The



blowout size for the assumed material in the Solar System is  $s_{\text{blow}} \approx 1.2 \mu\text{m}$ . Typically, the amount of blowout grains instantaneously present in the steady-state system is much less than the amount of slightly larger grains in loosely bound orbits around the star. This is because the dust production of the grains of adjacent sizes is comparable, but the lifetime of bound grains (due to collisions) is much longer than the lifetime of blowout grains (disk-crossing timescale). This explains a drop in the size distribution around the blowout size which is seen in all three panels of Fig. 4.1.

Another generic feature of the size distribution is that it becomes narrower at larger distances from the Sun. Were the parent bodies all confined to a narrow radial belt, the distribution far outside would appear as a narrow peak composed only of small, high- $\beta$ , barely bound grains sent by radiation pressure into eccentric orbits with large apocentric distances. However, in the case of the EKB this effect is somewhat washed out, since the spatial distribution of parent bodies themselves (mostly, of scattered objects) is extended radially, as discussed below. As a result, the size distribution even at relatively large distances (e.g. 76 AU) is a superposition of such a narrow distribution and a background broad distribution of particles produced at those distances directly. Only at largest distances, at which hardly any parent bodies are present (see 240 AU curve), the size distribution transforms to a predicted narrow peak adjacent to the blowout size.

A direct comparison of our two simulations for the debiased EKB, without and with P-R effect, reveals some differences. One obvious — and expected — difference is the one between the 24 AU curves. At this distance (and all the others inside the main belt) parent bodies are nearly absent; there are only some scattered TNOs, see Fig. 3.1. Accordingly, without P-R nearly no dust is present there. However, a substantial amount of small particles is present there in the P-R case, because these are transported there by the P-R drag.

Outside  $\sim 30$  AU, the size distributions without and with P-R show more similarities than dissimilarities. In particular, the maximum of the cross section at  $s = 2 \mu\text{m}$  is nearly the same. At sizes  $s \geq 1$  mm, the curves roughly follow a classical Dohnanyi's law (cross section per size decade  $\propto s^{-0.5}$ ). The main difference is a dip of the size distribution in the region of the classical EKB that occurs at sizes of  $s = 100 \mu\text{m}$  in the P-R case, which is easy to explain. The  $100 \mu\text{m}$  grains in the classical EKB region stay in nearly-circular orbits, because their  $\beta$  ratio is small and radiation pressure-induced eccentricities are low. These grains are mainly destroyed in collisions with most abundant smaller grains, several  $\mu\text{m}$  in size. In the non-P-R case, the latter grains have their pericenters within the classical belt. Thus the collisions are “grazing”, the collisional velocities relatively low, and the

collisional destruction of  $100\ \mu\text{m}$  grains relatively inefficient. When the P-R effect is switched on, this changes. The P-R transport lowers the pericenters of smaller projectiles, and in the classical belt, they collide with  $100\ \mu\text{m}$  grains at higher speeds, which enhances their destruction and produces the dip. Note that this effect is absent farther out from the Sun. At a distance of 76 AU, for example, the collisions between smaller grains and  $100\ \mu\text{m}$  particles always occur far from the pericenter. Thus the P-R effect has little influence on the collisional velocities, and the size distribution in the non-P-R and P-R cases is similar.

However, the dust distributions computed with P-R effect, but for debiased EKB and known EKB, which are shown in middle and bottom panels of Fig. 4.1, exhibit a striking difference. The P-R effect has only a moderate influence on dust produced by the debiased EKB, but a strong one on dust generated solely by known TNOs. This needs to be explained. The debiasing and extrapolation procedure makes the EKB more densely populated, and the resulting increase in the dustiness shortens collision timescales to make them comparable with the P-R transport timescales. The resulting optical depth of the dust disk is such that it lies roughly between the collision-dominated and transport-dominated regimes. Without debiasing the parent body population, the dustiness of the disk is by two orders of magnitude lower, and so is the optical depth of the dust disk. At that optical depth level, the EKB dust disk would be transport-dominated below  $s \leq 100\ \mu\text{m}$  (but still collision-dominated at larger sizes). This is illustrated by the lowest panel in Fig. 4.1 that presents the size distribution of dust that would be produced by known TNOs. It is seen that the size distribution in such a transport-dominated disk differs from that in a collision-dominated one qualitatively. From  $s \sim 100\ \mu\text{m}$  down to blowout limit, the size distribution flattens and turns over. This is because the smaller the grains, the faster their inward P-R drift. This transport removes small grains from the collisionally active region and thus they are present in smaller amounts. As a result, the maximum of the cross-section density shifts towards  $s \sim 100\ \mu\text{m}$  particles.

**Radial Distribution of Dust.** Figure 4.2 presents the radial distribution of dust parent bodies and their dust, the latter simulated without and with P-R transport.

We start with the radial distribution of parent bodies, TNOs themselves, shown in Fig. 4.2a. In contrast to Fig. 3.6, we plot here the total cross section of the TNOs instead of the mass they carry, because it is the cross section that characterizes the efficiency of TNOs as dust producers. Besides, we use the distance from the Sun instead of the semimajor axis as an argument. Specifically, we plot the cross section in the 80 km-sized

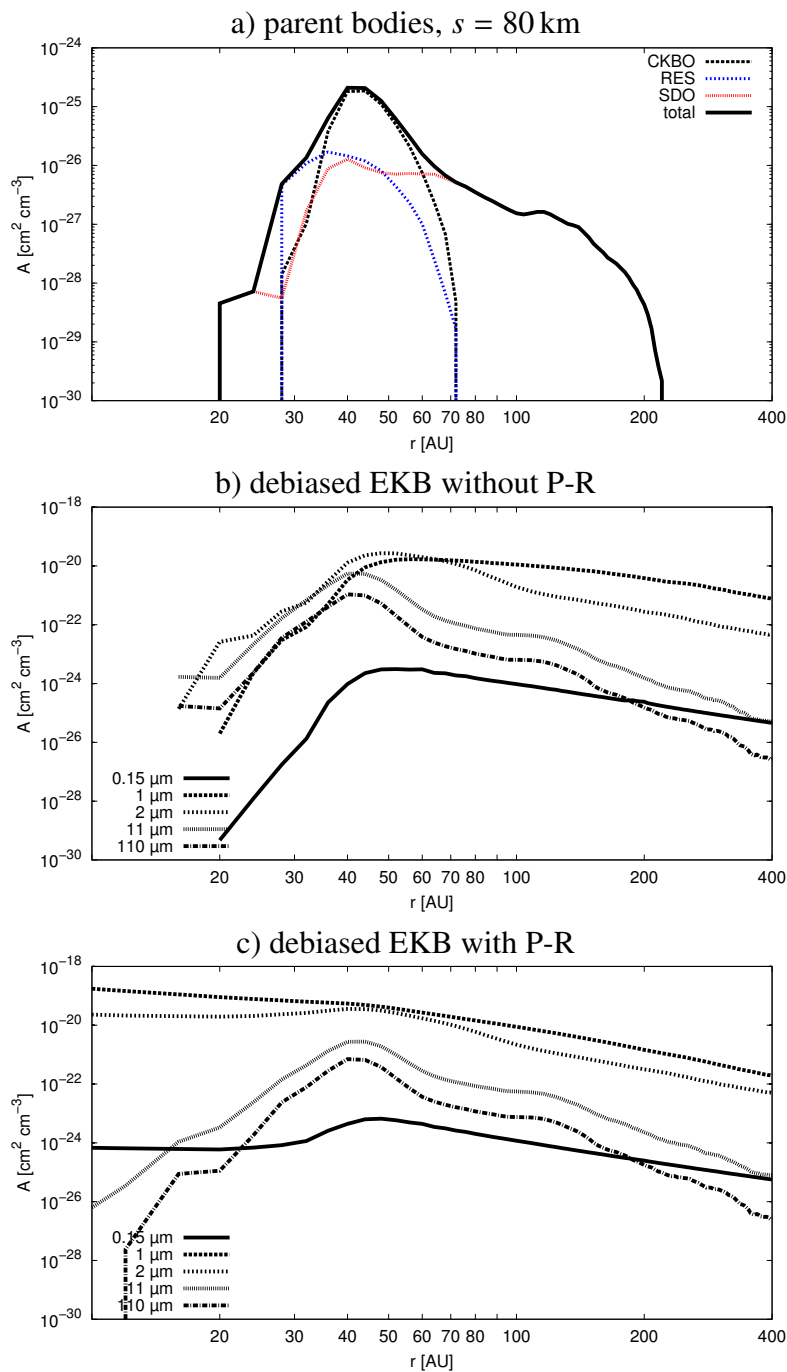


Figure 4.2.: Radial distribution of parent bodies ((a), from 64 km to 100 km in radius) and different-sized dust grains without (b) and with P-R drag (c). The vertical axis is the cross-section density per size decade.

TNOs, but the radial profile for larger objects look similar. As expected, the distribution peaks in the region of the main belt (40–50 AU), where about 90% of the cross section

comes from the classical EKB objects. Outside  $\sim 60$  AU, the cross section is solely due to scattered objects. The distribution of the latter is quite extended radially, it is nearly flat over a wide distance range from  $\approx 35$  AU to more than 100 AU.

We now move to a discussion of the radial distribution of dust. As noted above, smaller grains with higher  $\beta$  ratios acquire higher orbital eccentricities. As the eccentricities of particles slightly above the blowout limit are the highest, their radial distribution is the broadest, whereas larger particles stay more confined to their birth regions. In Fig. 4.2b this effect can be seen from how the curves gradually change from the largest ( $s = 110 \mu\text{m}$ ) to the smallest bound grains ( $2 \mu\text{m}$ ). The former essentially follow the distribution of the parent bodies, while the latter exhibit a more extended, flatter radial profile. Finally, blowout grains (e.g., those with  $s = 0.15 \mu\text{m}$  have an  $\propto r^{-2}$  distribution, as expected for a set of hyperbolic orbits streaming outward from their birth locations.

Including the P-R drag (Fig. 4.2c) does little with largest grains, but modifies the profile of smaller ones ( $\sim 1 \mu\text{m}$ ) substantially. The P-R transport inward steepens their profile. Besides, small particles are now present in high amounts at smaller distances, even where no parent bodies are present, in contrast to the case without P-R.

**Coupled Size-Radial Distribution.** Another view of the EKB dust can be achieved by plotting its combined radial and size distribution (Fig. 4.3). Besides presenting the same salient features as those discussed before, it emphasizes that radial and size distribution of dust in a debris disk are intrinsically coupled and cannot be treated independently of each other.

**Optical Depth.** The radial profile of the normal geometrical optical depth is shown in Fig. 4.4. In the case of a disk dominated by the P-R effect, Strubbe & Chiang (2006) calculated analytically the exponent of the optical depth profile  $\tau \propto r^{-\alpha}$  to be  $\alpha = 2.5$  and  $\alpha = 0$  in the outer and inner regions, respectively. Without P-R effect, i.e. for a collision-dominated disk, no dust is present interior to the parent bodies, and the outer slope should be close to  $\alpha = 1.5$ .

These slopes are in qualitative agreement with our simulations (Fig. 4.4). Taking the known EKB objects as dust sources and including the P-R effect, we find a nearly constant optical depth in the inner region and a slope of  $\alpha \approx 3.0$  in the outer disk, close enough to predictions for a transport-dominated disk. For the debiased EKB dust disk and with the P-R effect taken into account, the result is intermediate between what is expected for transport-dominated and collision-dominated disks. This is seen from the inner profile

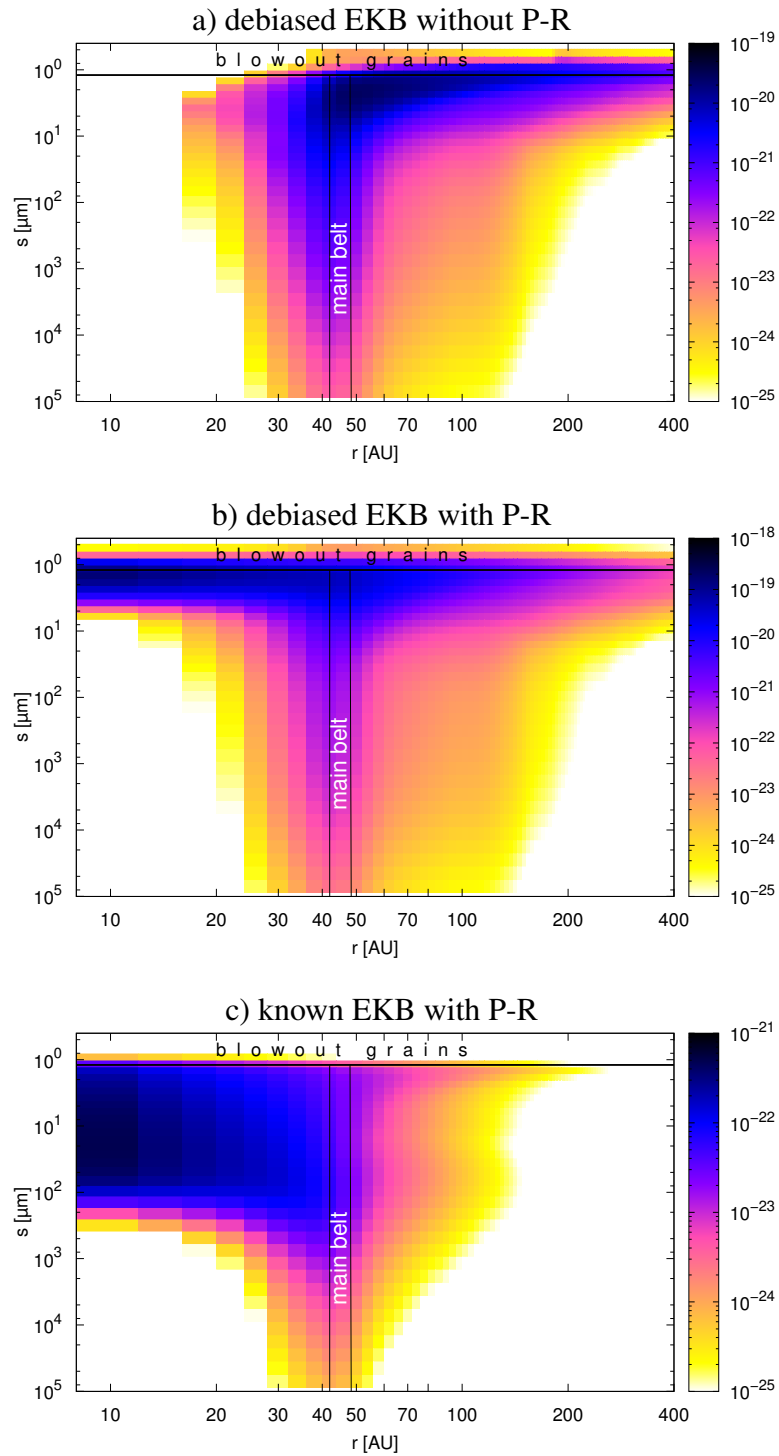


Figure 4.3.: The distribution of the cross-section density of the EKB dust as a function of distance and grain sizes. The panels are as in Fig. 4.2.

which is gently decreasing inward (cf. Fig. 1 of Wyatt, 2005), and from the outer slope of  $\alpha \approx 2.0$ . Finally, for the debiased EKB dust disk, but with the P-R effect switched off, the profile is the one expected for collision-dominated disks. The optical depth drops sharply inward from the main belt, whereas in the outer region the slope is  $\alpha \approx 1.1$ . That it is somewhat flatter than the analytic value  $\alpha = 1.5$ , traces back to a rather broad radial distribution of scattered TNOs that make a considerable contribution to the overall dust profile.

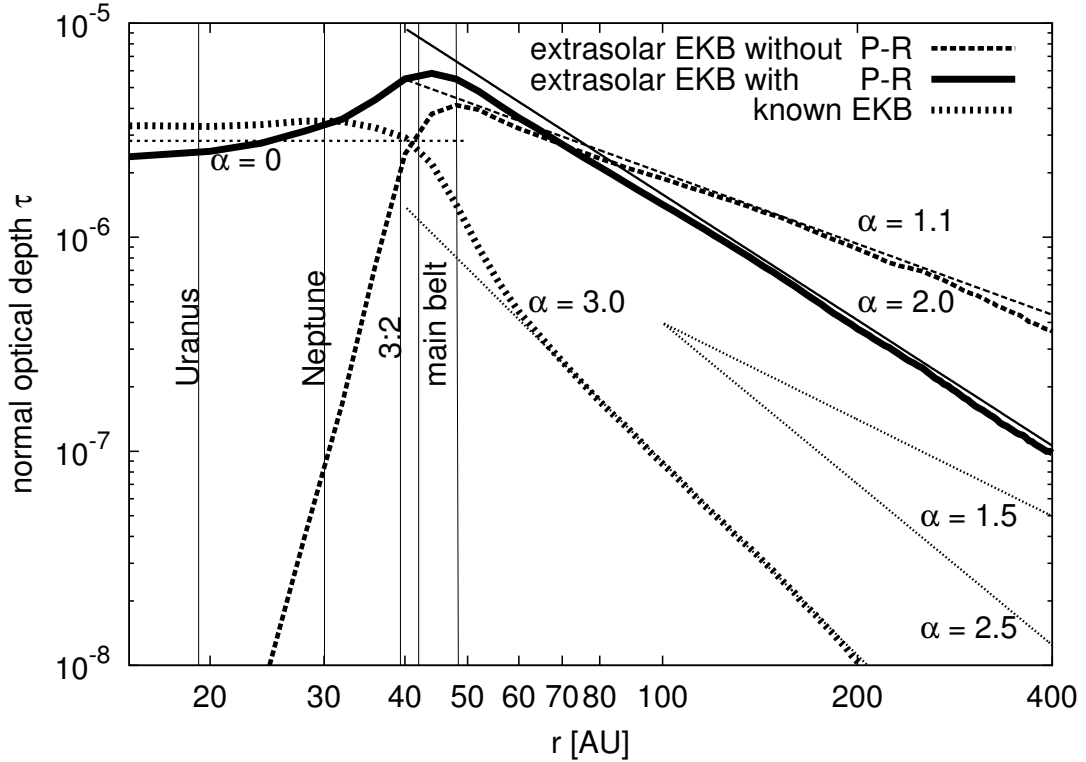


Figure 4.4.: Normal optical depth of the debiased Kuiper belt with and without P-R drag. Uranus and Neptune are shown for orientation, but were not included in the simulations. The optical depth for the known EKB is amplified by a factor of 100.

For the debiased EKB and with P-R effect included, the normal optical depth peaks at  $\approx 40$  AU at a level of  $\approx 6 \times 10^{-6}$ . Besides the normal optical depth shown in Fig. 4.4, we have calculated the in-plane optical depth to  $\tau \leq 2 \times 10^{-5}$  outside 30 AU. We finally note that the dust production rate for the debiased EKB in collisional equilibrium was calculated to  $\lesssim 1.7 \times 10^8 \text{ g s}^{-1}$ .

### 4.3. Thermal Emission

The numerical tool for calculating the spectral energy distribution is called *SEDUCE* (Spectral Energy Distribution Utility for Circumstellar Environments) and was developed by Sebastian Müller (Müller, 2007). Some minor changes in the code were done by the author of this thesis.

The equilibrium temperatures of dust and their thermal emission were calculated in a standard way as described, for instance, in Krivov et al. (2008). In these calculations we computed the Solar photospheric spectrum with the NextGen grid of models (Hauschildt et al., 1999), assuming a G2V star of Solar metallicity. To get a rough idea of how the thermal flux is affected by (unknown) chemical composition of dust, we tested four different cases: ideal material (blackbody absorption and emission), astrosilicate from Laor & Draine (1993), contaminated ice with 10% volume fraction of astronomical silicate and “dirty ice” with a 50 – 50 composition of ice and astrosilicate (Warren, 1984; Laor & Draine, 1993). For brevity we use “ice” for the 10% astrosilicate-contaminated ice and “dirty ice” for the 50% astrosilicate-contaminated ice. This is similar to what, for instance, Yamamoto & Mukai (1998b) adopted in their calculation of thermal emission of the EKB dust. The refractive indices of the adopted ice were calculated by means of the Maxwell-Garnett theory and for the “dirty ice” the Bruggeman mixing rule was used. With a standard Mie algorithm, we then computed the absorption efficiency  $Q_{\text{abs}}$  as a function of size and wavelength. Since most of the emission comes from small particles we limited the calculation of the flux to particles between  $0.1 \dots 3000 \mu\text{m}$ . For particles larger than  $3000 \mu\text{m}$  the size parameter  $2\pi s \lambda^{-1} \gtrsim 3 \times 10^4$  for  $\lambda = 0.5 \mu\text{m}$  (which is the peak emission wavelength of the Sun) and numerical solutions of Mie theory are not appropriate anymore (Wolf & Voshchinnikov, 2004).

#### 4.3.1. Spectral Energy Distribution

The resulting SEDs of the simulated (extrasolar) EKB dust disk, as it would be seen from a 10 pc distance, are presented in Fig. 4.5. Three different curves correspond to the materials blackbody, astrosilicate and ice as described above. Pure astrosilicate and the ice produce SEDs of similar shape and height, peaking at  $50\text{--}70 \mu\text{m}$  with a maximum flux at a level of several mJy. On the ice curve, a typical water ice feature at  $\sim 60 \mu\text{m}$  is seen. This feature may have been detected in the disk of a young debris disk star HD 181327 (Chen et al., 2008). The fact that the feature is located near the peak of the SED may help finding water ice in other debris disks by future observations.

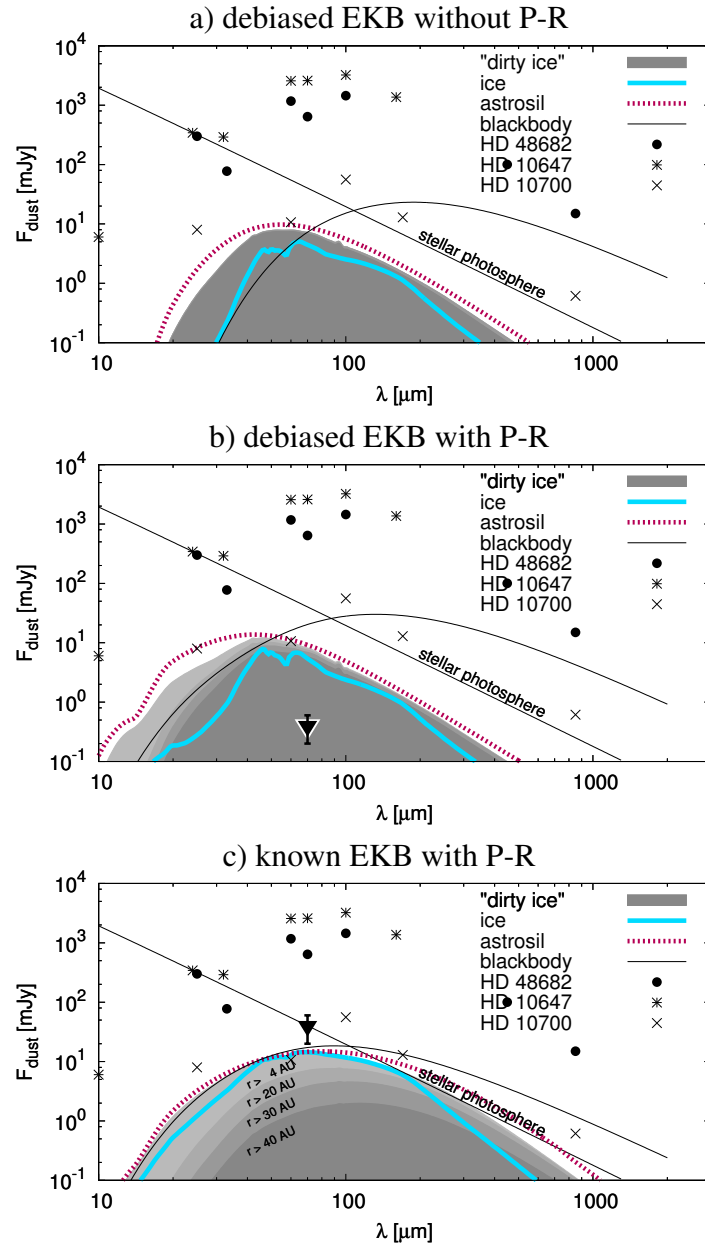


Figure 4.5.: Infrared excess of the Kuiper belt dust. (a): the debiased EKB, without P-R effect; (b): the debiased EKB, with P-R effect; (c): known EKB objects only, with P-R effect (amplified by a factor of 100). Three curves and the gray shades area in each panel (a) to (c) are based on the same *ACE* runs, but the thermal emission was calculated for four different materials: blackbody, astrosilicate, ice, and “dirty ice”. For comparison, observed SEDs of three other old Sun-like stars are shown with symbols. The triangle shows the upper non-detection limit at  $70 \mu\text{m}$  (amplified by 100 for the known EKB).



Finally the gray shaded areas correspond to the “dirty ice”. Different grayshades correspond to different distances. For the known EKB the radial distances are written into the plot. For the debiased EKB the same grayshades represent the same distances as for the known belt. Obviously, nearly all of the flux of the EKB without P-R drag stems from  $r > 40$  AU since no mechanism transports material inward and therefore no material can contribute to the flux. A different result can be seen for the debiased EKB with transport included. Although collision-dominated for all sizes and distances only  $\approx 60\%$  of the maximum flux stems from outside 40 AU. As a straightforward result, only  $\approx 15\%$  of the maximum flux of the transport-dominated known EKB are from  $r > 40$  AU, 33% from  $r > 30$  AU and 57% from  $r > 20$  AU.

A comparison with the blackbody curve readily shows that it departs from the others significantly. The maximum moves to  $\lambda \sim 200 \mu\text{m}$  and the (sub-)mm flux becomes by two orders of magnitude higher than in the other cases. This result confirms earlier conclusion (see, e.g., Yamamoto & Mukai, 1998b; Krivov et al., 2008) that the blackbody assumption is probably too crude and should not be used in modeling the thermal emission of debris disks.

It is important to compare the calculated flux of the debiased EKB with measurements of other known debris disks. For this purpose, photometric data for other Sun-like stars were looked at. Three stars which possess well-known, bright excesses (measured at many wavelengths from mid-IR to sub-mm), which have spectral classes not too far from Solar G2, and which, like the Sun, are rather old ( $\geq 1$  Gyr) were chosen. These are HD 48682 ( $\psi^5$  Aur, G0V, at 17 pc distance, estimated age 0.6–9 Gyr), HD 10647 (q<sup>1</sup> Eri, F8V, 17 pc,  $\sim 2$  Gyr), and HD 10700 ( $\tau$  Cet, G8V, 4 pc, 7 Gyr). Their SEDs, normalized to  $r = 10$  pc, are overplotted in Fig. 4.5. Distances, age estimates, and photometric data for these stars are adapted from Greaves et al. (2004), Sheret et al. (2004), Beichman et al. (2006), Chen et al. (2006), Moór et al. (2006), Lawler et al. (2009), and Tanner et al. (2009). A comparison shows that their SEDs are similar in shape to the simulated SED of the EKB dust disk (for one of the realistic materials, not blackbody). The maximum of the SEDs of the selected debris disk stars lies at  $\sim 100 \mu\text{m}$ , i.e. at slightly longer wavelengths than the maximum of the EKB dust flux. This (moderate) difference in the peak wavelengths of different SEDs may be caused by a choice of chemical composition of the disks, by different extensions of EKB and other debris disks, or both.

The major difference between the EKB dust disk and extrasolar debris disks is, of course, the absolute level of the thermal emission fluxes. For dust maintained by the debiased EKB (panels a and b), the fluxes from far-IR to sub-mm are about one to two

orders of magnitude lower than those of the reference stars. Obviously, this traces back to a much lower total mass of the EKB compared to that of the extrasolar Kuiper belts. The reasons for this difference are currently a matter of debate. For instance, Booth et al. (2009) argue that typical Kuiper belts around stars with observed debris disks may not have undergone a major depletion phase due to a “Late Heavy Bombardment”. Currently, it is not known whether low-mass disks at the EKB level exist around other stars at all and, if they do, how common they are.

It is interesting to compare fluxes from the EKB dust disk (Fig. 4.5b) with those from the dust disk that would stem from the known TNOs, without debiasing. The corresponding SEDs, depicted in Fig. 4.5c, are completely different. Apart from an expected reduction of the fluxes by almost two orders of magnitude, two other effects are seen. One is that the astrosilicate and ice SEDs come much closer to each other and to the blackbody curve. As a result, their maxima shift to longer wavelengths of  $\sim 100 \mu\text{m}$ . Another effect is a disappearance of the water ice feature. Both effects are easily explained by the major differences between the size distribution of dust of the known and debiased EKBs (see middle and bottom panels in Fig. 4.1). In the dust disk of the known EKB, the cross section, and thus the thermal emission, are dominated by grains  $\sim 100 \mu\text{m}$  in size. Such big grains behave as black bodies and do not produce any distinctive spectral features.

For three selected wavelengths of  $70 \mu\text{m}$ ,  $100 \mu\text{m}$ , and  $160 \mu\text{m}$ , which are the wavelengths measured by Herschel/PACS<sup>20</sup>, the fluxes calculated for the known and debiased EKB and for all four assumed materials are also tabulated in Table 4.1. Solar photospheric fluxes are given for comparison. These values are used below to assess the detectability of debris disks similar to the EKB with Herschel.

Table 4.1.: Calculated flux of the known and debiased (deb) Kuiper belt dust (including the P-R effect) and photospheric flux of the Sun at different wavelengths from a 10 pc distance. The fluxes are given in mJy.

$\lambda$ [ $\mu\text{m}$ ]	astrosil		“dirty ice”		ice		blackbody		Sun
	known	deb	known	deb	known	deb	known	deb	
70	0.1	7.9	0.1	8.1	0.1	4.8	0.12	17.3	40
100	0.1	4.1	0.1	3.8	0.1	2.1	0.14	24.7	22
160	0.08	1.5	0.07	1.4	0.06	0.9	0.11	25.5	7.8

<sup>20</sup>Photodetector Array Camera and Spectrometer.

**The Model is Wrong.** Finally, the triangle in Fig. 4.5 is the upper non-detection limit at  $70\ \mu\text{m}$  of the COBE mission (Backman et al., 1995; Greaves & Wyatt, 2010). As it is shown, our model of the debiased EKB would violate this non-detection limit. In other words the COBE spacecraft would have detected the EKB dust flux. We know this is not the case and have to think about the reasons of this contradiction. Either our debiasing algorithm overestimates the TNOs by a lot or the extrapolation method as described in Sec. 4.1 is wrong. Since the total mass of the debiased EKB is consistent with other results obtained by different methods (see discussion in Chapter 3), the extrapolation method has to be reconsidered. Therefore, we included the reported break in the size distribution at several tens of kilometers in radius and do the same collisional modeling. This is done in Chapter 5.

Although now knowing that we cannot use this model to describe the actual EKB, it is still useful to analyze the influence of the increased mass of the parent bodies and the P-R drag. Furthermore, we do not know whether such a break is typical for other debris disks and so this model can still be used to model disks without a break in the size distribution.

### 4.3.2. Surface Brightness Synthetic Images

For the calculation of synthetic surface brightness images the numerical code *SUBITO* (SURface Brightness Investigation TOol) was used, developed by Sebastian Müller with minor contributions from the author of this thesis.

Another view on the of the thermal emission is through surface brightness (synthetic) images. These were calculated using the same parameters as for the SED. As material “dirty ice” was chosen.

Figure 4.6 shows the normalized surface brightness of an EKB analog without and with P-R drag and of the known EKB at the wavelengths  $70\ \mu\text{m}$ ,  $160\ \mu\text{m}$  and  $800\ \mu\text{m}$ . With the assumption of azimuthal symmetry no resonant structures can be seen. This is similar to the well known Vega disk (Su et al., 2005) .

Without the artificially excluded transport the EKB would qualitatively look the same for every shown wavelength. The inner region would be clear of material and the bulk of the emission originates from the main belt as seen in the left column of Fig. 4.6. The middle column of the same Figure shows the more realistic version of the EKB since P-R drag is always present. Although collision-dominated (see Fig. 4.1) transport will lead to a significant flux increase inside the main belt at least for the  $70\ \mu\text{m}$  image (cf. Fig. 4.5). The  $160\ \mu\text{m}$  and  $800\ \mu\text{m}$  flux comes from larger particles whose collisional timescale is much shorter than the transport timescale and therefore are not transported

inward. As a consequence, the contribution for larger wavelengths to the flux from inside the main belt is of minor importance. This can be compared with the  $800\ \mu\text{m}$  image of the known EKB, where  $100\ \mu\text{m}$  sized particles are transport-dominated (Fig. 4.1) and so can contribute to the  $800\ \mu\text{m}$  flux even inside the main belt. For the  $70\ \mu\text{m}$  and  $160\ \mu\text{m}$  image this actually leads to an image where it is not possible to see the parent body belt anymore.

Without applying the debiasing algorithm to the known parent bodies there is nearly no contribution from the scattered objects and therefore the area outside the main belt is nearly empty ( $70\ \mu\text{m}$  and  $160\ \mu\text{m}$  image of the known EKB).

### 4.3.3. Detectability of “Kuiper Belts”

We would like to estimate the level, down to which Herschel can detect faint debris disks, and then to compare that level with the EKB dust disk models obtained in this Chapter.

The sensitivity limit of the PACS instrument (Poglitsch et al., 2010) of the Herschel Space Observatory (Pilbratt et al., 2010) at  $100\ \mu\text{m}$  in the scan-map mode for one hour exposure time is  $5.5\ \text{mJy}$  at a  $5\sigma$  uncertainty level<sup>21</sup>, or  $1.1\ \text{mJy}$  at  $1\sigma$ . The background noise, of course, is highly variable from one star to another. For 133 target stars of the Open Time Key Program DUNES (DUst around NEarby Stars; Eiroa et al., 2010), its average value at  $100\ \mu\text{m}$  is  $0.53\ \text{mJy}$  at  $1\sigma$ . Combining the instrument and the background noise leads to a limiting flux as low as  $5\sqrt{1.1^2 + 0.53^2} = 6.1\ \text{mJy}$  for one hour exposure time at a  $5\sigma$  uncertainty level. Assuming that the  $100\ \mu\text{m}$  flux is proportional to the total mass of a debris disk, we can conclude that the EKB with a mass of  $M > 2.9M_{\text{EKB}}$  will be detectable from a distance of  $10\ \text{pc}$ , assuming “dirty ice” as a dust composition. For silicate dust, the detectability limit would go down to  $1.5M_{\text{EKB}}$ . Additional uncertainties in the stellar photospheric flux ( $\approx 2\%$  of  $22\ \text{mJy}$ , or  $0.4\ \text{mJy}$ ) increase these values slightly to  $\approx 3.1M_{\text{EKB}}$  and  $\approx 1.6M_{\text{EKB}}$ , respectively.

<sup>21</sup><http://herschel.esac.esa.int/Docs/PACS/html/ch03s05.html#sec-photo-sensitivity>  
(Last accessed on 02 April 2012)

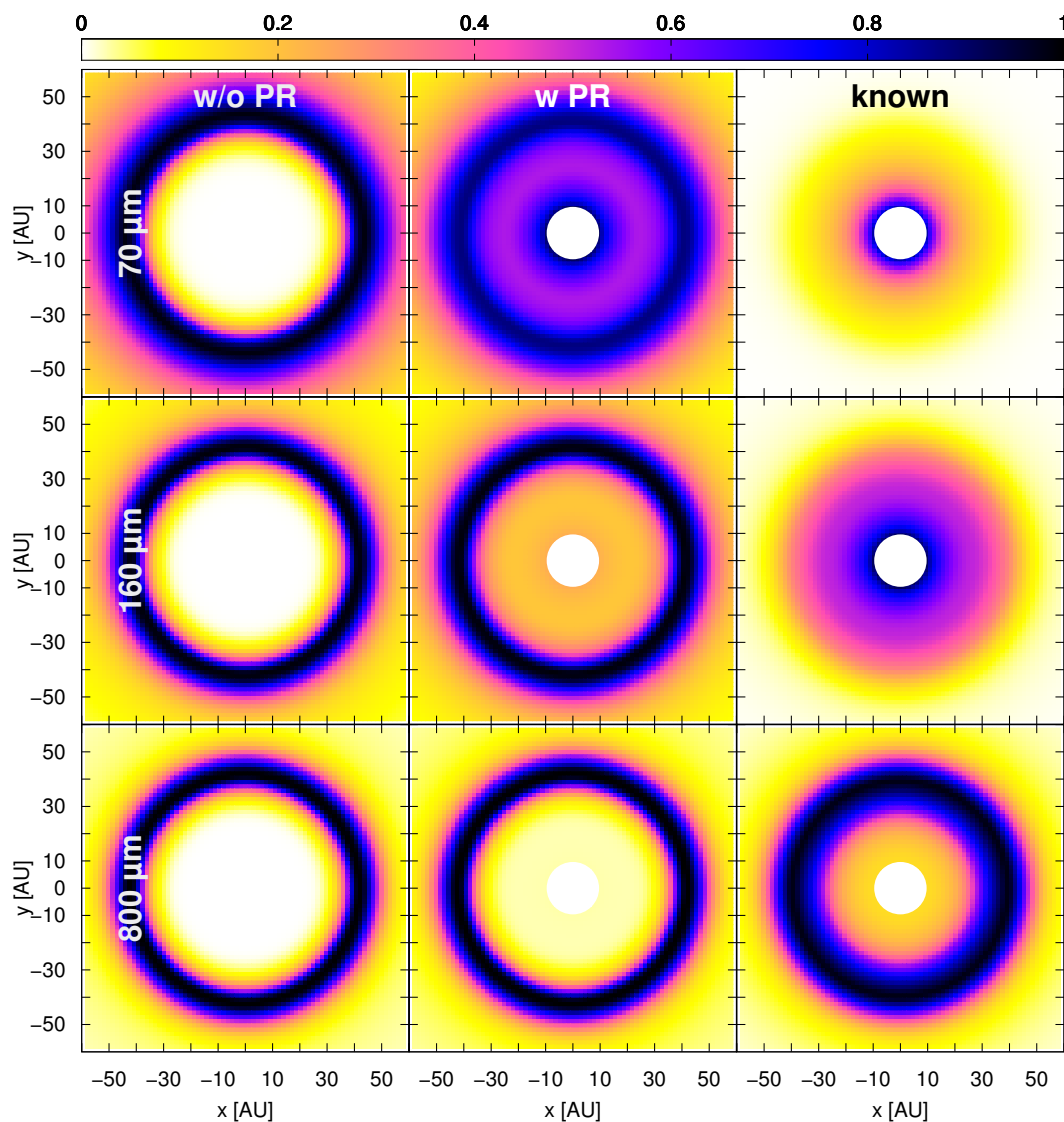


Figure 4.6.: Normalized surface brightness images of the EKB without P-R drag (left column), with P-R drag (middle column) and the known EKB (right column) at  $70 \mu\text{m}$  (upper panel),  $160 \mu\text{m}$  (middle panel) and  $800 \mu\text{m}$  (lower panel).

# 5. An Improved Model of the Edgeworth-Kuiper Debris Disk

Outside intelligences, exploring the Solar System with true impartiality, would be quite likely to enter the Sun in their records thus: Star X, spectral class G0, 4 planets plus debris.

---

Иaac Aлимob (1920-1992)

*This Chapter is based on Vitense et al. (2012). The analyses and results presented here were obtained in conjunction with Alexander Krivov, Hiroshi Kobayashi, and Torsten Löhne and are used here with their permission.*

With the information that an EKB which is in collisional equilibrium for all sizes is inconsistent with the COBE upper non-detection limit we try other extrapolations from parent bodies to dust sizes. In this Chapter we successfully find models which are consistent with the described COBE limit *and* can reproduce the data from the New Horizons dust counter. As further improvement to the previous Chapter, we drop the assumption of blackbody grains and analyse the influence of resonance capturing and scattering by planets and the effect of sublimation.

## 5.1. Setup of the Collisional Simulations

As learnt in the previous Chapter we have to reconsider the extrapolation method. Therefore, we start with general remarks about the size distribution in the EKB and its evolution since the early phases of the Solar System formation. Because it is not known how planetesimals in the Solar nebula have formed (cf. Sec. 1.2), their primordial size distribution is unclear. In standard coagulation scenarios, the bottom-up growth of planetesimals could have resulted in a broad size distribution (e.g., Kenyon & Bromley, 2008), with a more or less constant slope across all sizes up to roughly the size of Pluto. Alternatively, local gravitational instability in turbulent disks would have produced predominantly big ( $\sim 100$  km) planetesimals (Johansen et al., 2006, 2007; Cuzzi et al., 2008; Morbidelli

et al., 2009), implying a knee in the size distribution at these sizes, which is indicated by several observations (Bernstein et al., 2004; Fuentes & Holman, 2008; Fraser & Kavelaars, 2009; Fuentes et al., 2009). Next, according to the Nice model (Gomes et al., 2005; Levison et al., 2008; Morbidelli, 2010), the primordial Kuiper belt was compact (between 15 and 35 AU) and massive ( $\sim 35 \dots 50$  Earth masses). With these parameters, the EKBOs with sizes up to a few kilometers would have been collisionally processed by the time of the Late Heavy Bombardment (LHB) in  $\approx 800$  Myr from the birth of the Solar System (see Sec. 5.6). Therefore, the size distribution consisted of two parts before the LHB. Objects smaller than a few km had a size distribution set by their collisional evolution in the early massive EKB, whereas larger objects retained a primordial distribution set by their formation process. The LHB has then resulted in a dynamical depletion of the EKB, which was obviously size-independent (Wyatt et al., 2011). As a result, the entire size distribution must have been pushed down, retaining its shape. During the LHB, the EKB has reduced its original mass by a factor of  $\sim 1000$  (Levison et al., 2008) and expanded to its present position. Both the reduction of mass and the increase of distance to the Sun have drastically prolonged the collisional lifetime of the EKBOs of any given size. As a result, only objects smaller than about a hundred of meters in radius (see Sec. 5.2 for more accurate numbers) experienced full collisional reprocessing during the subsequent 3.8 Gyr. We conclude that the size distribution in the EKB after the LHB, and in the present-day EKB, is likely to consist of three parts. Objects smaller than a hundred meters (more accurate numbers are given below) must currently reside in a collisional equilibrium, those with radii between a hundred meters and a few kilometers inherit the collisional steady-state of the massive and compact belt of the pre-LHB stage, and the largest EKBOs still retain a primordial size distribution from their accretion phase.

If we were able to set an initial size and orbital distribution of bodies (i.e. the one after the completion of the LHB) in a reasonable way, we could simply run the code over 3.8 Gyr to see which dust distribution it yields. Setting the initial distribution at largest EKBOs, i.e. the third of the three parts of the entire size distribution described above, is straightforward. Because the distribution of these objects remains nearly unaltered since the LHB, their initial distribution should be nearly the same as the current one. We use the parent bodies as obtained in Chapter 3 and directly filled the  $(m, q, e)$ -bins at the beginning of each simulation with the objects of the “true” Kuiper belt as done in the previous Chapter. Then we extrapolated toward smaller sizes the same way as described in Sec. 4.1 with a power law  $dN \propto s^{-q} ds$ . The slope  $q$  is unknown, so we explored the following possibilities (thin lines in Fig. 5.1):

1. Run “d” (“Dohnanyi extrapolation”). We assume the classical Dohnanyi (1969) law with  $q = 3.5$ . This extrapolation is similar to the one used in Chapter 4.
2. Run “f” (“flat extrapolation”). We assume  $q = 3.0$  for  $s < 10$  km. Run “f” can be treated as a rough proxy for a break in the size distribution at a few tens of kilometers reported in the literature:  $q \approx 1.9$  (Fraser & Kavelaars, 2009),  $q \approx 2.0$  (Fuentes et al., 2009) and  $q \approx 2.5$  (Fuentes & Holman, 2008). Keeping in mind that the observed TNOs include several populations, and that the knowledge of scattered objects is particularly poor (see Chapter 3), we made an additional run “f<sub>CKB</sub>” identical to “f”, but without the scattered objects.
3. Run “n” (“no extrapolation”). Here, we refrain from any extrapolation, assuming that the system was devoid of smaller objects initially. This formally corresponds to  $q \rightarrow -\infty$ .

In the *ACE* simulations for this Chapter, we used the following size-pericentric distance-eccentricity grid. As a minimum grain radius, we chose  $0.4 \mu\text{m}$  and set size ratios of the adjacent bins of 1.5 for dust sizes and 2.3 for the largest TNOs. To cover the heliocentric distances from 4 AU to 400 AU we used a logarithmically spaced pericenter grid with 21 bins as well as a linearly spaced eccentricity grid between  $-1.5$  and  $1.5$ , the semi-opening angle of the disk was set to  $i \approx 8^\circ$ . To make sure that this fairly coarse grid yields sufficiently accurate results, we made another “n” run with a finer, more extended grid with a minimum grain radius of  $0.3 \mu\text{m}$  with size ratios of the adjacent bins of 1.25 for dust sizes and 1.58 for the largest TNOs, 41 pericenter bins and eccentricity bins between  $-5$  and  $5$ . We found that our coarse grid leads to almost the same results as the fine grid model.

For the material properties, we assumed a mixture of 50% ice (Warren, 1984) and 50% astrosilicate (Laor & Draine, 1993) with a bulk density of  $2.35 \text{ g cm}^{-3}$ . The optical constants of the mixture were computed with the Bruggeman mixing rule and the absorption coefficients with a standard Mie algorithm. For values of the critical fragmentation energy (see Eq. 2.18) we used the same values as written in Sec. 2.3.

## 5.2. Results of the Collisional Simulations

All extrapolations described in Sec. 5.1 are rather arbitrary, and the last one is obviously unrealistic. A natural question is then, which of the models, and after which timestep, will deliver the distributions that match the actual distributions of the EKB material the best. We start with the integration time. Each of the runs was let continue as long as



needed to reach a collisional equilibrium at smaller sizes, but not too long to preserve the initial distribution of larger objects. A boundary between “smaller” and “larger” sizes was arbitrarily set to  $s \sim 1$  km. We considered “collisional equilibrium” to have been reached once the shape of the size distribution stopped changing. To meet these criteria in the “n” run, we had to let the system evolve much longer than the age of the Universe. Of course, this “modeling time” should not be misinterpreted as the physical time of the EKB evolution. This was merely the time needed for the population of large bodies to generate a sufficient amount of smaller debris down to dust sizes.

The results obtained over the integration interval chosen in this way are shown in Figs. 5.1–5.3 with thick lines. These three figures show the size distribution, the radial profile of the normal geometrical optical depth, and the collisional lifetime of the objects, respectively. We note that at an earlier stage of evolution the cross-section density and the normal optical depth would be lower, and the lifetime of dust grains longer, while a later stage of evolution would lead to more dust and therefore to a higher cross-section density and optical depth and reduced lifetime of the particles.

The question is which of the models, “d”, “f”, of “n” — if any — matches the actual dust distribution in the present-day EKB best? The only way to answer this question is to compute the observables for each of the simulations and compare them with in-situ spacecraft measurements and thermal emission constraints. Although an in-depth analysis of the data is deferred to Sec. 5.5, we now take a first quick look. The gray shaded rectangle in Fig. 5.1 is a rough approximation of the dust flux data collected by New Horizons, translated into the cross-section density and extrapolated to the distance of the classical EKB. A comparison with the evolved curves demonstrates that the “d” run is far too dusty. It cannot reach an evolutionary stage that would be consistent with the measurements (and with the upper limit from the non-detection of the thermal emission) as already showed and explained in Chapter 4. Consequently, we showed here, with a completely different type of argument, that a break in the size distribution *has* to be present in the EKB, as found from the analysis of TNO observations (Fuentes & Holman, 2008; Fraser & Kavelaars, 2009; Fuentes et al., 2009).

How about the other runs? Both the “f” and the “n” runs are consistent with the observational data; we will confirm this in Sec. 5.5 by a more thorough analysis. Thus — unfortunately — we cannot constrain the size distribution of EKBOs more tightly. Nor can we say which of the dust distributions, the one of the “f” run or the “n” run, can be expected in the EKB, although the shape of the curves in these runs is different. (The only common feature shared by all the curves is an abrupt drop at  $\approx 0.5 \mu\text{m}$ , which is the limit

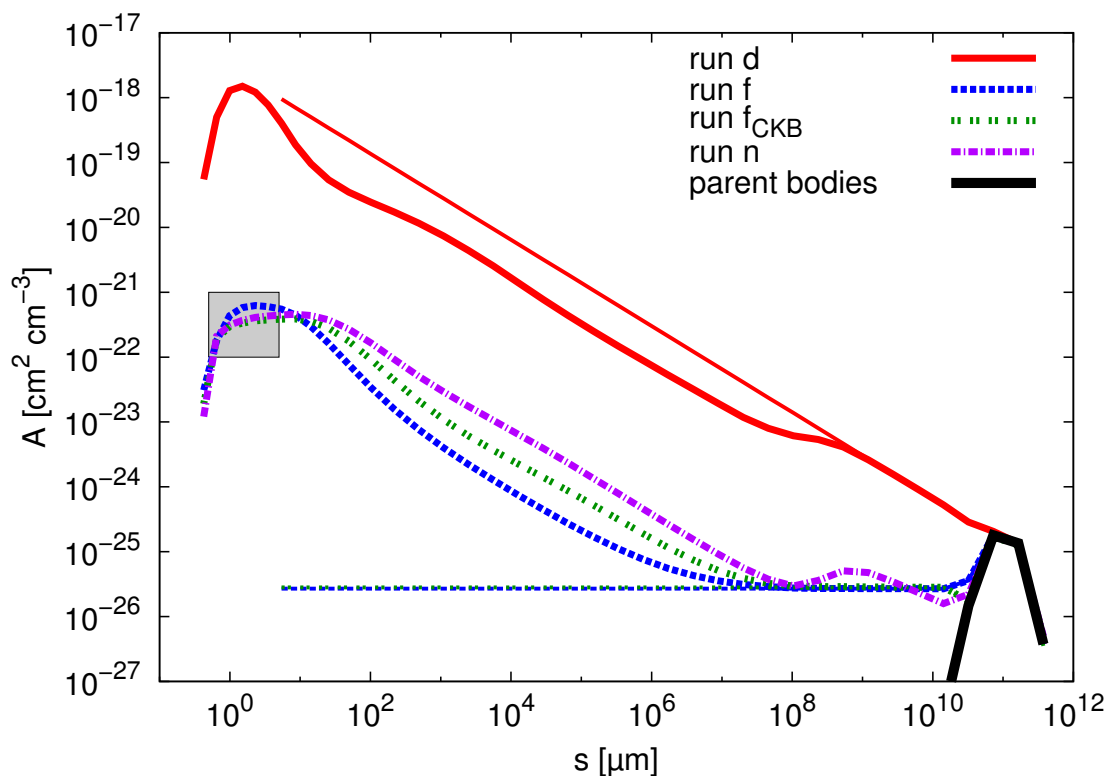


Figure 5.1.: Size distributions in different collisional runs. Thin lines are initial distributions, while thick ones correspond to an advanced state of collisional evolution. Note that the initial size distribution of the “n” run coincides with the debiased population of TNOs.  $A$  is the cross-section density per size decade at a distance of 40 AU. Note that  $A = \text{const}$  (i.e. horizontal lines) corresponds to a size distribution with  $q = 3$ , where different-sized objects equally contribute to the cross section. The gray shaded rectangle is a rough approximation of the particle dust flux given by New Horizons translated into the cross-section density and distances of the EKB.

below which the grains are swiftly removed from the system by radiation pressure.) We now come to an analysis of these differences.

The size distribution in the “d” run, which we rejected because it violated the observational constraints, is typical of a collision-dominated disk. At all sizes, the dust transport is less efficient than the collisional grinding, and the cross-section density peaks just above the blowout limit (cf. Krivov et al., 2006; Thébault & Augereau, 2007). This is also confirmed by the radial profile shown in Fig. 5.2. The outer slope of  $\approx 1.2$  agrees well with an approximate analytic solution for a collision-dominated disk that predicts a slope of  $\approx 1.5$  (Strubbe & Chiang, 2006). Also, there is a clear decrease of the optical depth toward the

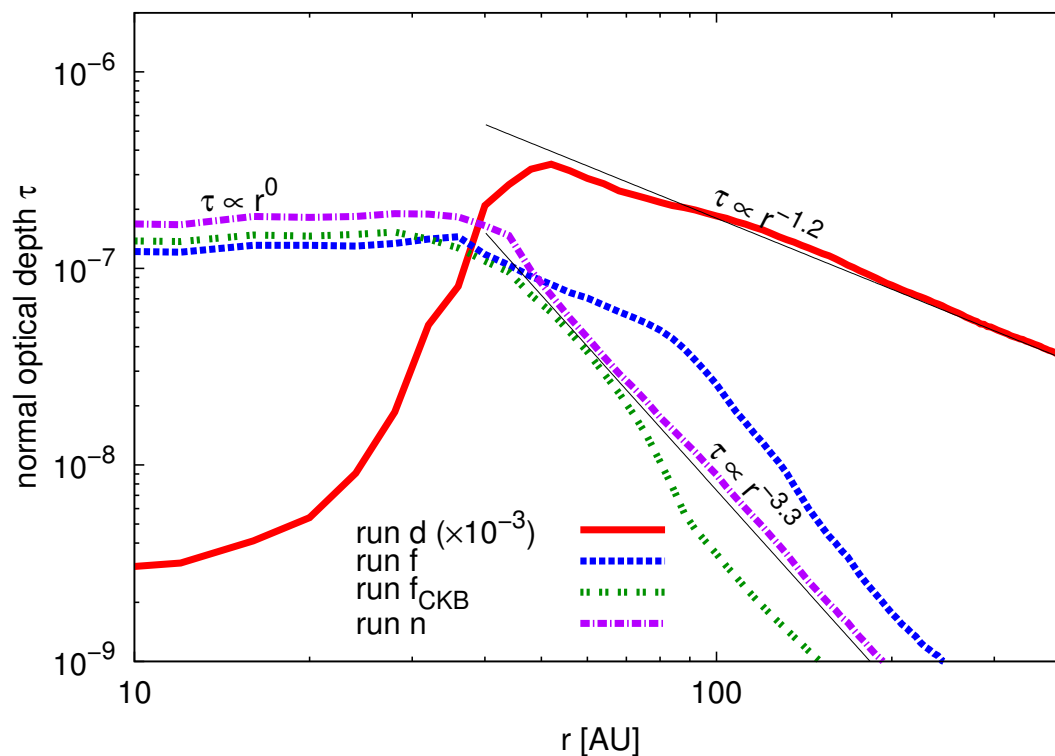


Figure 5.2.: Normal optical depth for the same *ACE* runs and time instants as in Fig. 5.1.

star, caused by collisional elimination of the particles. Since we ruled out this extrapolation, additional results for the “d” run are presented for comparison but not discussed anymore. As mentioned above, the “d” run is essentially the same as the run in Chapter 4 (made for the debiased EKB, with the Poynting-Robertson effect included), therefore we refer to this Chapter for a detailed analysis of the “d” run.

The size distribution in the “n” run is different. It shows a broad maximum at  $\sim 100 \mu\text{m}$ , which indicates that particles smaller than that are transported inward from the dense part of the disk before they are lost to collisions (Wyatt et al., 2011). The inner part of the radial profile in Fig. 5.2 is nearly constant, and the outer one reveals a steeper slope of  $\approx 3.0$ , as predicted analytically for a transport-dominated disk ( $\approx 2.5$ , Strubbe & Chiang 2006). Note that the outer profiles are generated by particles in a narrow range of sizes around the blowout limit. The coarse size grid in our models therefore limits the accuracy with which we can reproduce these slopes.

The “f” run seems to be intermediate. Although the maximum in the size distribution is broader than in the “d” run, it still resembles the curves typical of collision-dominated

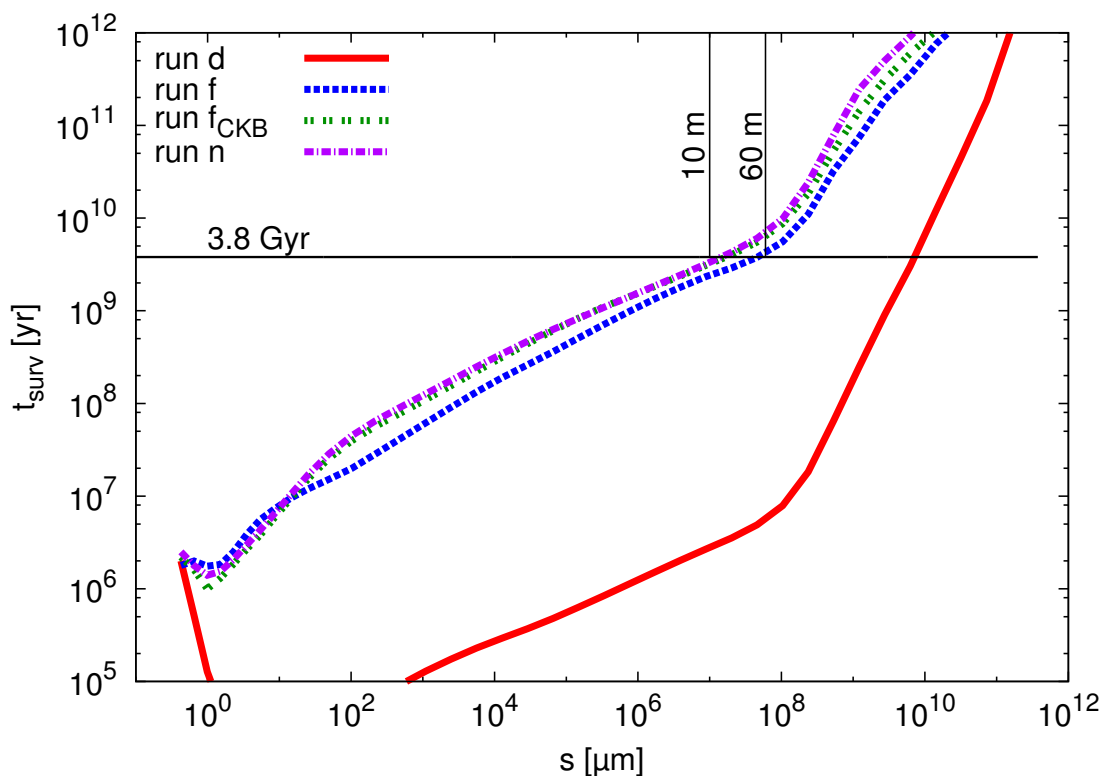


Figure 5.3.: Lifetimes of dust grains and parent bodies for the same *ACE* runs and time instants as in Fig. 5.1. Particles below the 3.8 Gyr line are in a collisional equilibrium after the LHB. A steep rise in the lifetime at  $s \sim 300$  m corresponds to the strength–gravity transition of the critical disruption energy.

disks. However, the profile of the normal optical depth (Fig. 5.2) stays nearly constant inside the main belt, which is typical of transport-dominated disks (e.g., Wyatt, 2005).

Figures 5.1–5.3 also present the results of the additional “ $f_{\text{CKB}}$ ” run, from which we excluded scattered objects as dust parent bodies. Figure 5.1 shows, somewhat unexpectedly, that the results of “ $f$ ” and “ $f_{\text{CKB}}$ ” runs differ from each other: the dust disk in the latter turns out to be transport-dominated, similar to the “ $n$ ” run. The question is why. This is not because dropping the scattered objects just reduces the amount of material in the EKB, resulting in reduced collisional rates. A test simulation in which we artificially augmented the mass of the classical EKB to the total mass of the expected EKB brought qualitatively the same results as the “ $f_{\text{CKB}}$ ” run. Instead, the answer can be found in the method of extrapolation. As explained before, we filled the  $(m, q, e)$ -bins with our debiased population of EKBOs and extrapolated toward smaller sizes with a power law into the same  $(q, e)$ -bins. That means that we transferred the high eccentricities of the

large scattered objects to all smaller ones. Although higher eccentricities do not lead to higher collisional rates (see Krivov et al., 2007, discussion after their Eq. (17)), they increase the relative velocities, making collisions more disruptive. In the “f” run a large amount of  $s < 10 \mu\text{m}$  particles is produced, leading to a higher number and cross-section density for these particles, which in turn leads to a higher collisional rate and a shorter collisional lifetime for larger particles (Fig. 5.3). Without the eccentric orbits of scattered objects (“f<sub>CKB</sub>” run), the relative velocities are moderate, collisions are less disruptive and fewer small particles are produced. Therefore, destruction of larger grains becomes less efficient, leading to a prolonged collisional lifetime.

The above discussion demonstrates that it remains unclear whether the EKB dust disk is transport- or collision-dominated. It is most likely that it is either transport-dominated or intermediate between a collision- and transport-dominated disk. However, in all the runs considered, the inner part of the dust disk (inside the classical EKB) has a nearly constant radial profile of the optical depth of  $\tau_{\perp} \sim 1 \times 10^{-7}$  (Fig. 5.2; For comparison, the in-plane optical depth for  $r > 10 \text{ AU}$  is  $\tau_{\parallel} = 1 \dots 2 \times 10^{-6}$ , which is in good agreement with the estimates from Stern 1996, who found  $\tau = 3 \times 10^{-7} \dots 5 \times 10^{-6}$ ). This suggests that collisions in the inner part of the disk can be neglected. This justifies that in this section we first simulated a completely planet- and sublimation-free EKB and will include the effects of planetary scattering and sublimation below, in Sec. 5.3 and 5.4.

Figure 5.3 shows the mean collisional lifetimes averaged over *all* distances for the same *ACE* runs at the same time instants. Note that the collisional lifetime in the main belt is much shorter than the average one because the density there is much higher and therefore collisions are more frequent. The horizontal line represents a lifetime of 3.8 Gyr, which is the time elapsed after the LHB. All grains below this line are in a collisional equilibrium in the present EKB. For all simulations this size is just about 10 . . . 60 m. The distribution of all objects larger than that equilibrium size was set before the LHB and cannot be constrained with our collisional model.

We finally state that the calculated dust production rate is  $2 \times 10^6 \text{ g s}^{-1}$  and is by an order of magnitude lower than the predicted rate of  $5 \times 10^7 \text{ g s}^{-1}$  from Landgraf et al. (2002) on the base of in-situ measurements of Pioneer 10 and 11. The reason of this difference is their assumed size distribution index of  $q = 3.5$  whereas we found a flatter one which lowers the dust production rate.

### 5.3. Influence of Planets

Giant planets interact gravitationally with dust in the outer Solar System. On the one hand, the grains drifting inward by the Poynting-Robertson (P-R) drag (Burns et al., 1979) can be captured by planets into outer mean-motion resonances (e.g., Liou & Zook, 1999; Moro-Martín & Malhotra, 2002; Kuchner & Holman, 2003; Moro-Martín & Malhotra, 2003, 2005; Stark & Kuchner, 2009; Kuchner & Stark, 2010). On the other hand, the grains that cross the planet's orbit can be scattered. Both effects are able to modify the size and spatial distribution of dust in the disk. In this section, we investigate the efficiency of capturing and scattering.

#### 5.3.1. Resonant Trapping

Mustill & Wyatt (2011) developed a general formalism to calculate the capture probability of a particle into the first- and second-order resonances with a planet. Their theory is valid for any convergent differential migration of the particle and the planet (for instance, if the particle is drifting inward and the planet is migrating outward). Their results are presented in terms of the generalized momentum  $J$  and a dimensionless drift rate  $\dot{B}$  ( $\beta$  in their paper).

The generalized momentum  $J$  is related to the orbital eccentricity of the particle reaching the resonance location,  $e$ , while the dimensionless drift rate  $\dot{B}$  can be expressed through the differential change rate of the particle's semimajor axis at the location of a resonance,  $\dot{a}_{\text{res}}$ , and the semimajor axis itself,  $a_{\text{res}}$ . Below, we make estimates for the 3:2 resonance with Neptune. Using Eqs. (3) and (4) of Mustill & Wyatt (2011), we find the following conversion relations:

$$J = 5893.36 \left( \frac{m_{\text{N}}}{m_{\oplus}} \right)^{-2/3} e^2 \quad (5.1)$$

$$\dot{B} = -0.818921 \left( \frac{m_{\text{N}}}{m_{\oplus}} \right)^{5/6} \sqrt{\frac{a_{\text{N}}}{\text{AU}}} \frac{a_{\text{N}}}{a_{\text{res}}} \frac{\dot{a}_{\text{res}}}{1 \text{ AU Myr}^{-1}}, \quad (5.2)$$

where  $m_{\oplus}$  and  $m_{\text{N}}$  denote the masses of Earth and Neptune, respectively, and  $a_{\text{N}}$  is the semimajor axis of the Neptune orbit.

We now assume that  $\dot{a}_{\text{res}}$  is caused by P-R drag (Wyatt & Whipple, 1950)

$$\begin{aligned}\dot{a}_{\text{res}} &= -1.3 \frac{\beta GM_{\odot}}{c a_{\text{res}}} \frac{2 + 3e^2}{(1 - e^2)^{3/2}} \\ &= -815 \frac{\beta}{a_{\text{res}}[\text{AU}]} \frac{2 + 3e^2}{(1 - e^2)^{3/2}} \frac{\text{AU}}{\text{Myr}},\end{aligned}\quad (5.3)$$

where the prefactor 1.3 accounts for the enhancement of P-R drag by Solar wind drag (Burns et al., 1979) and  $\beta$  is the radiation pressure to gravity ratio for the particle as introduced in Sec. 2.2.3. The enhancement by Solar wind drag is included in the subsequent analysis but we will call it P-R drag for brevity. The  $\beta$ -ratio not only controls the drift rate, it also reduces the effective Solar mass felt by the particle by a factor of  $(1 - \beta)$ . This affects the resonance location, so that  $a_{\text{res}}$  reads

$$a_{\text{res}} = a_{\text{N}} \sqrt[3]{1 - \beta} (3/2)^{2/3}. \quad (5.4)$$

Inserting Eqs. (5.3) and (5.4) into Eq. (5.2), the latter takes the form

$$\dot{B} = 1.6 \frac{\beta}{(1 - \beta)^{2/3}} \frac{2 + 3e^2}{(1 - e^2)^{3/2}}. \quad (5.5)$$

Using the capture probabilities as functions of  $J$  and  $\dot{B}$  from Mustill & Wyatt (2011) and applying Eqs. (5.1) and (5.5), we computed the probabilities as functions of  $e$  and  $\beta$  (or equivalently, particle radius  $s$ ). The results for the 3:2 resonance with Neptune are shown in Fig. 5.4. Although capturing for grains  $s > 0.6 \mu\text{m}$  and  $e < 0.03$  seems unavoidable, it is not obvious what is the fraction of particles of those sizes that will actually have such low eccentricities. The reason is that small particles, when released from parent bodies in nearly-circular orbits, are sent by radiation pressure into large and highly-eccentric orbits. Subsequently, drag forces reduce the semimajor axes and eccentricities of the grains. Yet, it is not clear how low the eccentricities will be by the time when the grains will have reached the resonance location.

To find this out, we first consider parent bodies with elements  $a_{\text{p}}$  and  $e_{\text{p}}$  and compute the initial semimajor axis  $a_{\text{i}}$  and the eccentricity  $e_{\text{i}}$  of a grain upon release. To this end, we use Eqs. (19)–(20) of Krivov et al. (2006), in which we neglect the mass of the projectile compared to the mass of the target, i.e. the parent body, and assume that ejection occurs

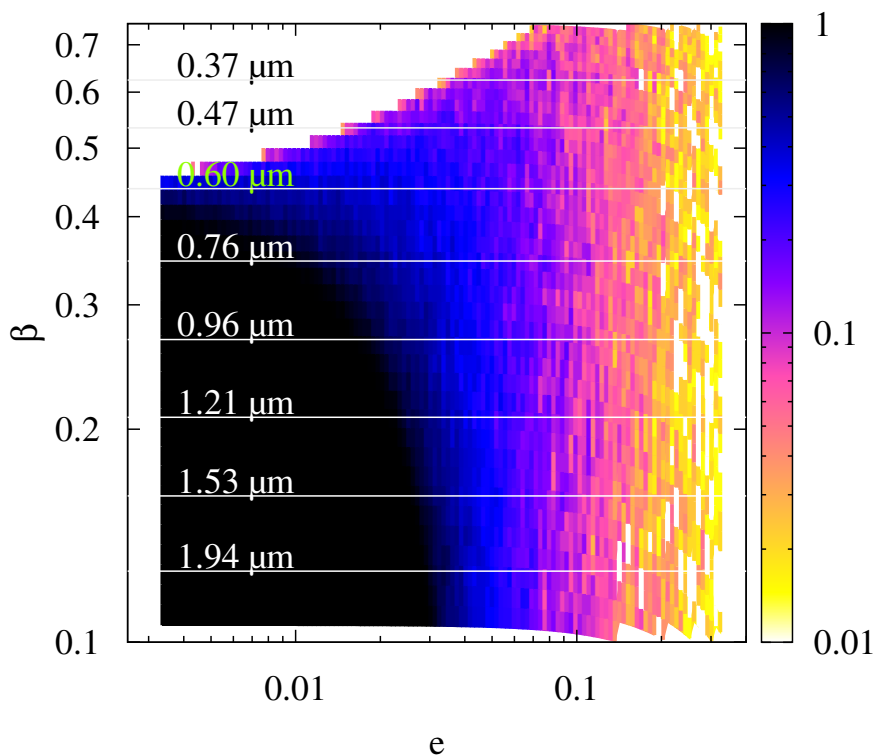


Figure 5.4.: Capture probability of a single particle with given  $\beta$  and  $e$  at the location of the 3:2 resonance with Neptune.

at the pericenter of the parent body orbit:

$$a_i = a_p \frac{(1 - \beta)(1 - e_p)}{1 - e_p - 2\beta} \quad (5.6)$$

$$e_i = \frac{\beta + e_p}{1 - \beta}. \quad (5.7)$$

Subsequently, the P-R drag will decrease  $a_i$  and  $e_i$ . Denoting by  $e_f$  the final eccentricity – i.e. the one the grain will have at the location of a resonance,  $a_{\text{res}} = a_f$  – and using the dependence of  $\dot{a}$  on  $\dot{e}$  as given in Wyatt & Whipple (1950)

$$\frac{de}{da} = \frac{5}{2a} \frac{e(1 - e^2)}{2 + 3e^2} \quad (5.8)$$

leads to

$$\left( \frac{e_f}{e_i} \right)^{4/5} \frac{1 + e_i^2}{1 - e_f^2} = \frac{a_f}{a_i}. \quad (5.9)$$



As an example, a plutino with  $a_p \approx 39$  AU and  $e_p = 0.1$  will release a  $\beta = 0.3$  particle into an orbit with  $a_i = 82$  AU and  $e_i = 0.57$ . The 3:2 resonance with Neptune for this particle is located at  $a_{\text{res}} \approx 35$  AU. At that location, the grain will have  $e_f = 0.13$ .

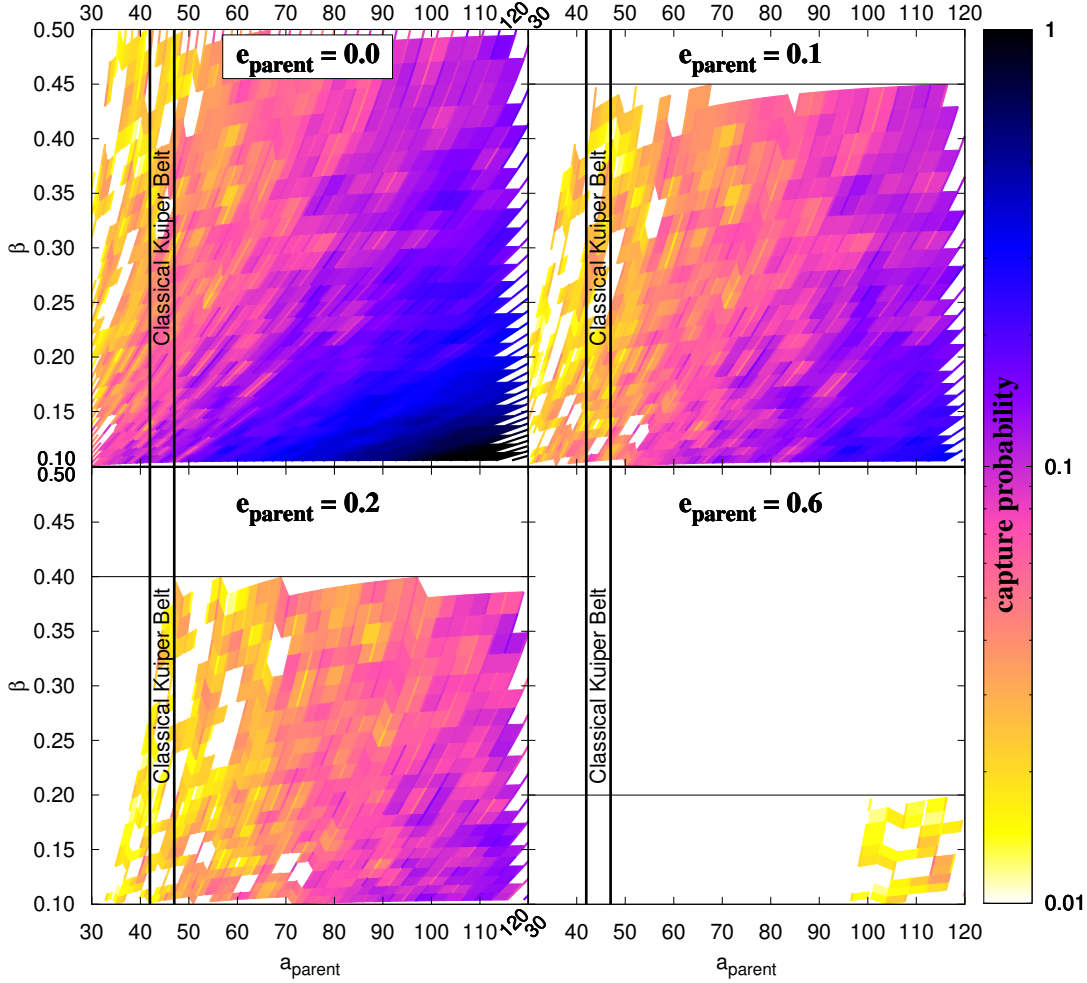


Figure 5.5.: Capture probability of a  $\beta$ -particle released by a parent body for the 3:2 resonance with Neptune.  $e_p = 0.6$  represents the population of scattered objects. Note that all particles above the horizontal lines have initial eccentricities of  $e > 1$  and will be removed from the system (Eq. 5.7).

With Eqs. 5.6 – 5.9 and the data of Mustill & Wyatt (2011) it is possible to calculate the capture probability for each resonance and particle size for given  $a_p$  and  $e_p$ . As a word of caution, we note that the actual dust dynamics can be more complicated. One complication is that the initial semimajor axis (Eq. 5.6) for sufficiently small particles is often so large that the grain has to pass several other resonances before it reaches the 3:2 one. At these resonances, particles with high migration rates and low eccentricities will

experience an eccentricity jump when they are not captured. As a result, our model will underestimate the final eccentricity at the 3:2 resonance and so overestimate the capture probability. Slow migration rates and low eccentricities will result in the opposite effect — an eccentricity decrease and a probability increase — so an underestimation of the capture probability is also possible (Mustill & Wyatt, 2011). A detailed modeling of this problem is beyond the scope of this work.

Fig. 5.5 shows the probability of capture into the 3:2 resonance with Neptune. The probability is the highest for  $e_p = 0$ , but even then it does not exceed  $\approx 20\%$  for dust grains below  $2 \mu\text{m}$  when released from classical EKBOs. Increasing the eccentricity of the EKBOs and decreasing the grain size reduces the capturing efficiency. For  $e_p = 0.6$ , which can be considered representative for scattered-disk objects, the capturing probability is only a few per cent. For  $e_p = 0.1$  (typical classical EKBOs) and  $s \sim 1 \mu\text{m}$  (slightly above the threshold of the New Horizons dust detector), the trapping probability is still below 10%. Given these results, we decided to neglect resonant capture.

### 5.3.2. Gravitational Scattering

Because P-R drag continuously decreases the particle's distance from the Sun, the grain will eventually reach the orbit of a planet. As this happens, the grain can either fall onto the planet, be scattered, or pass the planet without interaction. In the first two cases the particle will be lost. To determine the surviving fraction, we used a numerical code that calculates the orbital evolution of a single particle, taking into account the gravity of one planet and the P-R effect. The corresponding code *DISCO* (Direct Integration of Single Circumstellar Orbits) was first developed by Alexander Krivov, then advanced by Martin Reidemeister (Reidemeister, 2007). Further improvements to analyze the scattering rates and further development was done by the author of this thesis. For each  $\beta$ -value listed in Table 5.1 (these are the same values as used in our collisional simulations) we started 10 000 particles, with an EKB-like  $a, e, i$  distribution taken from the upper panel of Fig. 3.5. A particle was counted as a survivor as soon as its apocentric distance became shorter than the pericentric distance of the planet.

The results are listed in Table 5.1 for Neptune, Uranus and Saturn. As expected, the surviving rate decreases for larger grains with lower migration rates. Moro-Martín & Malhotra (2003) found quantitatively similar results in the scattering rates of Saturn<sup>22</sup>. For Neptune and Uranus the ejection rate is negligible and will not alter the dust flux

<sup>22</sup>Interestingly, they found that (except for Jupiter) the scattering rates increase with larger  $\beta$ -values.

significantly (Sec. 5.5). However, Saturn ejects nearly half of the dust grains. As we will see in Sec. 5.5, Saturn’s influence is important for the explanation of the in-situ measurements, but all three planets have little effect on the thermal emission of the EKB dust (Sec. 5.7).

Table 5.1.:  $\beta$ -values and corresponding sizes, masses and surviving rates for particles passing Neptune, Uranus and Saturn. Particles between  $10^{-12} \text{ g} < m < 10^{-9} \text{ g}$  can be measured by the New Horizons dust counter (Horányi et al., 2008).

$\beta$	$s$ [ $\mu\text{m}$ ]	$m$ [g]	$\Psi_{\text{surv}}$	$\hat{\delta}_{\text{surv}}$	$\hat{\eta}_{\text{surv}}$
0.404	0.65	$2.7 \times 10^{-12}$	96.8%	97.4%	79.7%
0.259	0.99	$9.5 \times 10^{-12}$	93.8%	95.1%	66.0%
0.164	1.5	$3.4 \times 10^{-11}$	88.7%	90.0%	57.0%
0.106	2.3	$1.2 \times 10^{-10}$	82.2%	80.1%	50.3%
0.070	3.5	$4.3 \times 10^{-10}$	78.3%	73.9%	47.1%

As shown in the previous section, the EKB dust disk is transport-dominated for small particles, which means that collisions play a minor role. Therefore, gravitational scattering can simply be implemented by multiplying the distribution obtained in the collisional simulation by the surviving rates for the corresponding particle sizes and distances.

## 5.4. Influence of Sublimation

When drifting inward, dust grains will not only suffer interaction with planets, but they will also be heated up because of the decreasing distance to the Sun. Our dust particles are composed of “dirty ice” (50% ice and 50% astrosilicate in volume). Their icy part sublimates at  $\approx 100 \text{ K}$  (Kobayashi et al., 2008, 2009, 2011). Since the EKB dust disk is radially optically thin, the temperature of a dust grain is determined by the energy balance between the absorption of incident Solar radiation and the thermal emission of the grain. We neglected the latent heat of sublimation because its contribution is minor (Kobayashi et al., 2008). The sublimation distance  $r_{\text{subl}}$ , where the temperature of a particle reaches 100 K, depends on its size. If the particles are larger than  $\lambda/(2\pi)$ , where  $\lambda$  is the peak wavelength of emission, the absorption and emission cross sections are approximately the same as the geometrical one, and these particles can be assumed to be blackbody radiators. For  $T = 100 \text{ K}$  the maximum emission is at  $\lambda \sim 30 \mu\text{m}$ , which corresponds to grains with  $s > 5 \mu\text{m}$ . Temperatures of smaller particles are obtained by solving the thermal balance equation (see, e.g., Krivov et al., 2008). Fig. 5.6 shows the resulting temperatures

for different sizes and distances, with three isotherms overplotted. The leftmost one corresponds to 100 K. Empirically we can approximate the dependence of the sublimation distance (in AU) on the size (in micrometers) by

$$r_{\text{subl}} = \begin{cases} -10.2 \sin(0.26s) + 16.85 & s \leq 5.0 \mu\text{m} \\ 8.0 & s > 5.0 \mu\text{m}. \end{cases} \quad (5.10)$$

We note that this function does not have a physical meaning and is only needed to implement sublimation into our model.

The outcome of sublimation depends on the structure of icy grains. If a single icy particle is an aggregate of small grains, each having  $\beta \geq 0.5$ , the resulting grains will be blown out and therefore no grains should be present inside  $r_{\text{subl}}$ . However, if the constituent monomers have  $\beta \leq 0.5$ , the number density of grains inside  $r_{\text{subl}}$  will increase. Since both possibilities are inconsistent with the dust flux measured by spacecraft, a single icy grain is likely to contain a single core of refractory material covered with an ice mantle (Kobayashi et al., 2010). For our dirty-ice grains sublimation will result in a 100% silicate particle that has half of the volume of the original particle. The radius of the resulting particle is simply

$$s_{\text{silicate}} = \sqrt[3]{0.5} s_{\text{icy}}, \quad (5.11)$$

and the mass is given by

$$m_{\text{silicate}} = 0.5 \frac{\rho_{\text{silicate}}}{\rho_{\text{icy}}} m_{\text{icy}}, \quad (5.12)$$

with  $\rho_{\text{icy}} = 2.35 \text{ g cm}^{-3}$  being the bulk density of the dirty ice and  $\rho_{\text{silicate}} = 3.35 \text{ g cm}^{-3}$  of the astrosilicate. The typical sizes and  $\beta$ -values of the particles before and after sublimation are given in Table 5.2 together with their sublimation distances.

We now discuss how sublimation affects the distribution of dust. The particles born through collisions in the Edgeworth-Kuiper belt have eccentricities roughly comparable to their  $\beta$ -values (Eq. 5.7). Although damped by P-R drag, their eccentricities in the sublimation zone are typically higher than 0.05. Particles with  $e > 0.05$  will experience a rapid sublimation without pile-up and dust ring formation (Kobayashi et al., 2009, see also Burns et al., 1979, their Fig. 8). Next, although sublimation in our model does not eliminate the particles and accordingly preserves their number, it reduces their spatial number density. This is because the number density of particles is inversely proportional to their drift rates in the steady-state. Because  $\dot{a} \propto \beta$ , the increase of  $\beta$  due to sublimation lessens the number density of particles. Based on Table 5.2, the change is estimated to be

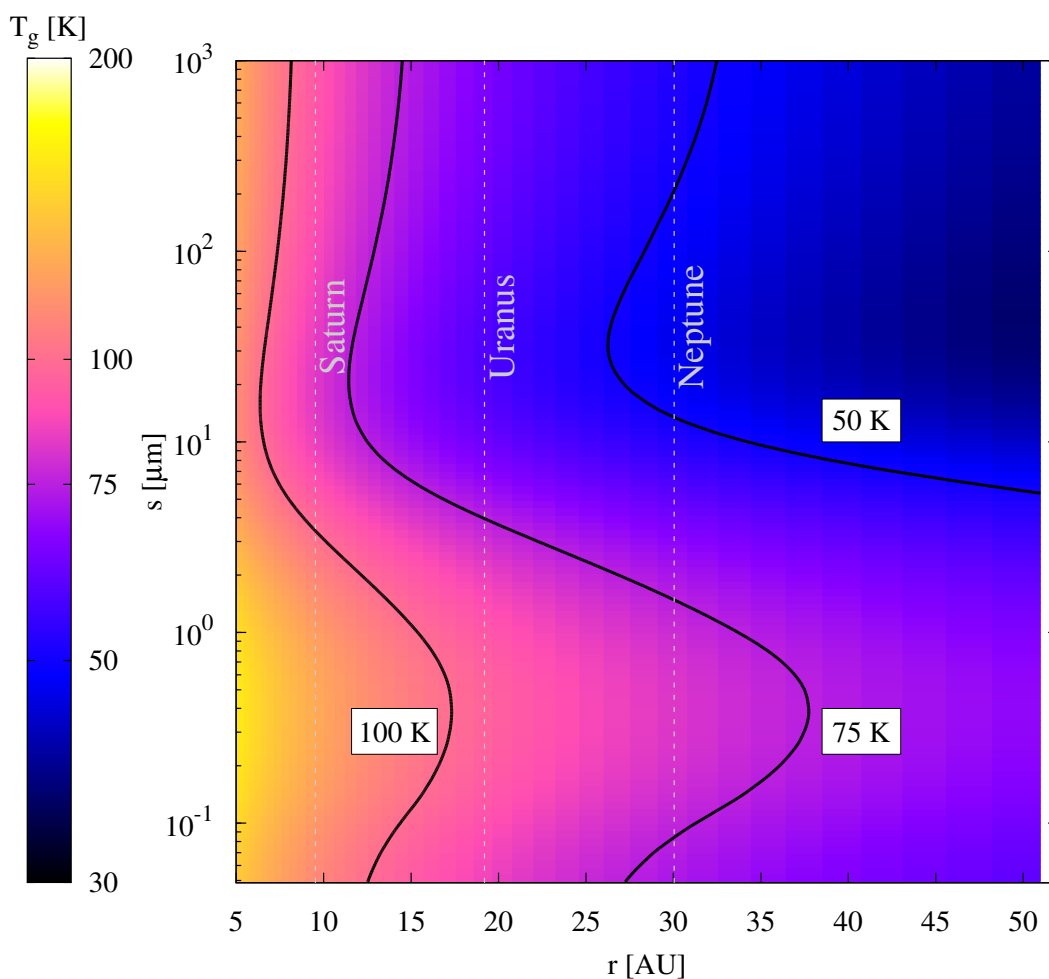


Figure 5.6.: Temperatures of the dirty-ice particles for different distances. The solid lines correspond to 100 K, 75 K and 50 K. Sublimation occurs at  $T_{\text{subl}} = 100$  K. Sublimation distance increases with decreasing size because the emission efficiency of small grains is lower, which makes them hotter.

only about 20%, see Fig. 5.7 below. However, with in-situ dust detectors measuring only grains above a certain threshold, the observable dust flux decreases more strongly.

If we assume that the orbital changes due to the change in size and therefore changing interaction with the stellar radiation are small, we can implement sublimation into our collisional results the same way as gravitational scattering by simply correcting sizes and cross-section- and mass density for the affected bins. Since planetary scattering and sublimation are independent processes, the order of implementation does not matter.

Table 5.2.: Sizes and  $\beta$ -values before and after sublimation and the corresponding sublimation distances; for particles larger than  $5.0 \mu\text{m}$  blackbody temperatures are assumed.

$s_{\text{icy}} [\mu\text{m}]$	$\beta_{\text{icy}}$	$r_{\text{subl}} [\text{AU}]$	$s_{\text{silicate}} [\mu\text{m}]$	$\beta_{\text{silicate}}$
0.425	0.576	15.7	0.337	0.652
0.648	0.404	15.1	0.514	0.428
0.989	0.259	14.3	0.785	0.280
1.51	0.164	13.0	1.20	0.184
2.30	0.070	11.1	1.83	0.121
3.51	0.046	8.8	2.79	0.079
> 5.0		8.0	$\sqrt[3]{0.5} s_{\text{icy}}$	

## 5.5. Comparison with Spacecraft Measurements

The Student Dust Counter on-board the New Horizons spacecraft is capable of detecting impacts of grains with  $10^{-12} \text{ g} < m < 10^{-9} \text{ g}$  and can distinguish grain masses apart by a factor of 2 between  $0.5 \mu\text{m} < s < 5 \mu\text{m}$  (Horányi et al., 2008). The first results from Poppe et al. (2010) indicate particle fluxes of up to  $1.56 \times 10^{-4} \text{ m}^{-2} \text{ s}^{-1}$ . The results of Han et al. (2011) show a slight increase of the flux for  $r > 15 \text{ AU}$ . The particle flux can be calculated via

$$F_{\text{dust}}^{\text{p}} = \int mnv_{\text{rel}} d(\ln m), \quad (5.13)$$

with  $m$  being the mass of the particle,  $n$  the number density per logarithmic mass and  $v_{\text{rel}}$  the relative velocity between the spacecraft and the particle. The first two values are a direct output of our simulation. The relative velocity was assumed to be  $v_{\text{rel}} = 15.54 \text{ km s}^{-1}$ , according to the official New Horizons web page<sup>23</sup>. Based on the previous results, we calculated the dust fluxes for the EKB dust disk unaffected by planets and sublimation, the one with planets and the one with planets and sublimation. Although the separate contributions of planets and sublimation are rather low, their combination can alter the dust flux by up to a factor of three, in which Saturn plays the most important role. In Fig. 5.7 the results of run “f” are shown. The proper evolutionary state of the simulation (i.e. timestep) was chosen in the following way. As seen in Fig. 5.7, the black solid line can be assumed to be a constant for  $r < 20 \text{ AU}$ . With this assumption we fitted the New Horizons data from Poppe et al. (2010) and Han et al. (2011) by a constant line to  $F_{\text{dust}}^{\text{p}} \approx 3 \times 10^{-4} \text{ m}^{-2} \text{ s}^{-1}$  and searched for the timestep that agrees with the model best.

<sup>23</sup>[http://pluto.jhuapl.edu/mission/whereis\\_nh.php](http://pluto.jhuapl.edu/mission/whereis_nh.php) (Last accessed on 2 September 2011)

According to Gurnett et al. (1997), the Voyager 1 and 2 plasma wave instruments, which acted as “chance” dust detectors, have a mass threshold of  $m > 1.2 \times 10^{-11}$  g, which is one order of magnitude higher than for the New Horizons dust counter. Accordingly, we rescaled the Voyager data to the New Horizons threshold, with the power law slope of  $q = -1$  obtained in our simulation for the corresponding masses (Fig. 5.1) at 40 AU. Because the instruments aboard Voyager I and II were neither designed to detect dust impacts nor calibrated for this purpose and traversed the outer Solar System in highly inclined orbits, their dust measurements should be compared with our model with great caution.

Simulations f, f<sub>CKB</sub>, and n were treated the same way. Since for the particle sizes in question ( $s < 5 \mu\text{m}$ ) all modeled disks are transport-dominated, the results do not differ much from each other and lead approximately to the same fits as for the “f” run. Therefore these results are not shown.

## 5.6. Consistency Check with the Nice Model

As recent planet formation models suggest (see Sec. 1.2) planetesimals are born big up to 10...1000 km in radius. As a consequence smaller objects are underabundant leading to a break in the size distribution at several tens of kilometers (cf. previous Sections in this Chapter). In simulations of the Nice model a set of initial parameters for the compact Kuiper belt is found to be  $a = 17 \dots 35$  AU,  $M_{\text{disk}} = 35M_{\oplus}$  (see, for a recent review, Morbidelli et al., 2009, and references therein). With this conditions and the additional assumptions of an eccentricity distribution between  $0.0 < e < 0.2$  and a semi-opening angle of the disk of  $i \approx 8^\circ$  we started another ACE runs with the mentioned parameters. As parent bodies we used objects between 30...370 km and 63...370 km in size. The latter distribution is approximately the same as in the “n” run. After 800 Myr of simulation time the integration was stopped, according to the start of the LHB. Equations 2.60 and 2.59 show that amplifying the initial disk mass and reducing the distance of the belt will speed up the collisional evolution. The question is whether collisional lifetimes are shortened enough to allow even the largest parent bodies to get into a collisional equilibrium which would be in contrast to the break we found. The results are shown in Fig. 5.8.

The break in the size distribution is still present after 800 Myr even with that compact and massive configuration described above. The depth of the drop of the cross section is in a good agreement with our “f” and “n” run. A difference between the “f” run and the others is the missing local maximum at  $\sim 1$  km. Since the critical disruption energy

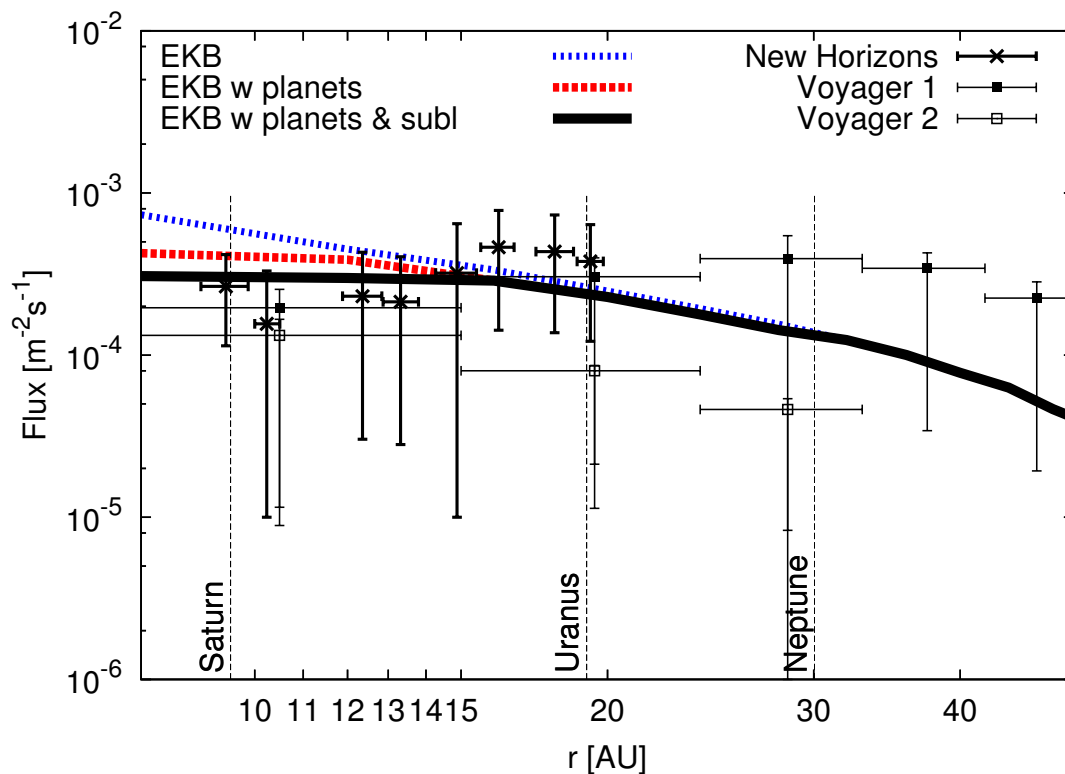


Figure 5.7.: Simulated particle flux compared with in-situ measurements by New Horizons and Voyager 1 and 2. The solid black line takes into account planets and sublimation and represents our best fit to the data taken from Poppe et al. (2010), Han et al. (2011), and Gurnett et al. (1997). The dotted and dashed lines show the dust flux for the unperturbed EKB and after planetary scattering without sublimation, respectively.

has a minimum at  $\approx 100$  m, these objects are destroyed the easiest and therefore are underabundant. Due to this, they cannot act as projectiles for kilometer-sized objects which results in this maximum. In the “f” run the flat slope between  $10 \text{ m} \lesssim s \lesssim 10 \text{ km}$  is a remnant of the extrapolation, and since these objects are not yet part of the collisional cascade, the slope remains unchanged.

A mean collisional lifetime of 800 Myr is found for objects  $s \approx 10 \text{ km}$ , which is approximately the break-size. Therefore, we can conclude that objects smaller than  $s < 10 \text{ km}$  were in a collisional equilibrium before the LHB and  $s > 10 \text{ km}$  sized objects are still primordial. If this is true there should be a slight overabundance of kilometer-sized objects.



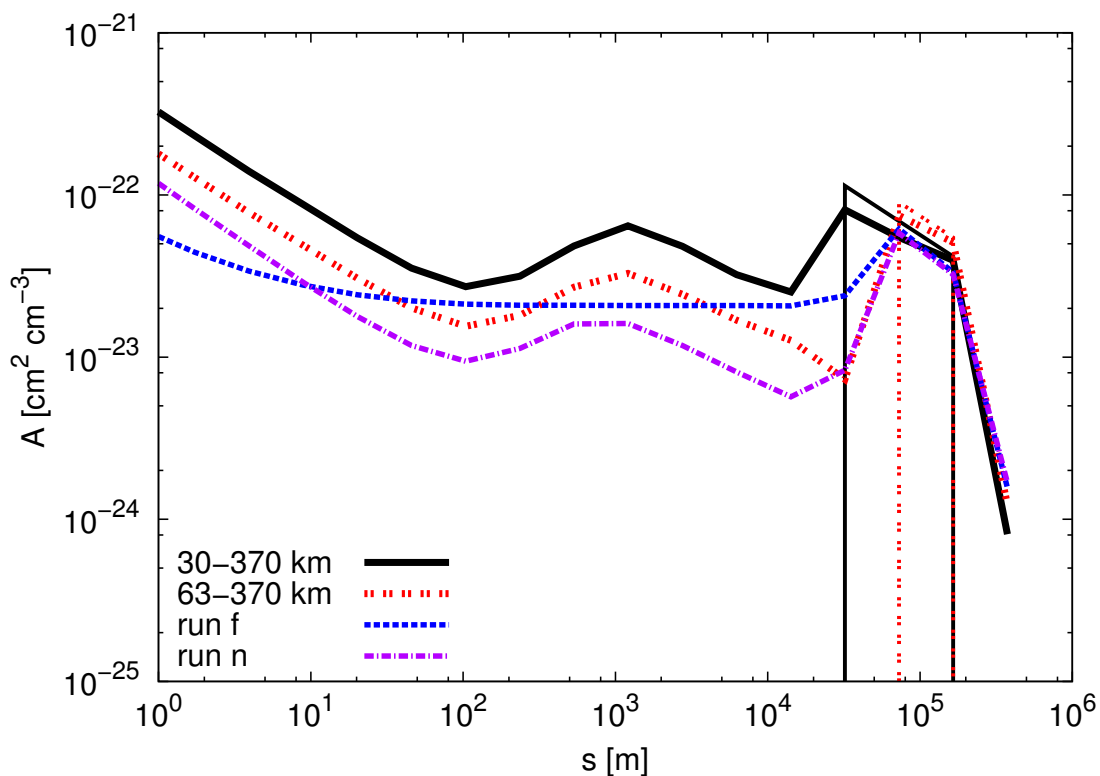


Figure 5.8.: Size distribution of a compact EKB after 800 Myr. The thin lines mark the initial conditions as written in the text. The results of run “f” and “n” are shown for comparison and amplified by a factor of 1000.

## 5.7. Thermal Emission Constraints

### 5.7.1. Spectral Energy Distribution

To calculate the thermal emission of dust in the EKB, we computed the photospheric spectrum of the Sun using the NextGen models (Hauschildt et al., 1999). The equilibrium dust temperatures were obtained by the procedure of Krivov et al. (2008). As in the collisional simulations, we adopted the “dirty ice” consisting of equal volume fractions of ice (Warren, 1984) and astrosilicate (Laor & Draine, 1993). As explained in Sec. 5.4, the sublimation distance depends on the particle size. Therefore we divided the EKB into six sub-rings to handle the different emission properties of the dirty ice and pure astrosilicate (Table 5.3).

To place our EKB in the context of extrasolar debris disks, we now consider the EKB dust disk as if it were viewed from outside. The final spectral energy distribution (SED)

Table 5.3.: The EKB divided into six sub-rings: material composition together with the sizes and distances for which that composition was adopted.

ring #	material	$s$ [ $\mu\text{m}$ ]	distance [AU]
1	astrosilicate	$0.425 < s < \infty$	$0 < r < 8$
2	dirty ice	$3.51 < s < \infty$	$8 \leq r < 12$
3	astrosilicate	$0.425 < s \leq 3.51$	$8 \leq r < 12$
4	dirty ice	$1.51 < s < \infty$	$12 \leq r < 16$
5	astrosilicate	$0.425 < s \leq 1.51$	$12 \leq r < 16$
6	dirty ice	$0.425 < s < \infty$	$16 \leq r < \infty$

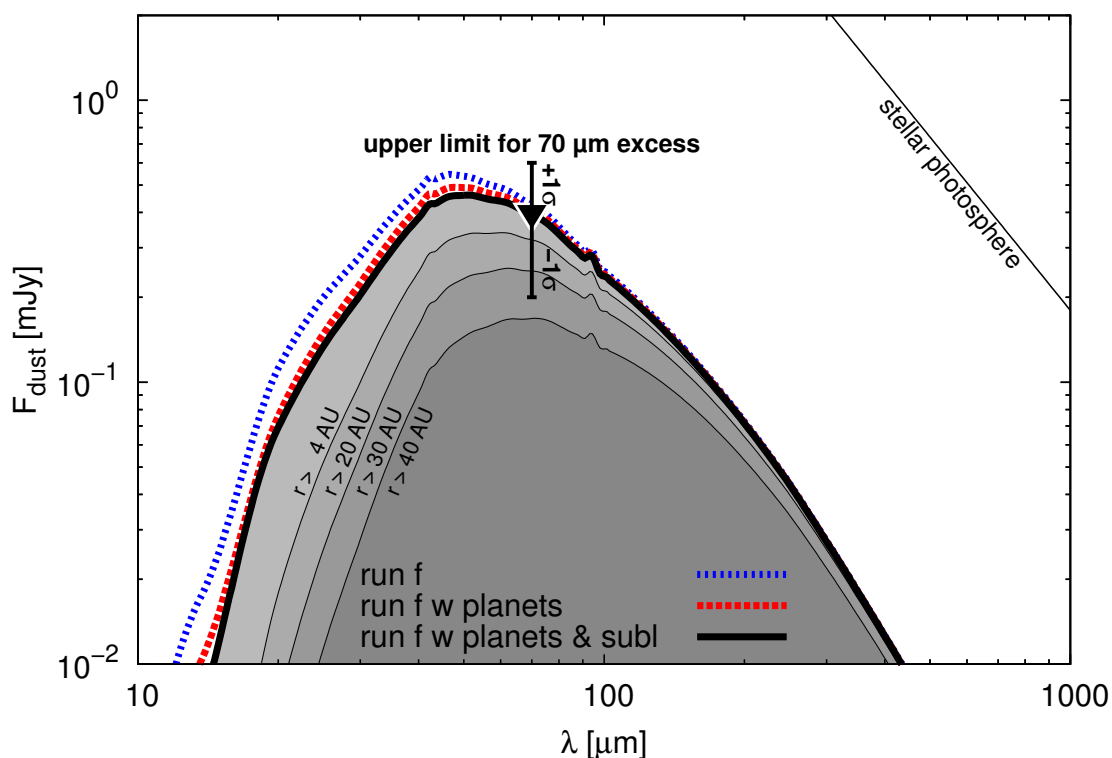


Figure 5.9.: Spectral energy distribution of the EKB including planets and sublimation (solid black line), with planets (dashed red line), and for an unperturbed EKB (dotted blue line). All curves are based on the same run (“f”) and the same time instant as in Fig. 5.7. Different gray shaded areas show the contribution to the flux of different distances.

of the EKB dust disk, as seen from a reference distance of 10 pc, is shown in Fig. 5.9. The influence of planets and sublimation does not significantly alter the shape, peak position, and height. The SED, corrected for planets and sublimation, peaks at 40 – 50  $\mu\text{m}$

with a maximum thermal emission flux of  $\approx 0.5$  mJy, which amounts to  $\approx 0.5\%$  of the photospheric flux at that wavelength. The predicted flux drops to  $\approx 0.4$  mJy at  $70\ \mu\text{m}$  and to  $\approx 0.2$  mJy at  $100\ \mu\text{m}$ . The fractional luminosity of the modeled EKB dust disk, after applying corrections for planets and sublimation, is  $f_d = 1.2 \times 10^{-7}$ .

Our results are consistent with the upper limit that is placed by non-detection of the EKB dust emission at  $70\ \mu\text{m}$  with the COBE spacecraft. That limit amounts to  $1 \pm 0.5\%$  of the Solar photospheric flux (Greaves & Wyatt, 2010) and is shown by the triangle in Fig. 5.9.

### 5.7.2. Surface Brightness Synthetic Images

Figure 5.10 shows the radial brightness profile and a synthetic surface brightness image for the “f” run at  $70\ \mu\text{m}$  without planets and sublimation, with planets, and with planets and sublimation. For other wavelengths (Fig. 5.11) the radial brightness profiles are not shown because they show qualitatively the same results. As already seen and discussed for the SED, planets and sublimation only alter the inner part of the Solar System.

Kuchner & Stark (2010) addressed the same problem of predicting the EKB dust disk properties and employed a catalog of known EKBOs to model the dust production. Instead of collisional grinding simulations, Kuchner & Stark made use of N-body integrations supplemented with a “collisional grooming” algorithm. Despite the difference in the simulation methods, their results for the radial distribution of the EKB dust are in a qualitatively good agreement with ours (cf. our Fig. 5.2 and their Fig. 4). Their surface brightness images show qualitatively the same results. Since they included planets directly into their simulations, they are able to reveal the captured particles of first order resonances (their Fig. 8). Consequently, these brightness maxima are missing in our results. Although the total numbers cannot be compared, because they did not calibrate their model to dust impact rates, their model show a concentration of small grains inside 20 AU as well as the model presented in this thesis does. The same holds for the  $800\ \mu\text{m}$  image (their Fig. 9, Fig. 5.11 in this thesis) which is not a surprise. The  $800\ \mu\text{m}$  flux is mainly determined by larger grains, which are nearly unaffected by stellar radiation and drag forces and therefore stay in the birth ring.

The effect of transport mechanisms can also be seen in Fig. 5.11. As the wavelength of observations increases, the contribution of larger particles to the observed flux increases. In other words, small particles contribute most to the  $70\ \mu\text{m}$  image, whereas larger grains contribute most to the  $160\ \mu\text{m}$  and  $800\ \mu\text{m}$  image. This explains why the  $70\ \mu\text{m}$  image reveals its maximum in the inner part of the Solar System, because P-R drag transports

small particles inward. In contrast to this, the P-R effect is inefficient for large grains, leading to a “hole” in the brightness profile in the inner part.

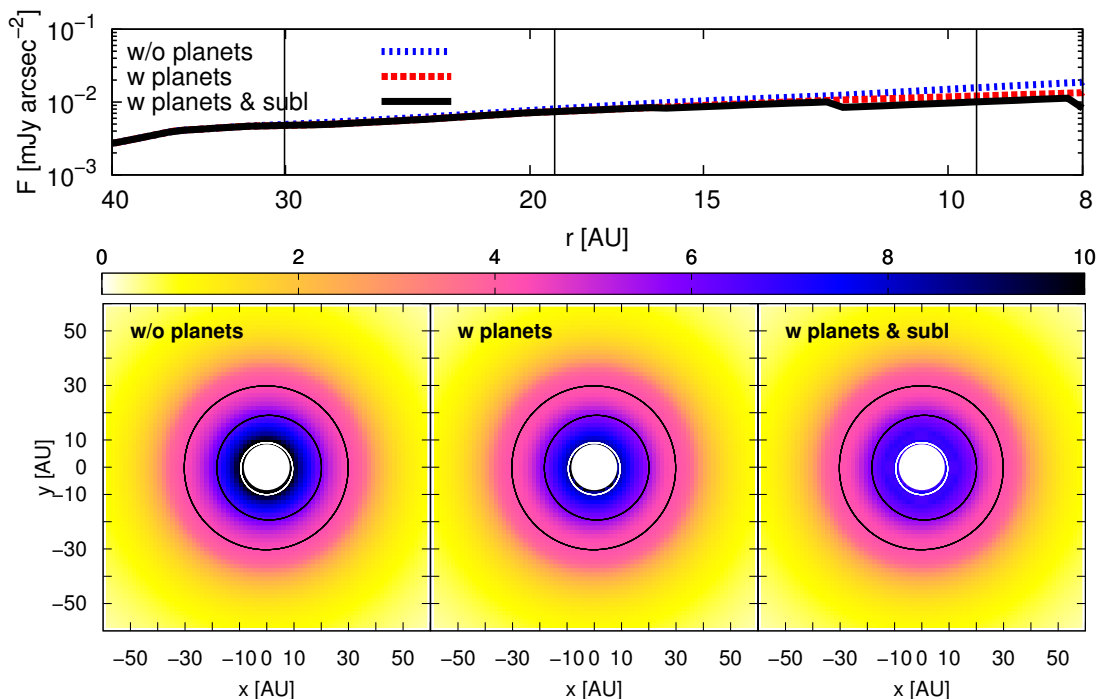


Figure 5.10.: Radial profile (upper panel) and surface brightness images (lower panel) of the EKB at  $70\mu\text{m}$  without planets and sublimation, with planets, and with planets and sublimation. The fluxes are given in  $\mu\text{Jy arcsec}^{-2}$ . The lines/ellipses show the orbit of Neptune, Uranus and Saturn (from outside in).

### 5.7.3. Detectability of the Kuiper Belt

Would (exact) EKB analogs around nearby stars be detectable, for example, with the PACS instrument (Poglitsch et al., 2010) of the Herschel Space Observatory (Pilbratt et al., 2010)? The sensitivity of the PACS instrument at  $70\mu\text{m}$  is  $4.7\text{ mJy}$  in 1 hour integration time at a  $5\sigma$  uncertainty level<sup>24</sup>. This is about a factor of 10 above the calculated SED flux of  $0.4\text{ mJy}$  at  $70\mu\text{m}$ . This factor would increase even more when taking into account additional background noise and photospheric flux uncertainties. We conclude

<sup>24</sup><http://herschel.esac.esa.int/Docs/PACS/html/ch03s05.html#sec-photo-sensitivity>  
(Last accessed on 02 April 2012)

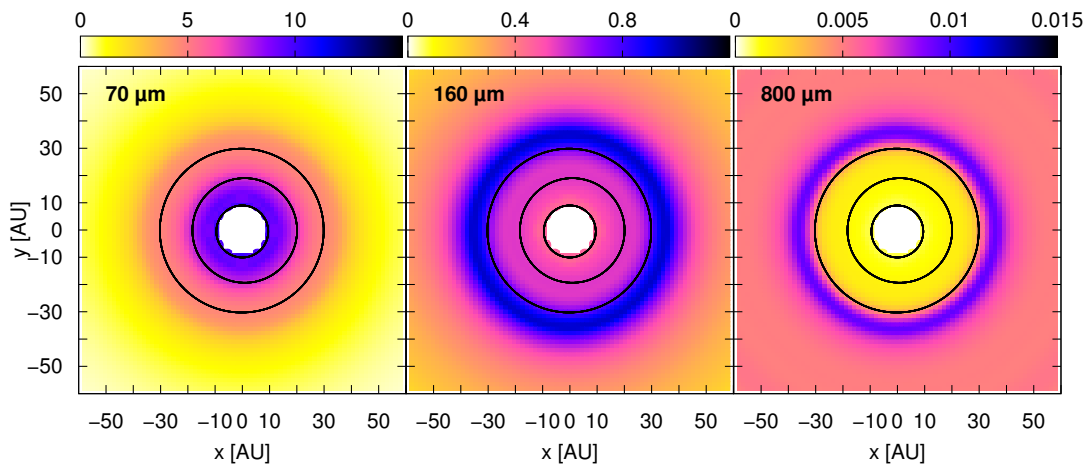


Figure 5.11.: Surface brightness images of the EKB after planetary interaction and sublimation at  $70 \mu\text{m}$ ,  $160 \mu\text{m}$  and  $800 \mu\text{m}$ . The fluxes are given in  $\mu\text{Jy arcsec}^{-2}$ . The ellipses show the orbit of Neptune, Uranus and Saturn (from outside in).

that the detection of an exact analog of the EKB with the present-day instruments is impossible.

## 6. Summary and Outlook

“We are all agreed that your theory is crazy. The question that divides us is whether it is crazy enough to have a chance of being correct.”

---

Niels Bohr (1885-1962)

The goal of this thesis was to construct a model of the Solar System’s cold debris disk — Kuiper belt objects and their collisional debris. This was done in two major steps. First, a new algorithm to remove the two largest selection effects from TNO observations, the inclination and the distance biases was developed. Applying it to the database of 1260 known TNOs, we derived new estimates for the global parameters of the “true” Kuiper belt: its mass, orbital and size distribution. Second, treating the debiased populations of EKB objects as dust parent bodies, the collisional code *ACE* was employed to simulate their dust disk. In our first modeling effort, we made an in-depth analysis of the influence of the Poynting-Robertson drag and the increased mass of the belt of parent bodies on the radial and size distribution. This model, however, was rejected for being inconsistent with the COBE upper non-detection limit. We could exclude that the EKB is in a collisional equilibrium throughout all sizes. Dropping the assumption of collisional equilibrium resulted in a self-consistent model of the EKB dust disk, consistent with dust impact measurements and not violating the COBE limit. In addition, the thermal emission of the Kuiper belt dust was calculated. The main results are summarized below.

### 6.1. Kuiper Belt Objects

1. The total mass of the EKB, including classical, resonant, and scattered objects, amounts to  $0.12M_{\oplus}$  for an assumed mean bulk density of  $\varrho = 1 \text{ g cm}^{-3}$ . Without scattered objects, the mass reduces to  $0.05M_{\oplus}$  ( $\varrho = 1 \text{ g cm}^{-3}$ ). These values are about one order of magnitude higher than the mass of the known TNOs. The mass ratio between the classical, resonant and scattered objects is 1 : 0.2 : 1.3.
2. In terms of inclination, the classical Kuiper belt consists of a cold ( $i \sim 0^{\circ} \dots 5^{\circ}$ ) and a hot ( $i \sim 20^{\circ} \dots 25^{\circ}$ ) subpopulation. In terms of eccentricity, the scattered objects

consist of a hot ( $e \sim 0.5 \dots 0.7$ ) and a very hot ( $e \sim 0.8 \dots 0.9$ ) subpopulation. The last result, however, should be taken with caution, since the debiasing algorithm is less accurate for scattered objects.

3. The slope of the differential size distribution in the EKB in the size range  $50 \text{ km} < s < 170 \text{ km}$  (absolute magnitudes  $8.9 > H > 6$ ) is found to be  $q = 4.3 \pm 0.2$  for the classical objects,  $5.1 \pm 0.1$  for resonant ones, and  $2.8 \pm 0.1$  for scattered TNOs. This results in  $4.4 \pm 0.2$  for classical and all resonant objects together. For the entire EKB (classical, resonant, and scattered TNOs), we find  $3.6 \pm 0.1$ .

Although it is believed that the debiasing algorithm presented in this work is more accurate than the ones used before, it is possible that the results over- or underestimate, for instance, the mass of the EKB by a factor of a few. The main reason is an incomplete list of surveys used for debiasing. In particular, observations that covered higher ecliptic latitudes, omitted in Table 3.1, could alter the results. 90 objects in the MPC (excluding Centaurs) were identified that have been detected beyond  $10^\circ$  ecliptic latitude. Of these, 29 objects have been found beyond  $20^\circ$ . To check how non-including the surveys that covered higher latitudes may affect the results, additional tests were made. A re-run of our code was done several times, each time artificially changing  $\varepsilon$  in three randomly chosen surveys of Tab. 3.1 to  $20^\circ$ . This changed the detection probability of single objects typically by a few tenths of percent only. The change in the inferred total EKB mass turned out to be larger, but still minor, 4%.

Another difficulty is related to the scattered objects with their large eccentricities and inclinations. Their average detection probability is very low, the resulting “mass amplification factor” very high ( $\approx 25$ ), so that the estimated masses of objects can considerably differ from the “true” ones. The same applies to the treatment of the smallest objects discovered so far, a few kilometers in radius.

## 6.2. Model of the Kuiper Belt in Collisional Equilibrium

Although the model obtained in Chapter 4 fails to reproduce the actual EKB, the results show the inevitable coupling of the radial and size distribution of dust. However, we cannot rule out this modeling attempt from the beginning since we do not know whether a break in the size distribution is common in other debris disks. Hence, the results could still be valid for extrasolar EKB analogs. In addition, the effect of increased parent body

mass and transport effects were analysed in depth and therefore the results of Chapter 4 are summarized here.

1. If the debiased populations of TNOs are taken as dust sources and an extrapolation toward small sizes according to O'Brien & Greenberg (2003) is made (i.e. that objects throughout all sizes are in collisional equilibrium), the dustiness of the disk will be high enough to make collisional timescales comparable to, or even shorter than, the radial transport timescales. Thus such a predicted Kuiper belt dust disk rather falls to the category of collision-dominated debris disks, to which all debris disks detected so far around other stars belong, albeit it is already close to the "boundary" between collision-dominated and transport-dominated disks. For such an EKB, the simulated size distribution shows a sharp cutoff at the radiation pressure blowout radius of  $\sim 1 \mu\text{m}$ . The cross section dominating radius is several times larger.
2. As a comparison, also a dust disk that would be produced solely by known TNOs as parent bodies was considered using the same extrapolation toward small sizes as before. That disk would fall into the transport-dominated regime, where the Poynting-Robertson drift timescales are shorter than the collisional timescales (at dust sizes). The size distribution in such a disk is dramatically different from the one expected in collision-dominated disks. While a cutoff at  $1 \mu\text{m}$  remains, the distribution between  $1 \mu\text{m}$  and several hundreds of  $\mu\text{m}$  is nearly flat, and the cross section is now dominated by much larger grains,  $\sim 100 \mu\text{m}$  in radius.
3. The radial distribution of the TNOs themselves peaks in the region of the main belt (40...50 AU), where about 90% of the cross section comes from the classical EKB objects. Outside  $\sim 60$  AU, the cross section is solely due to scattered objects. The distribution of the latter is quite extended radially, being nearly flat over a wide distance range from  $\approx 35$  AU to more than 100 AU.
4. The radial distribution of dust grains with radii  $\geq 10 \mu\text{m}$  is similar to the distribution of the parent bodies described above (assuming collisional equilibrium up to largest TNOs). At smaller sizes, the radial profile gets progressively broader with decreasing radius, which is a classical effect of radiation pressure.
5. The maximum normal geometrical optical depth is reached at the inner edge of the classical belt,  $\approx 40$  AU, and is estimated to be  $\approx 6 \times 10^{-6}$ . Outside that distance, it falls off as  $r^{-2}$ . This slope is roughly intermediate between the slope predicted



analytically for collision-dominated ( $r^{-1.5}$ ) and transport-dominated ( $r^{-2.5}$ ) disks. An upper limit of the in-plane optical depth is set to  $\approx 2 \times 10^{-5}$  outside 30 AU. The dust production rate is calculated to  $\lesssim 1.7 \times 10^8 \text{ g s}^{-1}$ . Note that these results were obtained assuming collisional equilibrium throughout all sizes.

6. For comparison, the normal optical depth of the dust disk produced only by known TNOs would fall off outside the classical EKB as  $\tau \propto r^{-3}$ , and the in-plane optical depth would be by two orders of magnitude lower. Note again that these results were obtained assuming collisional equilibrium throughout all sizes.
  
7. The estimated thermal emission flux from the EKB dust disk (for the modeling attempt used in Chapter 4) that would be observed from a 10 pc distance strongly depends on the assumed dust composition. For two “realistic” materials probed, ice and ice-silicate mixture (“dirty ice”), the SED would peak at 40 . . . 60  $\mu\text{m}$ . The maximum value is at a level of several mJy (the Solar photospheric flux at the same wavelengths is several tens of mJy), which is about two orders of magnitude smaller than for the brightest known debris disks around other solar-type stars, normalized to the same distance. For a non-debiased EKB, the fluxes would be another two orders of magnitude lower.
  
8. With the Herschel Space Observatory, it would be possible to detect debris disks around other stars, which are within a factor of a few times the brightness of the EKB dust disk, if it were in a collisional equilibrium. For observations with the PACS instrument at 100  $\mu\text{m}$  in a scan-map mode with one hour exposure, assuming an average background noise, the minimum mass of a Kuiper belt detectable at  $5\sigma$  from 10 pc is estimated as  $\approx 1 \dots 2M_{\text{EKB}}$ .

The results obtained in the modeling shows that it is not possible or advisable to treat the radial and size distribution independently since they are intrinsically coupled.

### 6.3. An Improved Model of the Edgeworth-Kuiper Debris Disk

1. We have shown that sub-kilometer-sized EKBOs largely determine the amount and distribution of dust in the outer Solar System. However, these are far too small to be directly detected at present in TNO surveys, and their properties cannot be accessed by collisional modeling, because they are not in a collisional equilibrium. Therefore, an extrapolation from observable TNOs toward smaller sizes is necessary.
2. A straightforward extrapolation for the as yet unknown objects ( $s \lesssim 10$  km) with a classical Dohnanyi law can be ruled out. In that case, the amount of dust would be so large that its thermal emission would have been detected by the COBE spacecraft. Therefore, the distribution of these objects should be flatter. In other words, a break in the size distribution at several tens of kilometers *has* to be present. We have shown that a compact and massive prehistoric EKB, were the TNOs were born big, as suggested by the Nice model is not in contradiction with this result. The break is retained.
3. Different extrapolation methods that are consistent with the measurements reveal the EKB either as a transport-dominated debris disk or to be intermediate between the collision-dominated and transport-dominated regimes. Depending on the extrapolation method, we found the present-day EKB to be in collisional equilibrium for objects  $s < 10 \dots 60$  m.

Since little is known about EKBOs smaller than a few tens of kilometers, but these largely control the amount and distribution of dust in the outer Solar System, an extrapolation from observable TNOs towards smaller sizes seems to be necessary. The question is what kind of extrapolation is reasonable. If the parent bodies pass on their orbital elements to their children and grand-children, then the EKB should comprise a huge amount of meter- and sub-kilometer-sized objects in highly eccentric orbits, stemming from scattered EKBOs. This would make collisions more disruptive and alter the size distribution of dust. The resulting size distribution would be dominated by the smallest dust grains, just above the radiation pressure blowout limit. If, in contrast, the meter- and sub-kilometer-sized objects have moderate eccentricities, the peak of the cross section in the size distribution would be broader and shifted to larger grains. To distinguish between these possibilities, one needs more information about the amount and distribution of sub-kilometer objects. Accurate measurements of sizes and orbital elements of dust grains in

the outer Solar System in the future would also help. What is for sure is a break in the size distribution at tens of kilometers, as reported in the recent literature, is necessary. Otherwise the EKB dust disk would be too dusty, violating the available observational constraints. If such a break is present in other debris disks as well, then the total mass of parent bodies should be higher than usually inferred in the debris disks studies.

We also showed that the pure knowledge of a parent body ring is not enough to model a unique dust distribution. This result is also true the other way around. In other words, with models of the dust properties and distribution from SEDs or resolved images there exist several models of parent body distributions which can explain the measurements. E.g., with a break in the size distribution the total mass of the dust-producing planetesimal belt might be underestimated in previous studies. We conclude that the link between parent bodies and dust (and vice versa) is not unambiguous.

Another question is whether the interaction of the Kuiper belt and the main belt dust should be considered. If in a mutual collision of two main belt parent bodies with  $e_p = 0$  a particle of, e.g.,  $\beta = 0.45$  is produced, then its apocenter is  $r = 25$  AU. There, it can collide with Kuiper belt dust. First, the main belt's mass ( $M_{\text{main belt}} \lesssim 0.04M_{\text{Moon}}$ ) is significantly lower than the EKB's. Second, the main belt is inside the orbit of Jupiter, i.e. the produced dust grains have to pass its orbit before there is any chance of interaction with EKB dust. A simulation similar to what was done in Sec. 5.3.2 but for the main belt and  $\beta = 0.4$  showed that  $\sim 70\%$  of the particles are scattered out of the system within  $\sim 100\,000$  yr by Jupiter (whereas none of the  $10\,000$  particles survived longer than  $350\,000$  yr). Although further in-depth investigations have to be done the neglect of the main belt seems justified.

4. Using the results of Mustill & Wyatt (2011), we estimated the effect of resonance trapping of planets. The capturing rate of the dust grains that are either detectable with in-situ measurements by spacecraft or contribute to measurable thermal emission turned out to be  $< 10\%$  in most cases and not to exceed  $< 20\%$  even for the largest grains considered. Accordingly, resonance trapping should have a negligible effect on dust impact rates and dust thermal emission, given the typical accuracy of the dust measurements.
5. Gravitational scattering of dust grains by planets was investigated numerically. Scattering can modify the particle flux in the Saturn-Uranus region ( $8\text{ AU} < r < 15\text{ AU}$ ) by about a factor of two and has little effect on the thermal emission of dust.

6. Likewise, sublimation can reduce the particle flux by approximately a factor of two and does not affect the thermal emission fluxes perceptibly.

Sufficiently large grains that derive from resonant TNOs must stay locked in such resonances from the very beginning for considerable time periods (e.g., Wyatt, 2006; Krivov et al., 2007). This will cause an enhancement of dust density at resonance locations, which was not modeled here. Furthermore, the distribution of dust will exhibit azimuthal clumps instead of being rotationally-symmetric, as was assumed in our *ACE* simulations. Although we estimated the capture probability into resonances to be small, Neptune is expected to capture at least some grains stemming from non-resonant KBOs which can alter the results (e.g., Liou & Zook, 1999; Moro-Martín & Malhotra, 2002).

Nevertheless, the amount of objects in mean-motion resonances is small compared to the amount of classical TNOs and therefore the changes in, e.g., the surface brightness images are probably negligible.

Next, if planetary scattering and/or sublimation is more efficient than assumed in our model, the amount of dust grains that reach the Saturn-Uranus region of the Solar System would be smaller. To stay consistent with the in-situ measurements, one would have to compensate higher scattering rates and/or more efficient sublimation by higher dust production rates in the EKB. However, this would lead to a higher thermal emission flux, which would contradict the non-detection of thermal emission by COBE. Therefore, it is most likely that the efficiency of scattering and/or sublimation was not underestimated substantially.

7. We calibrated our model with the in-situ measurements of the New Horizons dust counter (Poppe et al., 2010; Han et al., 2011) by fitting our results to the data points and can reproduce the nearly constant particle flux of  $3 \times 10^{-4} \text{ m}^{-2} \text{ s}^{-1}$ . The corresponding production rate of dust inside the EKB amounts to  $2 \times 10^6 \text{ g s}^{-1}$ , consistent with previous estimates (e.g., Yamamoto & Mukai, 1998a; Landgraf et al., 2002; Han et al., 2011). In a steady-state collisional cascade (which we assume), the “dust production rate” is the same as the “dust loss rate”. Consequently, the result means that 2 tons of dust per second leave the system by inward transport and through ejection as blowout grains.
8. The spectral energy distribution of an EKB analog, seen from a distance of 10 pc, would peak at  $40 \dots 50 \mu\text{m}$  with a maximum flux of 0.5 mJy. This is consistent with the upper limit that is placed by non-detection of thermal emission from the EKB dust as it would be viewed from outside at  $70 \mu\text{m}$  by the COBE spacecraft.

The fractional luminosity of the EKB was calculated to be  $f_d = 1.2 \times 10^{-7}$ . The normal optical depth is nearly constant inside the main belt and is estimated to be  $\sim 10^{-7}$ . The in-plane optical depth for  $r > 10$  AU is set by our model to  $2 \times 10^{-6}$ . Although the Herschel/PACS instrument successfully detects debris disks at similar fractional luminosity levels as the EKB (Eiroa et al., 2010, 2011), these are all larger and therefore colder. Their thermal emission peaks at wavelengths longward of  $100 \mu\text{m}$ , where the stellar photosphere is dimmer. The detection of an exact EKB analog even with PACS would not be possible.

When calculating the thermal emission of dust in Sec. 4.3.1, it was shown that the results are sensitive to the adopted absorption and emission efficiencies of grains. There are no reasons to think that variation of other parameters, for instance mechanical properties of different-sized solids in the collisional modeling, would alter the results to a lesser extent (see, e.g., explanatory note in Sec. 6.4, Grain Shape and Composition).

## 6.4. Future Work

Realistic simulations would necessitate good knowledge of tens of parameters, such as the bulk density, porosity, shape, tensile strength, optical constants of solids in the EKB, and all this over an extremely broad range of sizes: from hundreds of kilometers (large TNOs) down to a fraction of a micrometer (tiniest dust grains). In this thesis, a large set of simplifying assumptions were made, ignoring, in particular, any dependence of all these parameters on dust grain size, although such dependencies are expected. Although we think that the model presented in this work is a good starting point for the analysis of the EKB debris disk, several assumptions mentioned above can be improved.

**Parent Bodies.** As shown in this thesis the knowledge of the large parent bodies of several hundred of kilometer is not sufficient to unambiguously determine the dust distribution. Therefore, the knowledge of sub-kilometer objects, including good measurements of their orbital elements (in particular the eccentricity), would help to improve the extrapolation method and therefore the model, resulting in tighter constraints on the dust distribution and more accurate predictions for the upcoming dust flux measurements. Better constraints on the population of sub-kilometer objects, which could be expected, for instance, from the stellar occultation method (e.g., Liu et al., 2008; Schlichting et al., 2009; Bianco et al., 2010), would also be of great help.

**Grain Shape and Composition.** Not only the information of the existence of sub-kilometer objects is necessary, but the material composition is important as well. It is not only the fluffiness of objects but also the critical impact energy  $Q_D^*$ , which changes with the material and the outcomes of a collision will be different. Furthermore, the grain properties change when icy inclusions sublime. Further improvements on the *ACE* code may offer the possibility to model collisions between two different material compositions.

The assumption of spherical particles throughout all sizes is obviously unrealistic. Scanning electron microscope measurements show that dust grains of a few micrometer are not spherical at all (Brownlee et al., 2006; Wurm & Blum, 2000) so that Mie theory should not be applied. In more realistic models aligned non-spherical (spheroidal) dust grains are used (Wolf et al., 2002b). Schüppler et al. (in prep.) uses the assumption that (non-spherical) dust grains are built of a conglomerate of spherical particles and for these particles the T-matrix method can be used (see, e.g., Mackowski, 1994; Mackowski & Mishchenko, 1996). With this model it is possible to re-calculate the emission and absorption efficiencies of dust grains in a more realistic way.

**Impacts of Interstellar Grains.** Yamamoto & Mukai (1998a) calculated the production rate of dust in collisions between interstellar and EKB grains to be  $3 \times 10^5 \dots 3 \times 10^7 \text{ g s}^{-1}$ . Depending on the lower or upper limit of their estimate collisions with interstellar dust grains can contribute  $\approx 10\%$  or even  $\approx 1000\%$  to the dust production rate obtained in this thesis ( $2 \times 10^6 \text{ g s}^{-1}$ ). Therefore, future analyses should consider to implement interstellar dust grains into the simulations.

**Modification of the disk by planets.** An improvement of the planetary interaction with the EKB is necessary. Although resonant trapping and gravitational scattering are included in this work, the dynamics *in* mean-motion resonances are neglected. As seen in Chapter 3, some planetesimals are locked in resonances. There, the probability of a collision can increase up to a factor of two (or ten in 1:1 resonances, Queck et al. 2007) or even 100 (Wyatt, 2006). Furthermore, the produced grains will form clumps or spirals dependent on their size (e.g., Wyatt, 2003; Greaves et al., 2005; Wyatt, 2006; Krivov et al., 2007), which might be seen in the surface brightness image, dependent on the efficiency and therefore luminosity of the spiral rings.

**Measurements.** Of course, the most promising way to improve this model of the EKB dust is to use direct observations of dust. In particular, a size distribution of the impacted grains on the New Horizons dust counter would be very helpful to distinguish between the different extrapolation methods and perhaps then be able to at least exclude some of the possible extrapolations. New thermal emission constraints that could be expected from the Planck mission (Ade et al., 2012) are of course another way of improving dust measurements in the outer Solar System, albeit indirectly.

In any account, this study can be considered as a reasonable starting point to developing more accurate models of the debris disk of our own Solar System.

# Bibliography

- Acke, B., Min, M., Dominik, C., et al., 2012. *Herschel images of Fomalhaut. An extrasolar Kuiper belt at the height of its dynamical activity.* *Astron. Astrophys.*, 540, A125.
- Ade, P. A. R., Aghanim, N., Arnaud, M., et al., 2012. *Planck intermediate results. I. Further validation of new Planck clusters with XMM-Newton.* *Astron. Astrophys.*, 543, A102.
- Allen, C. W., 1973. *Astrophysical quantities.*
- Allen, R. L., Bernstein, G. M., & Malhotra, R., 2001. *The Edge of the Solar System.* *Astrophys. J. Letters*, 549, L241–L244.
- Arakawa, M., 1999. *Collisional Disruption of Ice by High-Velocity Impact.* *Icarus*, 142, 34–45.
- Backman, D., Marengo, M., Stapelfeldt, K., et al., 2009. *Epsilon Eridani's Planetary Debris Disk: Structure and Dynamics Based on Spitzer and Caltech Submillimeter Observatory Observations.* *Astrophys. J.*, 690, 1522–1538.
- Backman, D. E., Dasgupta, A., & Stencel, R. E., 1995. *Model of a Kuiper Belt Small Grain Population and Resulting Far-Infrared Emission.* *Astrophys. J. Letters*, 450, L35.
- Backman, D. E. & Paresce, F., 1993. *Main-sequence stars with circumstellar solid material - The VEGA phenomenon.* In E. H. Levy & J. I. Lunine, editors, *Protostars and Planets III*, 1253–1304.
- Balbus, S. A. & Hawley, J. F., 1992. *Is the Oort A-value a universal growth rate limit for accretion disk shear instabilities?* *Astrophys. J.*, 392, 662–666.
- Barucci, M. A., Brown, M. E., Emery, J. P., & Merlin, F., 2008. *Composition and Surface Properties of Transneptunian Objects and Centaurs.* In Barucci, M. A., Boehnhardt, H., Cruikshank, D. P., & Morbidelli, A., editor, *The Solar System Beyond Neptune*, 143–160.



- Beichman, C. A., Bryden, G., Stapelfeldt, K. R., et al., 2006. *New Debris Disks around Nearby Main-Sequence Stars: Impact on the Direct Detection of Planets*. *Astrophys. J.*, 652, 1674–1693.
- Beitz, E., Güttler, C., Blum, J., et al., 2011. *Low-velocity Collisions of Centimeter-sized Dust Aggregates*. *Astrophys. J.*, 736, 34.
- Benz, W. & Asphaug, E., 1999. *Catastrophic Disruptions Revisited*. *Icarus*, 142, 5–20.
- Bernstein, G. M., Trilling, D. E., Allen, R. L., et al., 2004. *The Size Distribution of Trans-Neptunian Bodies*. *Astron. J.*, 128, 1364–1390.
- Bianco, F. B., Zhang, Z.-W., Lehner, M. J., et al., 2010. *The TAOS Project: Upper Bounds on the Population of Small Kuiper Belt Objects and Tests of Models of Formation and Evolution of the Outer Solar System*. *Astron. J.*, 139, 1499–1514.
- Blum, J. & Wurm, G., 2008. *The Growth Mechanisms of Macroscopic Bodies in Protoplanetary Disks*. *Annual Review of Astronomy and Astrophysics*, 46, 21–56.
- Blum, J., Wurm, G., Kempf, S., et al., 2000. *Growth and Form of Planetary Seedlings: Results from a Microgravity Aggregation Experiment*. *Physical Review Letters*, 85, 2426–2429.
- Booth, M., Wyatt, M. C., Morbidelli, A., et al., 2009. *The history of the Solar system's debris disc: observable properties of the Kuiper belt*. *MNRAS*, 399, 385–398.
- Boss, A. P., 1997. *Giant planet formation by gravitational instability*. *Science*, 276, 1836–1839.
- Bottke, W. F., Nesvorný, D., Vokrouhlický, D., & Morbidelli, A., 2010. *The Irregular Satellites: The Most Collisionally Evolved Populations in the Solar System*. *Astron. J.*, 139, 994–1014.
- Bottke, W. F., Jr., Rubincam, D. P., & Burns, J. A., 2000. *Dynamical evolution of main belt meteoroids: Numerical simulations incorporating planetary perturbations and Yarkovsky thermal forces*. *Icarus*, 145, 301–331.
- Brown, M. E., 2001. *The Inclination Distribution of the Kuiper Belt*. *Astron. J.*, 121, 2804–2814.

- Brownlee, D., Tsou, P., Aléon, J., et al., 2006. *Comet 81P/Wild 2 Under a Microscope*. *Science*, 314, 1711–.
- Brucker, M. J., Grundy, W. M., Stansberry, J. A., et al., 2009. *High albedos of low inclination Classical Kuiper belt objects*. *Icarus*, 201, 284–294.
- Burns, J. A., Lamy, P. L., & Soter, S., 1979. *Radiation forces on small particles in the solar system*. *Icarus*, 40, 1–48.
- Chambers, J. E., 1999. *A hybrid symplectic integrator that permits close encounters between massive bodies*. *MNRAS*, 304, 793–799.
- Chen, C. H., Fitzgerald, M. P., & Smith, P. S., 2008. *A Possible Icy Kuiper Belt around HD 181327*. *Astrophys. J.*, 689, 539–544.
- Chen, C. H., Sargent, B. A., Bohac, C., et al., 2006. *Spitzer IRS Spectroscopy of IRAS-discovered Debris Disks*. *Astrophys. J. Suppl.*, 166, 351–377.
- Chiang, E. I. & Brown, M. E., 1999. *Keck Pencil-Beam Survey for Faint Kuiper Belt Objects*. *Astron. J.*, 118, 1411–1422.
- Crida, A., 2009. *Minimum Mass Solar Nebulae and Planetary Migration*. *Astrophys. J.*, 698, 606–614.
- Cuzzi, J. N., Hogan, R. C., & Shariff, K., 2008. *Toward Planetesimals: Dense Chondrule Clumps in the Protoplanetary Nebula*. *Astrophys. J.*, 687, 1432–1447.
- Cuzzi, J. N. & Weidenschilling, S. J., 2006. *Particle-Gas Dynamics and Primary Accretion*, 353–381.
- Delsanti, A. & Jewitt, D., 2006. *The Solar System Beyond The Planets*. Springer.
- Desch, S. J., 2007. *Mass Distribution and Planet Formation in the Solar Nebula*. *Astrophys. J.*, 671, 878–893.
- Dikarev, V., Preuß, O., Solanki, S., et al., 2009. *The Local Dust Foregrounds in the Microwave Sky. I. Thermal Emission Spectra*. *Astrophys. J.*, 705, 670–682.
- Dohnanyi, J. S., 1969. *Collisional Model of Asteroids and Their Debris*. *J. Geophys. Res.*, 74, 2531.

- Dominik, C., Blum, J., Cuzzi, J. N., & Wurm, G., 2007. *Growth of Dust as the Initial Step Toward Planet Formation*. *Protostars and Planets V*, 783–800.
- Dominik, C. & Decin, G., 2003. *Age Dependence of the Vega Phenomenon: Theory*. *Astrophys. J.*, 598, 626–635.
- Dominik, C. & Tielens, A. G. G. M., 1997. *The Physics of Dust Coagulation and the Structure of Dust Aggregates in Space*. *Astrophys. J.*, 480, 647.
- Donnison, J. R., 2006. *The size distribution of trans-Neptunian bodies*. *Planetary Space Science*, 54, 243–250.
- Doressoundiram, A., Peixinho, N., Doucet, C., et al., 2005. *The Meudon Multicolor Survey (2MS) of Centaurs and trans-neptunian objects: extended dataset and status on the correlations reported*. *Icarus*, 174, 90–104.
- Dullemond, C. P. & Dominik, C., 2005. *Dust coagulation in protoplanetary disks: A rapid depletion of small grains*. *Astron. Astrophys.*, 434, 971–986.
- Dumas, C., Merlin, F., Barucci, M. A., et al., 2007. *Surface composition of the largest dwarf planet 136199 Eris (2003 UB<sub>313</sub>)*. *Astron. Astrophys.*, 471, 331–334.
- Eiroa, C., Fedele, D., Maldonado, J., et al., 2010. *Cold DUST around NEarby Stars (DUNES). First results. A resolved exo-Kuiper belt around the solar-like star  $\zeta^2$  Ret.* *Astron. Astrophys.*, 518, L131.
- Eiroa, C., Marshall, J. P., Mora, A., et al., 2011. *Herschel discovery of a new class of cold, faint debris discs*. *ArXiv e-prints*.
- Elliot, J. L., Kern, S. D., Clancy, K. B., et al., 2005. *The Deep Ecliptic Survey: A Search for Kuiper Belt Objects and Centaurs. II. Dynamical Classification, the Kuiper Belt Plane, and the Core Population*. *Astron. J.*, 129, 1117–1162.
- Fraser, W. C., 2009. *The Collisional Divot in the Kuiper Belt Size Distribution*. *Astrophys. J.*, 706, 119–129.
- Fraser, W. C. & Kavelaars, J. J., 2009. *The Size Distribution of Kuiper Belt Objects for Dgsim 10 km*. *Astron. J.*, 137, 72–82.
- Fraser, W. C., Kavelaars, J. J., Holman, M. J., et al., 2008. *The Kuiper belt luminosity function from  $m=21$  to 26*. *Icarus*, 195, 827–843.

- Freistetter, F., Krivov, A. V., & Löhne, T., 2007. *Planets of  $\beta$  Pictoris revisited*. *Astron. Astrophys.*, 466, 389–393.
- Fuentes, C. I., George, M. R., & Holman, M. J., 2009. *A Subaru Pencil-Beam Search for  $m_R \sim 27$  Trans-Neptunian Bodies*. *Astrophys. J.*, 696, 91–95.
- Fuentes, C. I. & Holman, M. J., 2008. *a SUBARU Archival Search for Faint Trans-Neptunian Objects*. *Astron. J.*, 136, 83–97.
- Fujiwara, A., 1986. *Results obtained by laboratory simulations of catastrophic impact*. *Mem. Societa Astronomica Italiana*, 57, 47–64.
- Fujiwara, A., Kamimoto, G., & Tsukamoto, A., 1977. *Destruction of basaltic bodies by high-velocity impact*. *Icarus*, 31, 277–288.
- Gladman, B., Kavelaars, J. J., Nicholson, P. D., et al., 1998. *Pencil-Beam Surveys for Faint Trans-Neptunian Objects*. *Astron. J.*, 116, 2042–2054.
- Gladman, B., Kavelaars, J. J., Petit, J.-M., et al., 2001. *The Structure of the Kuiper Belt: Size Distribution and Radial Extent*. *Astron. J.*, 122, 1051–1066.
- Goldreich, P., Lithwick, Y., & Sari, R., 2004. *Planet Formation by Coagulation: A Focus on Uranus and Neptune*. *Annual Review of Astronomy and Astrophysics*, 42, 549–601.
- Goldreich, P. & Ward, W. R., 1973. *The Formation of Planetesimals*. *Astrophys. J.*, 183, 1051–1062.
- Gomes, R., Levison, H. F., Tsiganis, K., & Morbidelli, A., 2005. *Origin of the cataclysmic Late Heavy Bombardment period of the terrestrial planets*. *Nature*, 435, 466–469.
- Greaves, J. S., Holland, W. S., Wyatt, M. C., et al., 2005. *Structure in the  $\epsilon$  Eridani Debris Disk*. *Astrophys. J. Letters*, 619, L187–L190.
- Greaves, J. S. & Wyatt, M. C., 2010. *Debris discs and comet populations around Sun-like stars: the Solar system in context*. *MNRAS*, 404, 1944–1951.
- Greaves, J. S., Wyatt, M. C., Holland, W. S., & Dent, W. R. F., 2004. *The debris disc around  $\tau$  Ceti: a massive analogue to the Kuiper Belt*. *MNRAS*, 351, L54–L58.
- Greenberg, R., Hartmann, W. K., Chapman, C. R., & Wacker, J. F., 1978. *Planetesimals to planets - Numerical simulation of collisional evolution*. *Icarus*, 35, 1–26.

- Greenzweig, Y. & Lissauer, J. J., 1992. *Accretion rates of protoplanets. II - Gaussian distributions of planetesimal velocities*. *Icarus*, 100, 440–463.
- Grün, E., Gustafson, B. A. S., Dermott, S., & Fechtig, H., editors, 2001. *Interplanetary Dust*. Springer.
- Gulbis, A. A. S., Elliot, J. L., Adams, E. R., et al., 2010. *Unbiased Inclination Distributions for Objects in the Kuiper Belt*. *Astron. J.*, 140, 350–369.
- Gurnett, D. A., Ansher, J. A., Kurth, W. S., & Granroth, L. J., 1997. *Micron-sized dust particles detected in the outer solar system by the Voyager 1 and 2 plasma wave instruments*. *Geophys. Res. Lett.*, 24, 3125–3128.
- Gustafson, B. A. S., 1994. *Physics of Zodiacal Dust*. *Annual Review of Earth and Planetary Sciences*, 22, 553–595.
- Hainaut, O. R., Kleyna, J., Sarid, G., et al., 2012. *P/2010 A2 LINEAR. I. An impact in the asteroid main belt*. *Astron. Astrophys.*, 537, A69.
- Haisch, K. E., Jr., Lada, E. A., & Lada, C. J., 2001. *Disk Frequencies and Lifetimes in Young Clusters*. *Astrophys. J. Letters*, 553, L153–L156.
- Han, D., Poppe, A. R., Piquette, M., et al., 2011. *Constraints on dust production in the Edgeworth-Kuiper Belt from Pioneer 10 and New Horizons measurements*. *Geophys. Res. Lett.*, 38, L24102.
- Hauschildt, P. H., Allard, F., & Baron, E., 1999. *The NextGen Model Atmosphere Grid for  $3000 \leq T_{\text{eff}} \leq 10,000$  K*. *Astrophys. J.*, 512, 377–385.
- Hayashi, C., 1981. *Formation of the planets*. In D. Sugimoto, D. Q. Lamb, & D. N. Schramm, editors, *Fundamental Problems in the Theory of Stellar Evolution*, volume 93 of *IAU Symposium*, 113–126.
- Heinrichsen, I., Walker, H. J., & Klaas, U., 1998. *Infrared mapping of the dust disc around VEGA*. *MNRAS*, 293, L78–L82.
- Henning, T., Il'In, V. B., Krivova, N. A., et al., 1999. *WWW database of optical constants for astronomy*. *Astronomy and Astrophysics, Supplement*, 136, 405–406.
- Hernández, J., Calvet, N., Hartmann, L., et al., 2009. *Spitzer Observations of the  $\lambda$  Orionis Cluster. I. The Frequency of Young Debris Disks at 5 Myr*. *Astrophys. J.*, 707, 705–715.

- Hildebrand, R. H., 1983. *The Determination of Cloud Masses and Dust Characteristics from Submillimetre Thermal Emission*. Quarterly Journal of the Royal Astronomical Society, 24, 267.
- Horányi, M., Hoxie, V., James, D., et al., 2008. *The Student Dust Counter on the New Horizons Mission*. Space Science Reviews, 140, 387–402.
- Ichikawa, K. & Fukugita, M., 2011. *Microwave Emission from the Edgeworth-Kuiper Belt and the Asteroid Belt Constrained from the Wilkinson Microwave Anisotropy Probe*. Astrophys. J., 736, 122.
- Ida, S. & Makino, J., 1993. *Scattering of planetesimals by a protoplanet - Slowing down of runaway growth*. Icarus, 106, 210.
- Irwin, M., Tremaine, S., & Zytlow, A. N., 1995. *A Search for Slow-Moving Objects and the Luminosity Function of the Kuiper Belt*. Astron. J., 110, 3082–3092.
- Jewitt, D., Luu, J., & Chen, J., 1996. *The Mauna Kea-Cerro-Tololo (MKCT) Kuiper Belt and Centaur Survey*. Astron. J., 112, 1225–1332.
- Jewitt, D., Luu, J., & Marsden, B. G., 1992. *1992 QB1*. IAU Circulars, 5611, 1.
- Jewitt, D., Luu, J., & Trujillo, C., 1998. *Large Kuiper Belt Objects: The Mauna Kea 8K CCD Survey*. Astron. J., 115, 2125–2135.
- Jewitt, D., Moro-Martín, A., & Lacerda, P., 2009. *The Kuiper Belt and Other Debris Disks*, 53–103.
- Jewitt, D., Peixinho, N., & Hsieh, H. H., 2007. *U-Band Photometry of Kuiper Belt Objects*. Astron. J., 134, 2046–2053.
- Jewitt, D., Stuart, J. S., & Li, J., 2011. *Pre-discovery Observations of Disrupting Asteroid P/2010 A2*. Astron. J., 142, 28.
- Jewitt, D. C. & Luu, J. X., 1995. *The solar system beyond Neptune*. Astron. J., 109, 1867–1876.
- Johansen, A., Klahr, H., & Henning, T., 2006. *Gravoturbulent Formation of Planetesimals*. Astrophys. J., 636, 1121–1134.
- Johansen, A., Oishi, J. S., Low, M.-M. M., et al., 2007. *Rapid planetesimal formation in turbulent circumstellar disks*. Nature, 448, 1022–1025.

- Kavelaars, J. J., Jones, R. L., Gladman, B. J., et al., 2009. *The Canada-France Ecliptic Plane Survey—L3 Data Release: The Orbital Structure of the Kuiper Belt*. *Astron. J.*, 137, 4917–4935.
- Kenyon, S. J. & Bromley, B. C., 2008. *Variations on Debris Disks: Icy Planet Formation at 30–150 AU for 1–3  $M_{\text{solar}}$  Main-Sequence Stars*. *Astrophys. J. Suppl.*, 179, 451–483.
- Kobayashi, H., Kimura, H., Watanabe, S.-I., et al., 2011. *Sublimation Temperature of Circumstellar Dust Particles and Its Importance for Dust Ring Formation*. ArXiv e-prints.
- Kobayashi, H., Kimura, H., Yamamoto, S., et al., 2010. *Ice sublimation of dust particles and their detection in the outer solar system*. *Earth, Planets, and Space*, 62, 57–61.
- Kobayashi, H., Watanabe, S.-I., Kimura, H., & Yamamoto, T., 2008. *Dust ring formation due to ice sublimation of radially drifting dust particles under the Poynting Robertson effect in debris disks*. *Icarus*, 195, 871–881.
- , 2009. *Dust ring formation due to sublimation of dust grains drifting radially inward by the Poynting-Robertson drag: An analytical model*. *Icarus*, 201, 395–405.
- Krivov, A. V., 2010. *Debris disks: seeing dust, thinking of planetesimals and planets*. *Research in Astronomy and Astrophysics*, 10, 383–414.
- Krivov, A. V., Löhne, T., & Sremčević, M., 2006. *Dust distributions in debris disks: effects of gravity, radiation pressure and collisions*. *Astron. Astrophys.*, 455, 509–519.
- Krivov, A. V., Mann, I., & Krivova, N. A., 2000. *Size distributions of dust in circumstellar debris discs*. *Astron. Astrophys.*, 362, 1127–1137.
- Krivov, A. V., Müller, S., Löhne, T., & Mutschke, H., 2008. *Collisional and Thermal Emission Models of Debris Disks: Toward Planetesimal Population Properties*. *Astrophys. J.*, 687, 608–622.
- Krivov, A. V., Queck, M., Löhne, T., & Sremčević, M., 2007. *On the nature of clumps in debris disks*. *Astron. Astrophys.*, 462, 199–210.
- Krivov, A. V., Sremčević, M., & Spahn, F., 2005. *Evolution of a keplerian disk of colliding and fragmenting particles: A kinetic model and application to the Edgeworth-Kuiper Belt*. *Icarus*, 174, 105–134.

- Kuchner, M. J., 2004. *A Minimum-Mass Extrasolar Nebula*. *Astrophys. J.*, 612, 1147–1151.
- Kuchner, M. J., Brown, M. E., & Holman, M., 2002. *Long-Term Dynamics and the Orbital Inclinations of the Classical Kuiper Belt Objects*. *Astron. J.*, 124, 1221–1230.
- Kuchner, M. J. & Holman, M. J., 2003. *The Geometry of Resonant Signatures in Debris Disks with Planets*. *Astrophys. J.*, 588, 1110–1120.
- Kuchner, M. J. & Stark, C. C., 2010. *Collisional Grooming Models of the Kuiper Belt Dust Cloud*. *Astron. J.*, 140, 1007–1019.
- Lamy, P. L., Toth, I., Fernandez, Y. R., & Weaver, H. A., 2004. *The sizes, shapes, albedos, and colors of cometary nuclei*, 223–264.
- Landgraf, M., Liou, J.-C., Zook, H. A., & Grün, E., 2002. *Origins of Solar System Dust beyond Jupiter*. *Astron. J.*, 123, 2857–2861.
- Laor, A. & Draine, B. T., 1993. *Spectroscopic constraints on the properties of dust in active galactic nuclei*. *Astrophys. J.*, 402, 441–468.
- Larsen, J. A., Roe, E. S., Albert, C. E., et al., 2007. *The Search for Distant Objects in the Solar System Using Spacewatch*. *Astron. J.*, 133, 1247–1270.
- Lawler, S. M., Beichman, C. A., Bryden, G., et al., 2009. *Explorations Beyond the Snow Line: Spitzer/IRS Spectra of Debris Disks Around Solar-type Stars*. *Astrophys. J.*, 705, 89–111.
- Levison, H. F., Morbidelli, A., Vanlaerhoven, C., et al., 2008. *Origin of the structure of the Kuiper belt during a dynamical instability in the orbits of Uranus and Neptune*. *Icarus*, 196, 258–273.
- Liou, J.-C. & Zook, H. A., 1999. *Signatures of the Giant Planets Imprinted on the Edgeworth-Kuiper Belt Dust Disk*. *Astron. J.*, 118, 580–590.
- Lissauer, J. J., 1987. *Timescales for planetary accretion and the structure of the protoplanetary disk*. *Icarus*, 69, 249–265.
- Liu, C.-Y., Chang, H.-K., Liang, J.-S., & King, S.-K., 2008. *Millisecond dip events in the 2007 RXTE/PCA data of Sco X-1 and the trans-Neptunian object size distribution*. *MNRAS*, 388, L44–L48.



- Löhne, T., 2008. *Models of Rotationally Symmetric, Collision-Dominated Debris Discs*. Ph.D. thesis, Models of Rotationally Symmetric Friedrich Schiller Universität Jena, Jena, Germany.
- Löhne, T., Augereau, J.-C., Ertel, S., et al., 2012. *Modelling the huge, Herschel-resolved debris ring around HD 207129*. *Astron. Astrophys.*, 537, A110.
- Löhne, T., Krivov, A. V., & Rodmann, J., 2008. *Long-Term Collisional Evolution of Debris Disks*. *Astrophys. J.*, 673, 1123–1137.
- Lowry, S. C., Fitzsimmons, A., Pravec, P., et al., 2007. *Direct Detection of the Asteroidal YORP Effect*. *Science*, 316, 272–.
- Luu, J. X. & Jewitt, D. C., 1998. *Deep Imaging of the Kuiper Belt with the Keck 10 Meter Telescope*. *Astrophys. J. Letters*, 502, L91–L94.
- , 2002. *Kuiper Belt Objects: Relics from the Accretion Disk of the Sun*. *Annual Review of Astronomy and Astrophysics*, 40, 63–101.
- Mackowski, D. W., 1994. *Calculation of total cross sections of multiple-sphere clusters*. *Journal of the Optical Society of America A*, 11, 2851–2861.
- Mackowski, D. W. & Mishchenko, M. I., 1996. *Calculation of the T matrix and the scattering matrix for ensembles of spheres*. *Journal of the Optical Society of America A*, 13, 2266–2278.
- Mizuno, H., 1980. *Formation of the Giant Planets*. *Progress of Theoretical Physics*, 64, 544–557.
- Mommert, M., Harris, A. W., Kiss, C., et al., 2012. *TNOs are Cool: A survey of the trans-Neptunian region V. Physical characterization of 18 Plutinos using Herschel PACS observations*. ArXiv e-prints.
- Moór, A., Ábrahám, P., Derekas, A., et al., 2006. *Nearby Debris Disk Systems with High Fractional Luminosity Reconsidered*. *Astrophys. J.*, 644, 525–542.
- Morbidelli, A., 2010. *A coherent and comprehensive model of the evolution of the outer Solar System*. *Comptes Rendus Physique*, 11, 651–659.
- Morbidelli, A., Bottke, W. F., Nesvorný, D., & Levison, H. F., 2009. *Asteroids were born big*. *Icarus*, 204, 558–573.

- Morbidelli, A., Levison, H. F., Tsiganis, K., & Gomes, R., 2005. *Chaotic capture of Jupiter's Trojan asteroids in the early Solar System*. *Nature*, 435, 462–465.
- Moro-Martín, A. & Malhotra, R., 2002. *A study of the dynamics of dust from the Kuiper belt: spatial distribution and spectral energy distribution*. *Astron. J.*, 124, 2305–2321.
- , 2003. *Dynamical Models of Kuiper Belt Dust in the Inner and Outer Solar System*. *Astron. J.*, 125, 2255–2265.
- , 2005. *Dust Outflows and Inner Gaps Generated by Massive Planets in Debris Disks*. *Astrophys. J.*, 633, 1150–1167.
- Müller, S., 2007. *Berechnung photometrischer Eigenschaften von zirkumstellaren Trümmerscheiben*. Diplomarbeit, Friedrich-Schiller Universität Jena, Germany.
- Müller, S., Löhne, T., & Krivov, A. V., 2010. *The Debris Disk of Vega: A Steady-State Collisional Cascade, Naturally*. *Astrophys. J.*, 708, 1728–1747.
- Murray, C. D. & Dermott, S. F., 2000. *Solar System Dynamics*. *Solar System Dynamics*, by C.D. Murray and S.F. Dermott. ISBN 0521575974. Cambridge, UK: Cambridge University Press, 2000.
- Mustill, A. J. & Wyatt, M. C., 2011. *A general model of resonance capture in planetary systems: first- and second-order resonances*. *MNRAS*, 413, 554–572.
- Nakamura, T., Noguchi, T., Tanaka, M., et al., 2011. *Itokawa Dust Particles: A Direct Link Between S-Type Asteroids and Ordinary Chondrites*. *Science*, 333, 1113–.
- Nesvorný, D., Vokrouhlický, D., & Morbidelli, A., 2007. *Capture of Irregular Satellites during Planetary Encounters*. *Astron. J.*, 133, 1962–1976.
- Newton, I., 1687. *Philosophiæ naturalis principia mathematica*.
- Noll, K. S., Stephens, D. C., Grundy, W. M., et al., 2004. *The Orbit and Albedo of Trans-Neptunian Binary (58534) 1997 CQ<sub>29</sub>*. *Astron. J.*, 128, 2547–2552.
- O'Brien, D. P. & Greenberg, R., 2003. *Steady-state size distributions for collisional populations: analytical solution with size-dependent strength*. *Icarus*, 164, 334–345.
- Ozernoy, L. M., Gorkavyi, N. N., Mather, J. C., & Taidakova, T. A., 2000. *Signatures of Exosolar Planets in Dust Debris Disks*. *Astrophys. J. Letters*, 537, L147–L151.

- Pál, A., Kiss, C., Müller, T. G., et al., 2012. "TNOs are Cool": A survey of the trans-Neptunian region. VII. Size and surface characteristics of (90377) Sedna and 2010 EK<sub>139</sub>. *Astron. Astrophys.*, 541, L6.
- Peixinho, N., Lacerda, P., & Jewitt, D., 2008. *Color-Inclination Relation of the Classical Kuiper Belt Objects*. *Astron. J.*, 136, 1837–1845.
- Petit, J.-M., Holman, M. J., Gladman, B. J., et al., 2006. *The Kuiper Belt luminosity function from  $m_R = 22$  to 25*. *MNRAS*, 365, 429–438.
- Pilbratt, G. L., Riedinger, J. R., Passvogel, T., et al., 2010. *Herschel Space Observatory. An ESA facility for far-infrared and submillimetre astronomy*. *Astron. Astrophys.*, 518, L1.
- Pinilla-Alonso, N., Brunetto, R., Licandro, J., et al., 2009. *The surface of (136108) Haumea (2003 EL<sub>61</sub>), the largest carbon-depleted object in the trans-Neptunian belt*. *Astron. Astrophys.*, 496, 547–556.
- Poglitsch, A., Waelkens, C., Geis, N., et al., 2010. *The Photodetector Array Camera and Spectrometer (PACS) on the Herschel Space Observatory*. *Astron. Astrophys.*, 518, L2.
- Poppe, A., James, D., Jacobsmeyer, B., & Horányi, M., 2010. *First results from the Venetia Burney Student Dust Counter on the New Horizons mission*. *Geophys. Res. Lett.*, 37, 11101.
- Queck, M., Krivov, A. V., Sremčević, M., & Thébault, P., 2007. *Collisional velocities and rates in resonant planetesimal belts*. *Celestial Mechanics and Dynamical Astronomy*, 99, 169–196.
- Quinn, T., Tremaine, S., & Duncan, M., 1990. *Planetary perturbations and the origins of short-period comets*. *Astrophys. J.*, 355, 667–679.
- Raymond, S. N., Quinn, T., & Lunine, J. I., 2006. *High-resolution simulations of the final assembly of Earth-like planets I. Terrestrial accretion and dynamics*. *Icarus*, 183, 265–282.
- Reidemeister, M., 2007. *Resonante Dynamik von Staubteilchen in Trümmerscheiben mit Planeten*. Diplomarbeit, Friedrich-Schiller Universität Jena, Germany.
- Reidemeister, M., Krivov, A. V., Schmidt, T. O. B., et al., 2009. *A possible architecture of the planetary system HR 8799*. *Astron. Astrophys.*, 503, 247–258.

- Reidemeister, M., Krivov, A. V., Stark, C. C., et al., 2011. *The cold origin of the warm dust around  $\epsilon$  Eridani*. *Astron. Astrophys.*, 527, A57+.
- Rice, W. K. M., Lodato, G., Pringle, J. E., et al., 2004. *Accelerated planetesimal growth in self-gravitating protoplanetary discs*. *MNRAS*, 355, 543–552.
- Safronov, V. S., 1969. *Evolution of the Protoplanetary Cloud and Formation of the Earth and Planets*. Nauka, Moscow (in Russian). [English translation: NASA TTF-677, 1972.].
- Santos-Sanz, P., Lellouch, E., Fornasier, S., et al., 2012. *"TNOs are Cool": A Survey of the Transneptunian Region IV. Size/albedo characterization of 15 scattered disk and detached objects observed with Herschel Space Observatory-PACS*. ArXiv e-prints.
- Schlichting, H. E., Ofek, E. O., Wenz, M., et al., 2009. *A single sub-kilometre Kuiper belt object from a stellar occultation in archival data*. *Nature*, 462, 895–897.
- Sheret, I., Dent, W. R. F., & Wyatt, M. C., 2004. *Submillimetre observations and modelling of Vega-type stars*. *MNRAS*, 348, 1282–1294.
- Snodgrass, C., Tubiana, C., Vincent, J.-B., et al., 2010. *A collision in 2009 as the origin of the debris trail of asteroid P/2010A2*. *Nature*, 467, 814–816.
- Stansberry, J., Grundy, W., Brown, M., et al., 2008. *Physical Properties of Kuiper Belt and Centaur Objects: Constraints from the Spitzer Space Telescope*. The Solar System Beyond Neptune.
- Stark, C. C. & Kuchner, M. J., 2009. *A New Algorithm for Self-consistent Three-dimensional Modeling of Collisions in Dusty Debris Disks*. *Astrophys. J.*, 707, 543–553.
- Stern, S. A., 1995. *Collisional time scales in the Kuiper Disk and their implications*. *Astron. J.*, 110, 856–868.
- , 1996. *Signatures of collisions in the Kuiper Disk*. *Astron. Astrophys.*, 310, 999–1010.
- Stewart, S. T. & Leinhardt, Z. M., 2009. *Velocity-Dependent Catastrophic Disruption Criteria for Planetesimals*. *Astrophys. J. Letters*, 691, L133–L137.
- Strubbe, L. E. & Chiang, E. I., 2006. *Dust Dynamics, Surface Brightness Profiles, and Thermal Spectra of Debris Disks: The Case of AU Microscopii*. *Astrophys. J.*, 648, 652–665.

- Su, K. Y. L., Rieke, G. H., Misselt, K. A., et al., 2005. *The Vega Debris Disk: A Surprise from Spitzer*. *Astrophys. J.*, 628, 487–500.
- Tanner, A., Beichman, C., Bryden, G., et al., 2009. *Survey of Nearby FGK Stars at 160  $\mu\text{m}$  with Spitzer*. *Astrophys. J.*, 704, 109–116.
- Teplitz, V. L., Stern, S. A., Anderson, J. D., et al., 1999. *Infrared Kuiper Belt Constraints*. *Astrophys. J.*, 516, 425–435.
- Th ebault, P., 2009. *Vertical structure of debris discs*. *Astron. Astrophys.*, 505, 1269–1276.
- Th ebault, P. & Augereau, J., 2007. *Collisional processes and size distribution in spatially extended debris discs*. *Astron. Astrophys.*, 472, 169–185.
- Th ebault, P., Augereau, J. C., & Beust, H., 2003. *Dust production from collisions in extrasolar planetary systems. The inner beta Pictoris disc*. *Astron. Astrophys.*, 408, 775–788.
- Th ebault, P. & Brahic, A., 1998. *Dynamical influence of a proto-Jupiter on a disc of colliding planetesimals*. *Planetary Space Science*, 47, 233–243.
- Th ebault, P. & Doressoundiram, A., 2003. *Colors and collision rates within the Kuiper belt: problems with the collisional resurfacing scenario*. *Icarus*, 162, 27–37.
- Th ebault, P., Marzari, F., & Scholl, H., 2002. *Terrestrial planet formation in exoplanetary systems with a giant planet on an external orbit*. *Astron. Astrophys.*, 384, 594–602.
- Toomre, A., 1964. *On the gravitational stability of a disk of stars*. *Astrophys. J.*, 139, 1217–1238.
- Trujillo, C. A. & Brown, M. E., 2002. *A Correlation between Inclination and Color in the Classical Kuiper Belt*. *Astrophys. J. Letters*, 566, L125–L128.
- , 2003. *The Caltech Wide Area Sky Survey*. *Earth Moon and Planets*, 92, 99–112.
- Trujillo, C. A., Jewitt, D. C., & Luu, J. X., 2000. *Population of the Scattered Kuiper Belt*. *Astrophys. J. Letters*, 529, L103–L106.
- , 2001a. *Properties of the Trans-Neptunian Belt: Statistics from the Canada-France-Hawaii Telescope Survey*. *Astron. J.*, 122, 457–473.

- Trujillo, C. A., Luu, J. X., Bosh, A. S., & Elliot, J. L., 2001b. *Large Bodies in the Kuiper Belt*. *Astron. J.*, 122, 2740–2748.
- Vandenbussche, B., Sibthorpe, B., Acke, B., et al., 2010. *The  $\beta$  Pictoris disk imaged by Herschel PACS and SPIRE*. *Astron. Astrophys.*, 518, L133.
- Vilenius, E., Kiss, C., Mommert, M., et al., 2012. *"TNOs are Cool": A survey of the trans-Neptunian region VI. Herschel/PACS observations and thermal modeling of 19 classical Kuiper belt objects*. ArXiv e-prints.
- Vitense, Ch., Krivov, A. V., Kobayashi, H., & Löhne, T., 2012. *An improved model of the Edgeworth-Kuiper debris disk*. *Astron. Astrophys.*, 540, A30.
- Vitense, Ch., Krivov, A. V., & Löhne, T., 2010. *The Edgeworth-Kuiper debris disk*. *Astron. Astrophys.*, 520, A32.
- Wada, K., Tanaka, H., Suyama, T., et al., 2007. *Numerical Simulation of Dust Aggregate Collisions. I. Compression and Disruption of Two-Dimensional Aggregates*. *Astrophys. J.*, 661, 320–333.
- , 2008. *Numerical Simulation of Dust Aggregate Collisions. II. Compression and Disruption of Three-Dimensional Aggregates in Head-on Collisions*. *Astrophys. J.*, 677, 1296–1308.
- , 2009. *Collisional Growth Conditions for Dust Aggregates*. *Astrophys. J.*, 702, 1490–1501.
- Warren, S. G., 1984. *Optical constants of ice from the ultraviolet to the microwave*. *App. Optics*, 23, 1206–1225.
- Weidenschilling, S. J., 1977. *The distribution of mass in the planetary system and solar nebula*. *Astrophys. Space Sci.*, 51, 153–158.
- , 1980. *Dust to planetesimals - Settling and coagulation in the solar nebula*. *Icarus*, 44, 172–189.
- Wetherill, G. W., 1980. *Formation of the terrestrial planets*. *Ann. Rev. Astron. Astrophys.*, 18, 77–113.
- Wetherill, G. W. & Stewart, G. R., 1989. *Accumulation of a swarm of small planetesimals*. *Icarus*, 77, 330–357.

- Wolf, S., 2008. *Signatures of planets in young and evolved circumstellar disks*. *Physica Scripta Volume T*, 130(1), 014025.
- Wolf, S., Gueth, F., Henning, T., & Kley, W., 2002a. *Detecting Planets in Protoplanetary Disks: A Prospective Study*. *Astrophys. J. Letters*, 566, L97–L99.
- Wolf, S. & Hillenbrand, L. A., 2003. *Model Spectral Energy Distributions of Circumstellar Debris Disks. I. Analytic Disk Density Distributions*. *Astrophys. J.*, 596, 603–620.
- Wolf, S., Moro-Martín, A., & D’Angelo, G., 2007. *Signatures of planets in protoplanetary and debris disks*. *Planetary Space Science*, 55, 569–581.
- Wolf, S. & Voshchinnikov, N. V., 2004. *Mie scattering by ensembles of particles with very large size parameters*. *Computer Physics Communications*, 162, 113–123.
- Wolf, S., Voshchinnikov, N. V., & Henning, T., 2002b. *Multiple scattering of polarized radiation by non-spherical grains: First results*. *Astron. Astrophys.*, 385, 365–376.
- Wurm, G. & Blum, J., 1998. *Experiments on Preplanetary Dust Aggregation*. *Icarus*, 132, 125–136.
- , 2000. *An Experimental Study on the Structure of Cosmic Dust Aggregates and Their Alignment by Motion Relative to Gas*. *Astrophys. J. Letters*, 529, L57–L60.
- Wurm, G., Paraskov, G., & Krauss, O., 2005. *Growth of planetesimals by impacts at ~25 m/s*. *Icarus*, 178, 253–263.
- Wyatt, M. C., 2003. *Resonant Trapping of Planetesimals by Planet Migration: Debris Disk Clumps and Vega’s Similarity to the Solar System*. *Astrophys. J.*, 598, 1321–1340.
- Wyatt, M. C., 2005. *The insignificance of P-R drag in detectable extrasolar planetesimal belts*. *Astron. Astrophys.*, 433, 1007–1012.
- , 2006. *Dust in resonant extrasolar Kuiper belts: Grain size and wavelength dependence of disk structure*. *Astrophys. J.*, 639, 1153–1165.
- Wyatt, M. C., 2008. *Evolution of Debris Disks*. *Annual Review of Astronomy and Astrophysics*, 46, 339–383.
- Wyatt, M. C., Clarke, C. J., & Booth, M., 2011. *Debris disk size distributions: steady state collisional evolution with Poynting-Robertson drag and other loss processes*. *Celestial Mechanics and Dynamical Astronomy*, 111, 1–28.


- Wyatt, M. C. & Dent, W. R. F., 2002. *Collisional processes in extrasolar planetesimal discs - dust clumps in Fomalhaut's debris disc*. MNRAS, 334, 589–607.
- Wyatt, M. C., Smith, R., Su, K. Y. L., et al., 2007. *Steady State Evolution of Debris Disks around A Stars*. Astrophys. J., 663, 365–382.
- Wyatt, S. P. & Whipple, F. L., 1950. *The Poynting-Robertson effect on meteor orbits*. Astrophys. J., 111, 134–141.
- Yamamoto, S. & Mukai, T., 1998a. *Dust production by impacts of interstellar dust on Edgeworth-Kuiper Belt objects*. Astron. Astrophys., 329, 785–791.
- , 1998b. *Thermal radiation from dust grains in Edgeworth-Kuiper belt*. Earth, Planets and Space, 50, 531–537.



# Danksagung

Auf der Dankesliste ganz oben steht selbstverständlich Prof. Dr. Alexander Krivov, der mich nach meiner Diplomarbeit als Doktorand in seiner Gruppe aufnahm und mich in den letzten Jahren betreute. Mit seiner Hilfe war es mir möglich, mich in der wissenschaftlichen Welt zurechtzufinden, zu beweisen und viele interessante Menschen kennenzulernen. Dazu gehören auch zahlreiche Reisen zu Konferenzen, Tagungen und Workshops in aller Welt.

Nicht minder weit oben auf der Dankesliste steht Dr. Torsten Löhne, welcher auch keine Mühen scheute, sich meinen Fragen zu stellen und immer zu Diskussionen bereit war, auch wenn sie mal länger dauerten.

Für stundenlange Diskussionen in Telefonkonferenzen bedanke ich mich auch bei Katharina Hohn. Meinen Eltern Edeltraut und Peter Vitense gebührt ebenso Dank. Auch meinen geschätzten Kollegen Dr. Harald Mutschke, Dr. Hiroshi Kobayashi, Jürgen Weiprecht, PD Dr. Katharina Schreyer, Martin Reidemeister, Dr. Sebastian Müller und Simon Zeidler möchte ich danken. Und ich möchte die schönen Stunden im Fitnessstudio mit Ludwig Trepl und im Stadion mit Sven Elsmann nicht missen, genauso wie die Stunden mit Caroline Reinert und Christian Beck. Danke auch an meine Vortragsente  sowie alle anderen Mitgliedern und Mitarbeitern des AIU.

Special thanks to Dr. Jonty Marshall for reading the manuscript and helping to improve the language.

Der Deutschen Forschungsgesellschaft (DFG) gebührt ebenso mein Dank, genau wie den Antragstellern :)

# Ehrenwörtliche Erklärung

Ich erkläre hiermit ehrenwörtlich, dass ich die vorliegende Arbeit selbstständig, ohne die unzulässige Hilfe Dritter und ohne die Benutzung anderer als der angegebenen Hilfsmittel und Literatur angefertigt habe. Die aus anderen Quellen direkt oder indirekt übernommenen Daten und Konzepte sind unter Angabe der Quelle gekennzeichnet. Personen, die an der inhaltlich-materiellen Erstellung der vorliegenden Arbeit beteiligt waren, sind am Anfang des jeweiligen Kapitels erwähnt. Weitere Personen waren nicht beteiligt. Insbesondere habe ich hierfür nicht die entgeltliche Hilfe von Vermittlungs- und bzw. Beratungsdiensten (Promotionsberater oder andere Personen) in Anspruch genommen. Niemand hat von mir unmittelbar oder mittelbar geldwerte Leistungen für Arbeiten erhalten, die im Zusammenhang mit dem Inhalt der vorgelegten Dissertation stehen.

Die Arbeit wurde bisher weder im In- noch im Ausland in gleicher oder ähnlicher Form einer anderen Prüfungsbehörde vorgelegt.

Die geltende Promotionsordnung der Physikalisch-Astronomischen Fakultät ist mir bekannt. Ich versichere ehrenwörtlich, dass ich nach bestem Wissen die reine Wahrheit gesagt und nichts verschwiegen habe.

Jena, den 09. Juli 2012

Christian Vitense